

GEO511 - Master's thesis

Investigations of the internal structures  
and geomorphological characteristics of an  
ice-debris complex in the Ak-Shiirak,  
Central Tien Shan, Kyrgyzstan

**June 30, 2015**

Submitted by

**Nico Rohrbach**

rohrbach.nico@bluewin.ch

Matr-Nr: 08-123-515

Supervised by

**Dr. habil. Tobias Bolch**

Faculty representative

**Prof. Dr. Andreas Vieli**



**University of  
Zurich**<sup>UZH</sup>

Glaciology and Geomorphodynamics Group - 3G

Department of Geography, University of Zurich

Winterthurerstrasse 190

CH-8057 Zürich



## Abstract

Mountains are fundamental water towers for adjacent, densely populated lowlands. Runoff will be affected by glacier retreat or earlier snow melt, caused by global warming. Periglacial landforms, such as ice-rich permafrost or rock glaciers are believed to compensate the loss in water availability with increasing temperatures. In the arid mountains of Central Asia, enormous periglacial ice-debris complexes are predominant and believed to contain a significant amount of internal ice. In order to better understand such a landform, an ice-debris complex in the Ak-Shiirak massif, in the Central Tien Shan of Kyrgyzstan, was investigated.

The main aim of this thesis was to understand the structure and genesis of the landform as well as to estimate the ice content and its hydrological significance. The internal structures were investigated using Ground Penetrating Radar (GPR). Furthermore a geomorphological map and a rock glacier inventory were developed using satellite imageries.

A total of 27 GPR profiles were taken on a glacier and its adjacent ice-debris complex. Clear reflections were apparent, indicating internal structures. The ice-debris complex was classified into five landform classes: glacier, medial moraine, lateral moraine, rock glacier tongue and glacio-fluvial plain. The landform classes showed distinguishable reflection patterns.

The geomorphological map showed that glacial, periglacial and the gravitational process domains were most dominant in the study area. The geomorphological characteristics were in accordance with the internal structures and the GPR reflection patterns. Based on the GPR profiles and the geomorphological map, the ice-debris complex was interpreted to be an assembled, intermediate landform shaped by the interaction of glacial and periglacial process domains.

The ice content of the ice-debris complex could not be estimated using on-site GPR measurements, but was assessed with existing literature. In a rock glacier inventory, a total of 63 rock glaciers were mapped and their ice contents were estimated using a rough approximation. The hydrological significance of the estimated ice volume was similar to that in rock glaciers in the Northern Tien Shan, but less important than in rock glaciers in the dry Andes.

Ice in permafrost related landforms is covered with debris and thus shielded from solar radiation. With ongoing global warming these landforms become more important in future regarding water supply. However, a better understanding of the structures and a quantification of the internal ice would permit a more detailed estimation of the hydrological significance.



## Acknowledgments

At first I would like to thank Tobias Bolch for the opportunity to write this thesis as well as for his excellent support, insightful discussions and the excitement for this topic. Throughout the thesis he was always available for helpful inputs and motivating words. Furthermore I would like to thank Stanislav Kutuzov (Russian Academy of Sciences, Russia) who gave us the opportunity to use his GPR device. His technical knowledge and his field experience were very helpful in the field. I would also like to thank Tino Pieczonka (TU Dresden, Germany) and Azamat Osmonov (CAIAG, Kyrgyzstan) for organising the field campaign and helping in the field. Special thanks for helping me in the field go to Paribesh Pradhan (University of Zurich, Switzerland), Ulrike Schinke and Benjamin Schroeter (TU Dresden).

I would also like to thank Leo Sold (University of Fribourg, Switzerland) for his help with GPR processing. In addition, I would like to thank Christin Hilbich and Martin Hoelzle (University of Fribourg) for fruitful discussions on GPR profile interpretation.

I want to thank my fellow students for inspiring discussions and motivating coffee breaks. I owe special thanks to my parents who supported me with my studies and thanks to my sisters. My greatest thanks are however dedicated to Anina Staeubli.



# Contents

<b>Abstract</b>	<b>III</b>
<b>Acknowledgments</b>	<b>V</b>
<b>List of Figures</b>	<b>X</b>
<b>List of Tables</b>	<b>XI</b>
<b>List of Abbreviations</b>	<b>XIII</b>
<b>1 Introduction</b>	<b>1</b>
1.1 Motivation . . . . .	1
1.2 Current Knowledge . . . . .	1
1.3 Objectives and Research Questions . . . . .	3
<b>2 Background</b>	<b>5</b>
2.1 Study Area . . . . .	5
2.2 Climate and Climate Change . . . . .	8
2.3 Permafrost and the Periglacial Environment . . . . .	10
2.3.1 Permafrost . . . . .	10
2.3.2 The Periglacial Environment . . . . .	11
2.4 Hydrology . . . . .	15
<b>3 Data</b>	<b>17</b>
3.1 SPOT-5 . . . . .	17
3.2 Landsat8 . . . . .	17
3.3 SRTM . . . . .	17
3.4 Glacier Inventory . . . . .	18
<b>4 Methods</b>	<b>19</b>
4.1 Rock Glacier Inventory . . . . .	19
4.1.1 Approach . . . . .	19
4.2 Geomorphological Map . . . . .	22
4.2.1 Process Domains . . . . .	22
4.2.2 Geodatabase Design . . . . .	23
4.2.3 Geomorphological Mapping . . . . .	23
4.3 Ground Penetrating Radar . . . . .	26

4.3.1	Background and Physical Principles . . . . .	26
4.3.2	Devices . . . . .	30
4.3.3	Data Acquisition . . . . .	31
4.3.4	Data Processing . . . . .	33
4.3.5	Subsurface Velocity Estimation . . . . .	37
<b>5</b>	<b>Results</b>	<b>41</b>
5.1	Rock Glacier Inventory . . . . .	41
5.1.1	Key Characteristics of Rock Glaciers . . . . .	41
5.1.2	Ice Content . . . . .	44
5.1.3	Rock Glacier to Glacier Ratio . . . . .	44
5.2	Geomorphological Map . . . . .	45
5.2.1	Surface Area of Process Domains . . . . .	45
5.2.2	Geomorphological Genesis of the Ice-Debris Complex . . . . .	46
5.3	Ground Penetrating Radar . . . . .	49
5.3.1	Glacier . . . . .	49
5.3.2	Medial Moraine . . . . .	54
5.3.3	Lateral Moraine . . . . .	60
5.3.4	Rock Glacier Tongue . . . . .	64
5.3.5	Glacio-Fluvial Plain . . . . .	72
<b>6</b>	<b>Discussion</b>	<b>75</b>
6.1	Structure of Landforms . . . . .	75
6.2	Genesis of the Landform Complex . . . . .	78
6.3	Ice Content . . . . .	79
6.4	Hydrological Significance . . . . .	82
<b>7</b>	<b>Conclusion and Outlook</b>	<b>85</b>
<b>A</b>	<b>Appendix</b>	<b>101</b>
A.1	Rock Glacier Inventory . . . . .	103
A.2	Geomorphological Map . . . . .	107
A.3	GPR Profiles Used in Thesis . . . . .	111
A.4	GPR Profiles Not Used in Thesis . . . . .	121
<b>B</b>	<b>Personal Declaration</b>	<b>129</b>

## List of Figures

1	Location of the study area . . . . .	5
2	Study area and area of detailed investigation . . . . .	6
3	The investigated ice-debris complex . . . . .	7
4	Monthly mean precipitation and temperature at the Tien Shan meteo station	8
5	Temperature trend at the Tien Shan meteo station . . . . .	9
6	Glacier and permafrost distribution in the Ak-Shiirak massif . . . . .	11
7	Glacial and periglacial landforms . . . . .	14
8	Overview of the main river systems . . . . .	15
9	The water divide at the study area . . . . .	16
10	Visualisation of the geomorphological legend . . . . .	25
11	Vertical and lateral resolution of GPR . . . . .	29
12	System design of Malå ProEx . . . . .	30
13	System design of VIRL-6 . . . . .	31
14	Common offset mode . . . . .	32
15	Overview of GPR profiles on the ice-debris complex . . . . .	33
16	Static correction . . . . .	34
17	Effects of different gain functions . . . . .	36
18	Hyperbola fitting . . . . .	38
19	The rock glacier inventory . . . . .	41
20	Key characteristics of the inventoried rock glaciers . . . . .	43
21	The geomorphological map . . . . .	45
22	Geomorphological Genesis of the Ice-Debris Complex . . . . .	47
23	Map of GPR profiles on the glacier . . . . .	50
24	Longitudinal profile G-L1 on the glacier . . . . .	51
25	Longitudinal and transverse profiles on the glacier . . . . .	53
26	Map of GPR profiles on the medial moraine . . . . .	54
27	Longitudinal profiles on the medial moraine . . . . .	57
28	Transverse profile on the medial moraine . . . . .	59
29	Map of GPR profiles on the lateral moraine . . . . .	60
30	GPR profiles on the lateral moraine . . . . .	63
31	Map of GPR profiles on the rock glacier tongue . . . . .	64
32	Longitudinal profiles on the rock glacier tongue . . . . .	67
33	Transverse profiles on the rock glacier tongue . . . . .	71
34	Map of GPR profiles on the glacio-fluvial plain . . . . .	72

35	GPR profiles on flood plain . . . . .	74
36	Internal structures of the investigated ice-debris complex . . . . .	75

## List of Tables

1	Warming trend coefficients for the Tien Shan . . . . .	9
2	Utilized remote sensing data . . . . .	18
3	Typical electrical properties in common earth surface . . . . .	28
4	Uncertainty at the time to depth conversion . . . . .	38
5	Comparsion of glacier and rock glacier area . . . . .	42
6	Key characteristics of rock glaciers . . . . .	42
7	Ice content of glaciers and rock glaciers . . . . .	44
8	Ratio of rock glacier to glacier ice volume . . . . .	44
9	Distribution of the surface area of the geomorphological process domains . .	46
10	Subsurface velocities of GPR profiles . . . . .	81
11	Hydrological significance of rock glaciers as water stores worldwide . . . . .	83



## List of Abbreviations

<b>AGC</b>	Automatic gain control
<b>ASTER</b>	Advanced spaceborne thermal emission and reflection radiometer
<b>CMP</b>	Common mid-point
<b>CO</b>	Common offset
<b>CRU</b>	Control and recording unit
<b>DEM</b>	Digital elevation model
<b>ELA</b>	Equilibrium line altitude
<b>ERT</b>	Electrical resistivity tomography
<b>fk</b>	Frequency-wavenumber
<b>GlabTop</b>	Glacier bed Topography
<b>GLIMS</b>	Global land ice measurements from space
<b>GPR</b>	Ground penetrating radar
<b>GPS</b>	Global positioning system
<b>LIA</b>	Little ice age
<b>MAAT</b>	Mean annual air temperature
<b>RES</b>	Radio echo sounding
<b>RTA</b>	Rough terrain antenna
<b>RX</b>	Receiver
<b>SPOT</b>	Système pour l'observation de la terre
<b>SRTM</b>	Shuttle radar topography mission
<b>TWT</b>	Two-way traveltime
<b>TX</b>	Transmitter
<b>WARR</b>	Wide-angle reflection and refraction
<b>WGS</b>	World geodetic system



# 1 Introduction

## 1.1 Motivation

Human caused climate change is unequivocal and its impacts on natural and human systems are evident on a global scale (IPCC, 2014).

One of the best known indicators of global warming are glacier length changes (Haeberli, 2005*b*; Kääb et al., 2007; Oerlemans, 2005). As a consequence of global warming, glaciers show increased melting and are retreating (Bolch et al., 2012; Haeberli and Beniston, 1998; Kutuzov and Shahgedanova, 2009; Oerlemans, 2005). Glaciers play an important role as water reservoirs in the hydrological cycle, especially for arid, densely populated lowlands (Immerzeel et al., 2010; Viviroli et al., 2007). The glacier retreat will therefore lead to an earlier runoff maximum and an increased water shortage, especially in summer, when the need for water is highest (Barnett et al., 2005). Enhanced precipitation or thawing permafrost could potentially compensate the reduced summer discharge (Bolch and Marchenko, 2009; Sorg et al., 2012).

In dry areas, ice-rich permafrost is considered to contain a significant amount of ice, especially in periglacial areas, where a blocky environment offers favourable thermal conditions for buried ice to occur. Permafrost related landforms like ice-cored moraines or rock glaciers contain an ice content of about 50% (Arenson et al., 2002; Barsch, 1996; Burger et al., 1999). Ice stored in permafrost should therefore be considered to get a more realistic assignment of the mountainous reservoir capacity, especially in dry areas.

In the Tien Shan mountains of Central Asia several massive creeping permafrost bodies are apparent below glaciers. These complex landform assemblages are considered to contain a significant amount of ice (Bolch and Marchenko, 2009). Previous Ground Penetrating Radar (GPR) measurements on such an ice-debris complex showed clear indicators for several hundred meters of buried massive ice (Bolch et al., 2015). In order to estimate the ice content and the hydrological importance of these features, the internal structures and geomorphological characteristics are investigated of an ice-debris complex in the Ak-Shirak massif in the Central Tien Shan.

## 1.2 Current Knowledge

The distinct ice-debris complexes were a well known phenomenon in the former Soviet era. In modern times, the ice-debris complexes are generally regarded as common rock

glaciers.

A similar ice-debris complex in the Chilean Andes was regarded as a depositional landform assemblage resulting from glacier-permafrost interactions during the late Pleistocene-Holocene glacier advances (Monnier et al., 2014). In contrast, rock glaciers are defined as lobate or tongue-shaped bodies of perennially frozen unconsolidated material supersaturated with interstitial ice and ice lenses that move downvalley by creep as a consequence of the deformation of ice contained in them and which are, thus, features of cohesive flow (Barsch, 1992). Hence, rock glaciers can be regarded as a part of an ice-debris complex with pronounced geomorphological creep characteristics. An ice-debris complex, however describes a landform continuum as the result of periglacial and glacial interactions (cf. Etzelmuller and Hagen (2005); Giardino and Vitek (1988)).

Rock glaciers are thought to be either of glacial origin (e.g. Evans (1993); Humlum (1996); Whalley and Azizi (1994); Whalley et al. (1995)) or of periglacial origin (e.g. Barsch (1977, 1992); Haeberli (1985); Haeberli et al. (2006); Wahrhaftig and Cox (1959)). Glacier derived rock glaciers originate below glaciers and form of glacier ice and rock fall debris (Humlum, 1996); in contrast, periglacial rock glaciers are thought to be the result of rock fall and avalanche deposits (Haeberli et al., 2006). In the Northern Tien Shan, the distribution and characteristics of rock glaciers are related to the interaction with polythermal glaciers, topographic characteristics, intensive weathering and rock avalanches triggered by seismic activity (Bolch and Gorbunov, 2014).

The internal structure of rock glaciers is usually described as a two-layer model. Rock glaciers are composed of an outer layer consisting of blocky, ice-poor sediments and an inner core, built up by an ice-rich, fine-grained debris matrix (e.g. Burger et al. (1999); Haeberli (1985); Ikeda and Matsuoka (2002); Wahrhaftig and Cox (1959)). The internal structures of rock glaciers are best investigated using geophysical methods like electrical resistivity tomography (ERT) (e.g. Farbroth et al. (2005); Hauck et al. (2003); Isaksen et al. (2000); Leopold et al. (2011)), refraction seismics (e.g. Maurer and Hauck (2007); Springman et al. (2012); Vonder Mühll et al. (2002)) or GPR (e.g. Berthling et al. (2000); Degenhardt (2009); Hausmann et al. (2007)). Often a combination of several geophysical methods is applied (e.g. Hausmann et al. (2007); Maurer and Hauck (2007)). Other studies used boreholes to investigate the internal structures of rock glaciers (e.g. Fukui et al. (2008); Monnier et al. (2013); Vonder Mühll and Holub (1992); Vonder Mühll et al. (2003)). These studies help to better understand the rock glacier kinematics, thermal conditions, and the ice content of the different layers.

### 1.3 Objectives and Research Questions

The potential of permafrost related, ice-rich landforms to compensate the decrease in glacier derived discharge and huge ice-debris complexes probably containing a considerable amount of buried ice lead to the following main scientific aims and research questions:

1. Estimation of the hydrological significance of the ice-rich permafrost
  - How can the hydrological significance of ice-rich permafrost be estimated?
  - How many rock glacier features are found in the study area?
  - What is the glacier/rock glacier portion?
  - How do rock glaciers contribute to the water storage in the study area?
  
2. Estimation of the ice content of an ice-debris complex
  - How can the ice content of an ice-debris complex be estimated?
  - How much ice do the different landform parts contain?
  
3. Investigation of the origin of an ice-debris complex
  - How was the ice-debris complex formed?
  - How is the ice-debris complex geomorphologically characterised?
  
4. Investigation of the internal structures of an ice-debris complex
  - How are the internal structures of an ice-debris complex characterised?
  - How can the internal structures and patterns be interpreted?



## 2 Background

### 2.1 Study Area

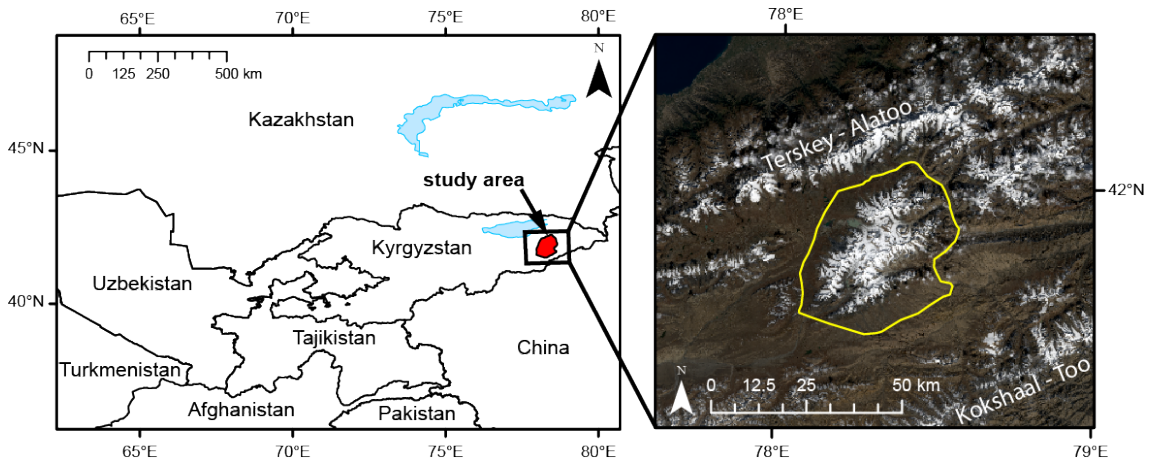


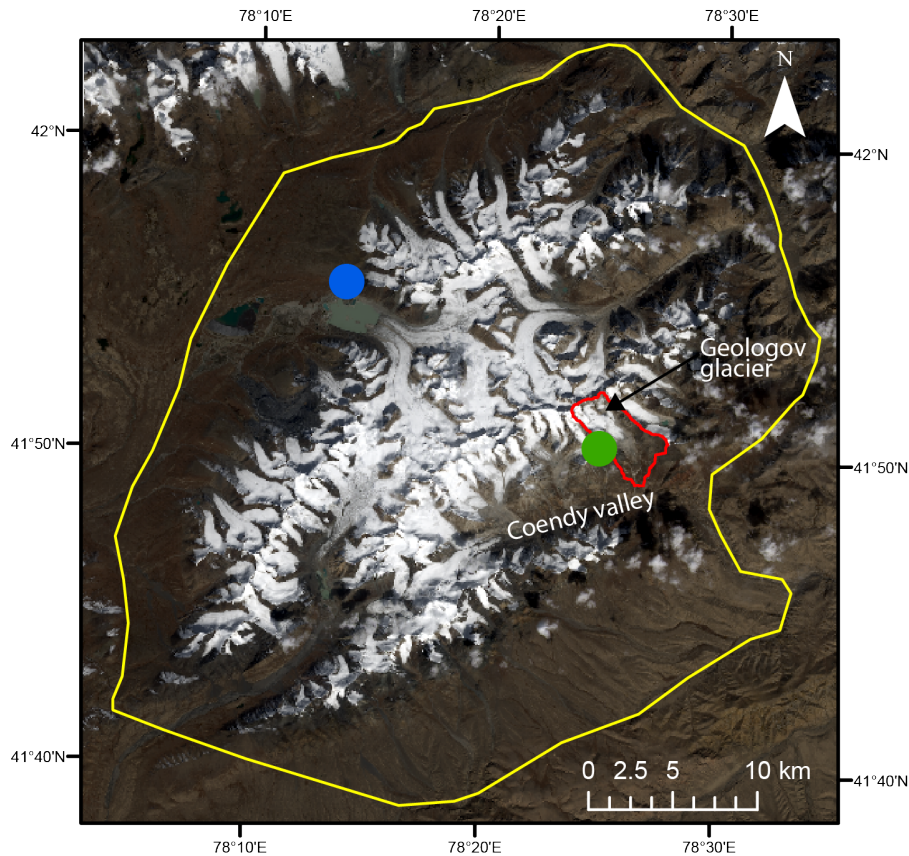
Figure 1: Location of the study area, delimited by the yellow line (right map is based on a Landsat8 scene)

The study area is situated in the Ak-Shiirak massif, in the eastern part of Kyrgyzstan (about  $41^{\circ}50'N$ ;  $78^{\circ}25'E$ ) (see figure 1). The Ak-Shiirak massif is part of the Tien Shan (Chinese for 'Celestial Mountains') a 2500km long and 400km wide mountain range in Central Asia. The Ak-Shiirak massif is located on a mountain plateau, delimited by the Terskey-Alatoo range in the north and the Kokshaal-Too range in the south (see figure 1). The Ak-Shiirak is an island-like massif, with its main ridges in south-western-to-north-eastern direction. The altitude ranges from 3500m a.s.l. (mountain plateau) up to 5000m a.s.l. The Ak-Shiirak massif is the second largest glacierized massif in Tien Shan, comprising of 178 glaciers (see figure 6). The glacierized area is about  $317\text{km}^2$  (status 2003), of which 87% is covered by large valley glaciers (Aizen et al., 2007; Kuzmichenok, 1989) (in Kutuzov and Shahgedanova (2009)). Glaciers occur on all sides of the Ak-Shiirak massif but are most pronounced on the northern aspect. Beside glaciers, several rock glacier like ice-debris complexes are evident. These ice-debris complexes are mainly occurring below large valley glaciers and are most distinct on southern aspects. The ice-debris complexes are large landform features and describe transition features consisting of debris covered glaciers, ice-cored moraines and typical rock glacier tongues.

The study area was delimited by surrounding rivers, the Sary-Chat river in the north and east, the Kumtor river in the north-west and the Ak-Tash river in the south. Between

the river systems the boundary line was drawn manually (see the yellow boundary line in figure 2).

Detailed investigations were done in a tributary valley of the Coendy valley (see the red boundary line in figure 2) in the south-eastern margin of the Ak-Shiirak massif. The tributary valley is dominated by the Geologov glacier and an adjacent huge ice-debris complex (see figure 3). The area of detailed investigations was delimited by the hydrological watershed and was selected due to its representativeness and its accessibility.



**Legend**

- Area of detailed investigations
- Study Area
- Meteo Station "Coendy"
- Meteo Station "Tien Shan"

Figure 2: Study area and area of detailed investigation (map is based on a Landsat8 scene)



Figure 3: The investigated ice-debris complex below Geologov glacier, as seen in eastern direction (own photo 2014)

## 2.2 Climate and Climate Change

The climate in the Tien Shan is determined by the interaction of the Siberian anticyclone and cyclonic activity in the West (Aizen et al., 1997). The Northern Tien Shan ranges act as a climate barrier. Thus, areas in the rain shadow of the Northern Tien Shan show a continentality gradient with decreasing precipitation and mean temperatures towards the south-west (Dyurgerov et al., 1993) (in Sorg et al. (2012)). The Ak-Shiirak is additionally encapsulated by the Terskey-Alatoo and the Kokshaal-Too ranges and shows pronounced continental climate. At the Tien Shan meteo station (3614m a.s.l.)(see figure 2), the mean annual air temperature (MAAT) is  $-7.4^{\circ}\text{C}$  and the mean annual precipitation is 311mm (period from 1930-2013). Precipitation is most pronounced in summer. About 67% of precipitation occur between May and September, with its maximum in July (see figure 4). Low precipitation in winter is caused by the prominent Siberian anticyclone, blocking the humid westerlies (Böhner, 2006) (in Bolch (2007)). The maximum mean monthly temperature is  $4.5^{\circ}\text{C}$  in July. The temperature drops to  $-21^{\circ}\text{C}$  in January (see figure 4). Measurements at the Coendy meteo station (see figure 2) close to the investigated ice-debris complex, exist for a one year period (09/13-09/14). The measured MAAT is  $-4.35^{\circ}\text{C}$ . The maximum temperature was reached in August ( $4.9^{\circ}\text{C}$ ) and minimum temperature in February ( $-16^{\circ}\text{C}$ ).

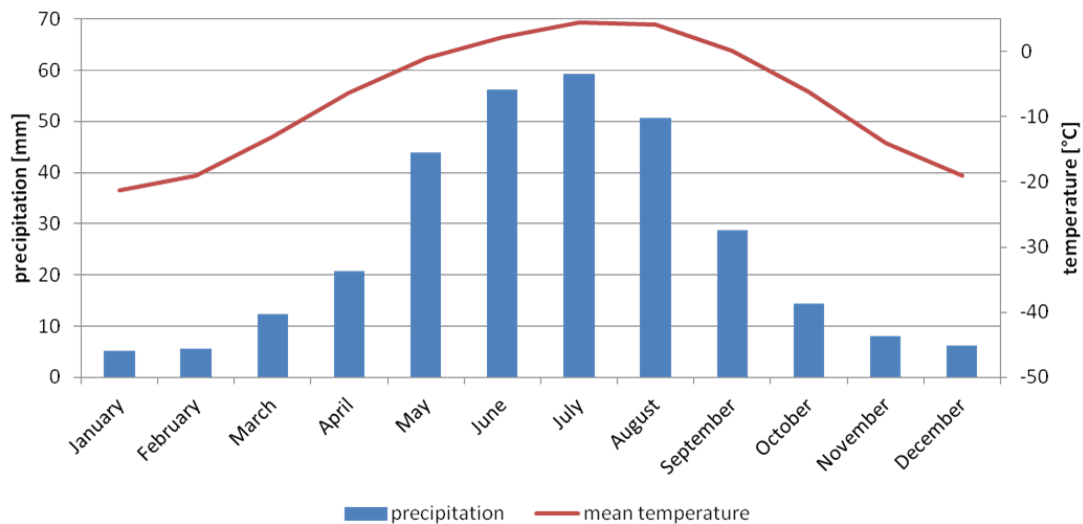


Figure 4: Monthly mean precipitation and temperature (1930-2013) at the Tien Shan meteo station (3614m a.s.l.); data source: (Giese, 2004) published in (Giese and Mossig, 2004)

Global climate change is also visible in the Tien Shan. Bolch (2007) evaluated 16 climate stations in the Tien Shan and showed a clear temperature increase in the last century, especially in the second half of it. The warming trend coefficient for the Tien Shan is between 0.8K/100y and 2K/100y, depending on the evaluated period (see table 1).

Table 1: Warming trend coefficients for the Tien Shan

Warming trend	Period	Author
0.8K/100y	1900-2000	Bolch (2007)
1K/100y	1940-1991	Aizen et al. (1997)
2K/100y	1950-2000	Bolch (2007)

At the Tien Shan meteo station, a warming trend of 0.79K/100y was calculated for the period of 1930-1996 (see figure 5). More recent temperature data at Tien Shan meteo station was not used, because the location of the meteo station was changed in 1997.

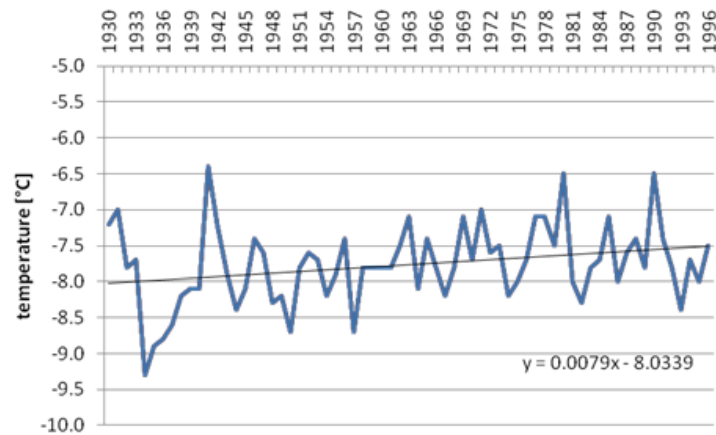


Figure 5: Temperature trend at the Tien Shan meteo station 1930-1996; data source: (Giese, 2004) published in (Giese and Mossig, 2004)

Temperature warming is most pronounced in autumn and winter and in areas below 2000m a.s.l. (Aizen et al., 1997; Bolch, 2007). For precipitation, no clear trend is apparent (Bolch, 2007).

## 2.3 Permafrost and the Periglacial Environment

### 2.3.1 Permafrost

A distinct characteristic of high mountain areas is the occurrence of permafrost. In areas where the MAAT is close to 0°C or below, permafrost is likely to occur. In continental climates, permafrost distribution is mainly depending on short-wave solar radiation, mean annual air temperature, and evaporation (Marchenko, 2001). Beside this, elevation, slope and aspect, as well as vegetation, snow cover, moisture, and ground water content are influencing the regional permafrost distribution. Coarse and blocky materials create favourable thermal conditions for permafrost to occur. Creeping permafrost bodies like rock glaciers or ice-cored moraines are thus distinct permafrost indicators.

According to Gorbunov et al. (1996) (in (Marchenko et al., 2007)), continuous permafrost occurs above 3600m a.s.l., discontinuous permafrost between 3600-3300m a.s.l and sporadic permafrost between 3300-2800m a.s.l. in the Central Tien Shan. Thus, in the Ak-Shiirak massif, favourable thermal conditions exist and permafrost is therefore a widespread phenomenon (see figure 6), influencing the periglacial geomorphology, slope stability, and frozen water storage.

In figure 6, permafrost favourable conditions are marked in blue and purple. Areas where permafrost occurs only in very favourable conditions are marked in red and yellow. The permafrost distribution is modelled as a function of the MAAT in a global permafrost zonation model of Gruber (2012).

With ongoing climate change permafrost thawing and degradation will continue, leading to slope instability and enhanced rock fall events (Haeberli and Beniston, 1998) as well as an increased water discharge from melting ice-rich permafrost bodies (Bolch and Marchenko, 2009; Sorg et al., 2012). In the Northern Tien Shan the permafrost temperature increased by 0.3-0.6°C in the last 30 years and the average thickness of the active layer increased by 23 % since the 1970ies (Marchenko et al., 2007). The lower permafrost boundary has shifted upward by 150-200m in the twentieth century (Marchenko et al., 2007).

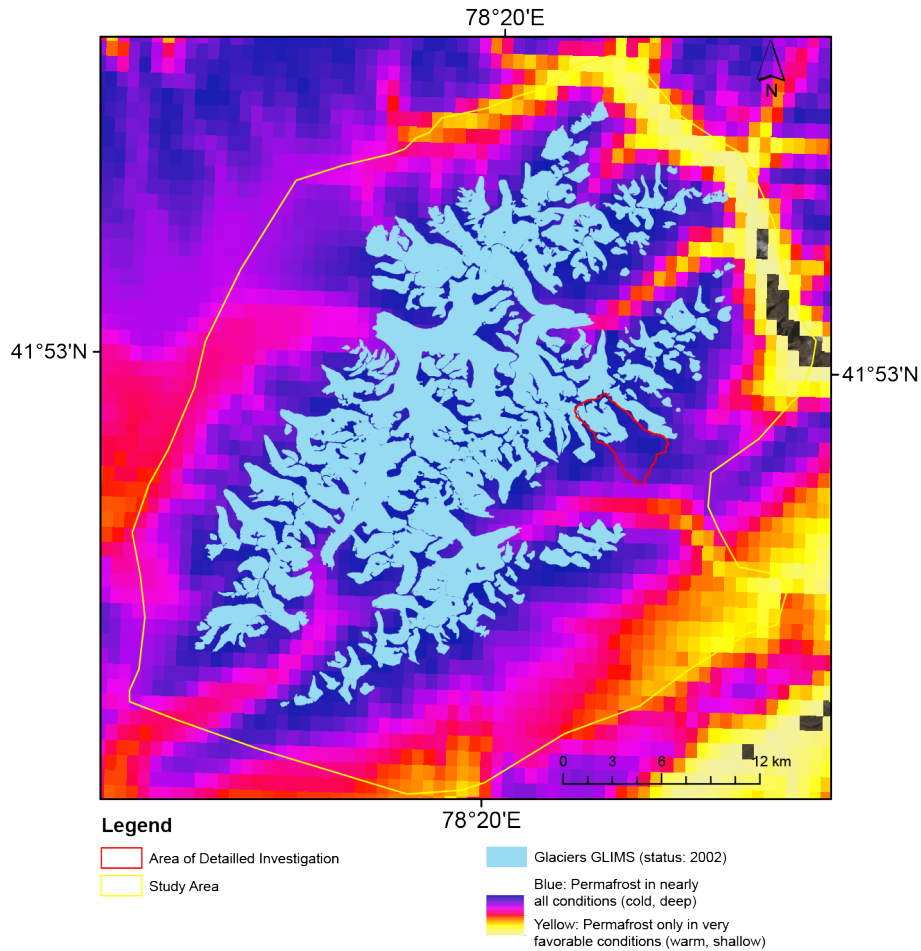


Figure 6: Glacier and permafrost distribution in the Ak-Shiirak massif (Glaciers based on GLIMS: (Khromova, 2005); Permafrost distribution based on the global permafrost zonation model of Gruber (2012))

### 2.3.2 The Periglacial Environment

Periglacial environments are regions with cold and generally non-glacial conditions, in which frost-related processes or permafrost are either dominant or characteristic (French, 2007).

Periglacial processes are due to seasonal or diurnal freezing and thawing of the ground, such as cryoturbation and gelifluction (Washburn, 1973). Periglacial environments are thus found in many high-mountain regions of all latitudes and are closely related to permafrost areas or glacial environments. When investigating periglacial processes, the glacial environment has to be considered as well.

There is a close interaction between the glacial and the periglacial system, affecting all chains of the sediment cascade system within landform evolution (Etzelmuller and Hagen, 2005). When investigating geomorphological processes and the response of the system to climate change, glaciers and permafrost systems must be regarded as an integrated part (Etzelmuller and Hagen, 2005).

In the Ak-Shiirak a glacial-periglacial landform complex consisting of several distinct periglacial landforms was investigated. The most prominent landforms are explained and an example is shown in figure 7.

### **Glacier**

A glacier (see figure 7a) is defined as a mass of surface-ice on land which flows downhill under the influence of gravity and is constrained by internal stress and friction at the base sides. Glaciers are controlled by the accumulation of snow in high-altitudes and ablation in low-altitudes (UNEP, 2007).

### **Moraine**

Moraine (see figure 7b) is a genetic term for a landscape element formed by deposition and/or deformation in glacial environments. Usually, moraines are described as ridge-shaped glacial landforms. Moraines consist of unconsolidated sediments, directly deposited or deformed and accumulated by glaciers (Schomacker, 2011).

Lateral moraines are ridges of supraglacially deposited debris located along the sides of valley glaciers. In modern glacial environments, lateral moraines might be ice cored (see next subsection). Medial moraines are ice-flow parallel debris ridges on the surface of glaciers. Medial moraines are the surface expression of englacial debris. Medial moraine material will deposit at the glacier tongue due to glacial melt. Lateral and medial moraines form only below the equilibrium line altitude ELA (Schomacker, 2011).

### **Ice-Cored Moraine Complex**

Ice-cored moraines (see figure 7c) are ice-marginal landforms that comprise a discrete body of glacier ice buried underneath sediment (Lukas, 2011). Ice-cored moraines evolve through the isolation of a body of glacier ice, triggered by the establishment of a debris cover which shields ice from melting. Other possibilities are differential melting of protected sediment-covered ice and clean ice, or the cut off from active ice, leading to stagnant or dead ice bodies (Lukas, 2011).

The main geomorphological characteristics of ice-cored moraines are a rounded surface and outlines with minor ridges superimposed on it. The appearance is slightly slumping

but no pronounced fractures are visible. Ice-cored moraines are a fairly stable landform and generally no fresh scree is visible on the slopes (Ø strem and Arnold, 1970). Often permanent snow banks on the proximal side are a sign indicating ice-cored moraines. Excavated ice cliffs are another sign for moraines containing massive ice lenses.

### **Rock Glacier**

”Active rock glaciers (see figure 7d) are lobate or tongue-shaped bodies of perennially frozen unconsolidated material supersaturated with interstitial ice and ice lenses that move downslope or downvalley by creep as a consequence of the deformation of ice contained in them and which are, thus, features of cohesive flow” (Barsch, 1992). In a more genetic definition, rock glaciers are defined as the visible expression of cumulative deformation by long-term creep of ice/debris mixtures under permafrost conditions (Berthling, 2011).

The main geomorphological characteristics of rock glaciers are the steep ( $\geq 30^\circ$ ) and relatively light-coloured front and side slopes. On the upper surface, pronounced transverse or longitudinal furrows and ridges are visible (Barsch, 1996). Both characteristics are a result of the creep behaviour of rock glaciers and are an indicator for internal ice.

### **Glacio-Fluvial Plain**

Glacio-fluvial sediments are deposited by glacier melt-streams, in either ice contact or proglacial settings (Benn and Evans, 1998). Glacio-fluvial plains (see figure 7e) are the area where glacio-fluvial sediments are deposited. Glacier-fed rivers show pronounced diurnal and annual changes in discharge and commonly entrain a substantial supply of coarse, cohesion less sediment. The entrainment of sediment is highly episodic and increasing with rising discharge (Benn, 2009).

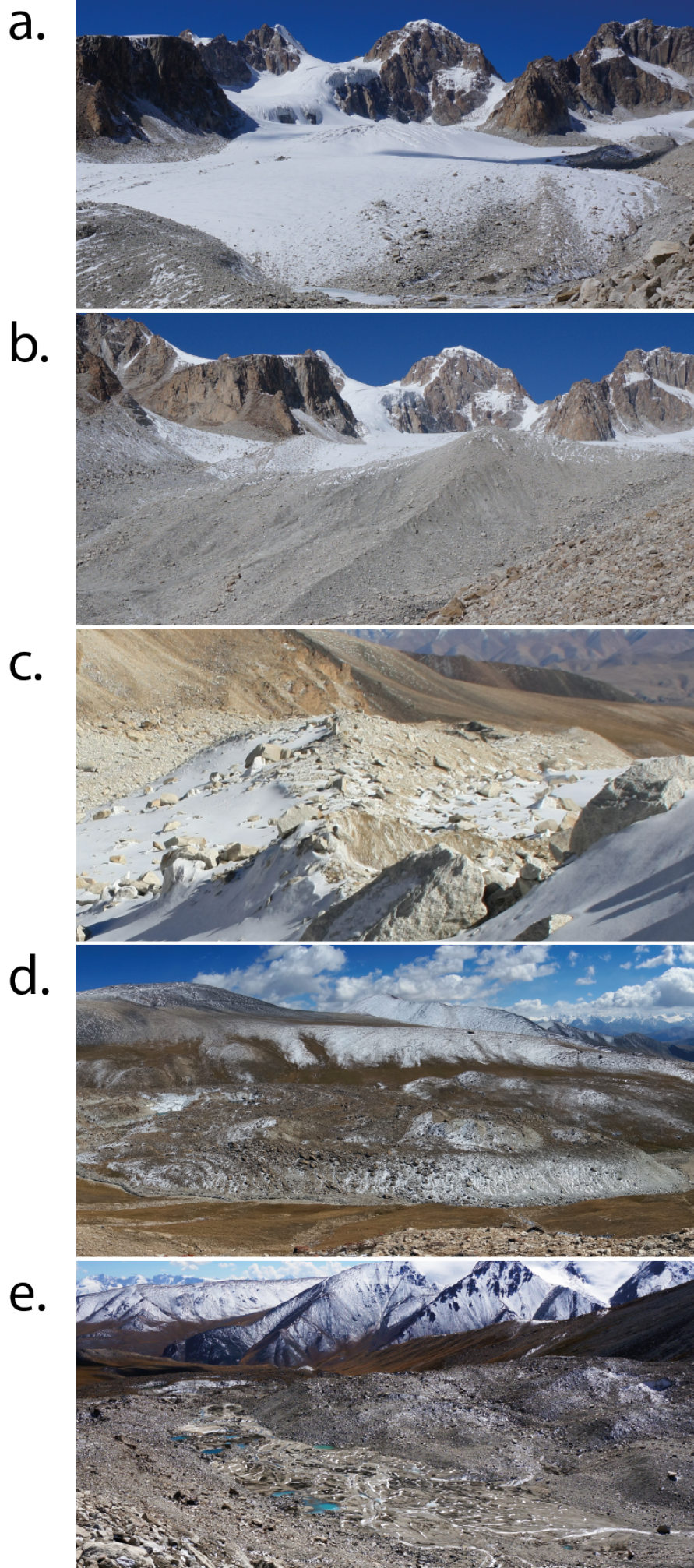


Figure 7: Glacial and periglacial landforms: a. glacier; b. medial moraine; c. ice-cored moraine complex; d. rock glacier; e. glacio-fluvial plain (own photos 2014; c: U. Schinke)

## 2.4 Hydrology

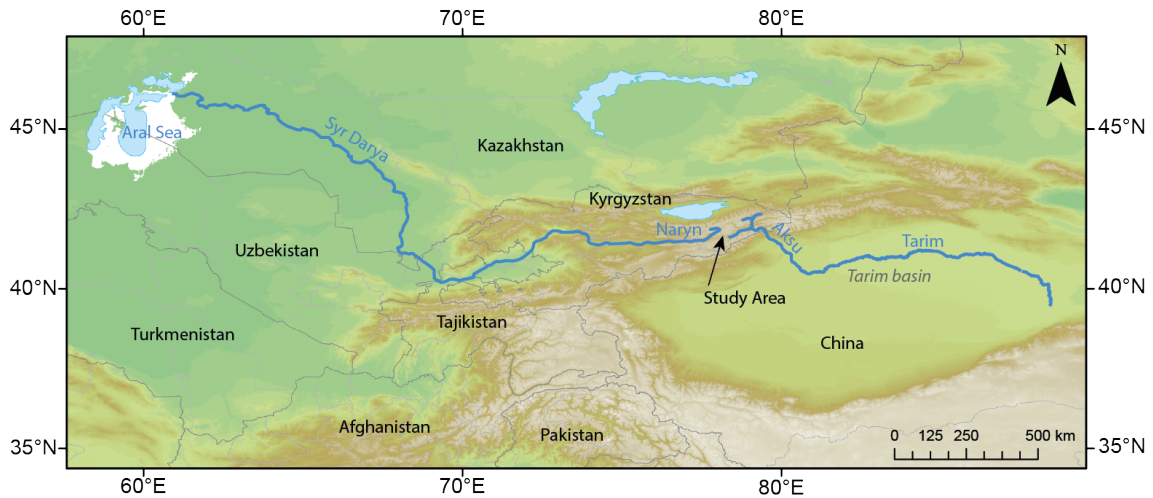


Figure 8: Overview of the main river systems: Naryn-Syr Darya and Aksu-Tarim

The study area in the Ak-Shiirak massif is located at a water divide. The south facing slopes including the Coendy valley are draining into the Aksu-Tarim catchment. The northern and western part of the Ak-Shiirak massif are draining into the Naryn-Syr Darya catchment (see figure 9).

The Syr Darya river originates at the confluence of the Kara Darya and the Naryn river. The Naryn river originates in the study area. The Syr Darya river has a total length of more than 3000km and is eventually draining into Aral Sea. Glacial runoff contributes between 6% (Mamatkanov, 2006; Kuzmichenok, 2009) (in (Sorg et al., 2012)) and 10% (only Naryn basin) (Aizen et al., 1995) to the total runoff.

In the arid lowlands of the Syr Darya people are relying on irrigated agriculture. Depletion of water resources of the Syr Darya have led not only to the almost disappearance of the Aral Sea (Micklin, 1988), but since the collapse of the Soviet Union also to political tensions (Smith, 1995).

The Tarim river originates at the confluence of the Aksu (originating in the study area), Yarkant, Kaxgar and Hotan river and is ending in a barrier lake in the eastern part of the Tarim basin (see figure 8). The total length of the Tarim river is more than 2000km.

Glacial runoff contributes between 33% (only Aksu river) (Aizen et al., 1995) and 46-48% (Dikikh, 1993; You, 1995) (in Xu et al. (2009)) for the whole Aksu-Tarim basin. (Pieczonka and Bolch, 2015) estimated the contribution to the total runoff due to glaciers imbalance to be about 20% between 1975-2000 for the Aksu catchment. In the dry Tarim basin

glacier derived runoff is extremely important for irrigation, hydro power and drinking water supply (Krysanova et al., 2014; Kundzewicz et al., 2014).

Ongoing climate change will likely influence the runoff seasonality with earlier snow melt and less glacier melt. This could eventually increase water stress in the arid lowlands (Siegfried et al., 2012) and lead to political conflicts on water allocation (Bernauer and Siegfried, 2012).

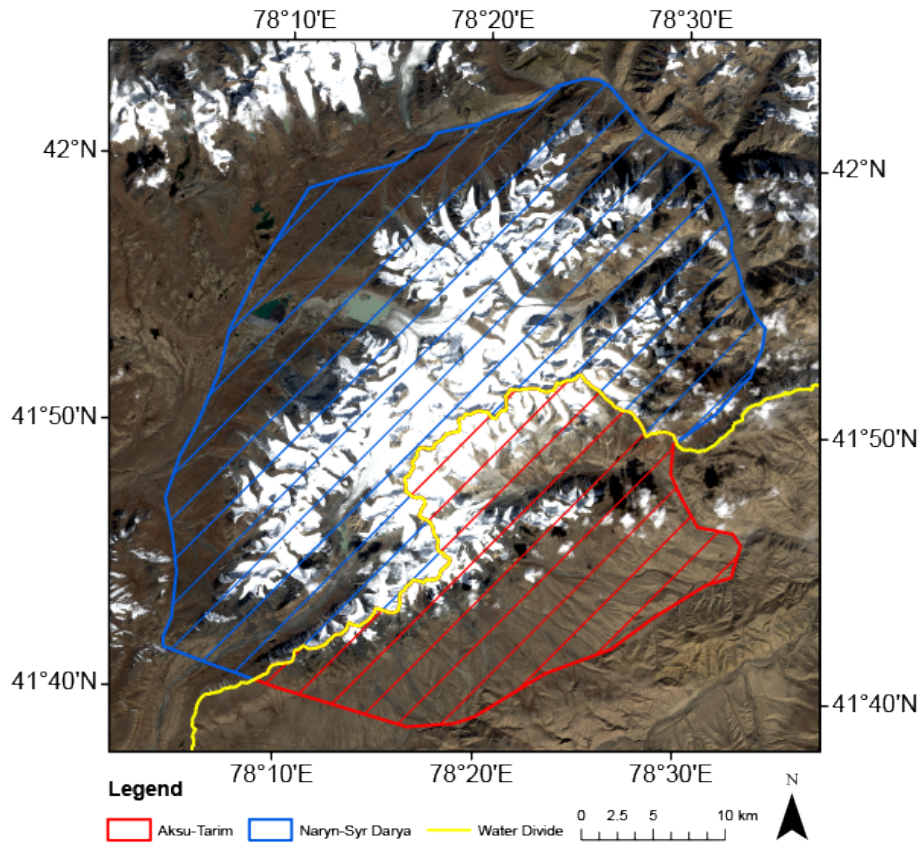


Figure 9: The water divide at the study area (map is based on a Landsat8 scene)

## 3 Data

The following data was used in order to create a rock glacier inventory and a geomorphological map.

### 3.1 SPOT-5

SPOT-5 (Systeme pour l'observation de la terre) is a satellite, equipped with two high resolution geometrical instruments, offering high resolution remote sensing images. Panchromatic images with 2.5 to 5m spatial resolution and multispectral images with 10m spatial resolution respectively are available. For the study area, a 5m panchromatic scene was used, taken on September 25 2013 (see table 2). The scene covers an area of  $60 \times 69 km^2$ .

### 3.2 Landsat8

Landsat8 is an American satellite providing multispectral images. The satellite was launched in February 2013 and covers the entire earth surface every 16 days (USGS, 2015). Landsat8 images have a spatial resolution of 15m (panchromatic) and 30m (multispectral) respectively (see table 2). Images are in the World Geodetic System WGS1984 datum (USGS, 2015). The image used in this study covers an area of  $190 \times 196 km^2$  and was taken on October 2 2013 (see table 2).

### 3.3 SRTM

Shuttle Radar Topography Mission (SRTM) provides a near global Digital Elevation Model (DEM) with a resolution of 3 arcseconds (90m) and 1 arcsecond (30m) for some regions. The SRTM DEM was acquired using radar interferometry and was recorded in February 2000 (Farr et al., 2007). For the study area, a  $85 \times 113 km^2$  scene with 1 arcsecond spatial resolution was available. The scene was taken on Februar 11 2000 (see table 2).

Validation using ground control points revealed a vertical and horizontal error of approximately 10m (Farr et al., 2007).

Table 2: Utilized remote sensing data

<b>Sensor</b>	<b>SPOT-5</b>	<b>Landsat8</b>	<b>SRTM</b>
Spatial Resolution	5m	15m (panchromatic) 30 (multispectral)	1arcsec(30m)
Date	25/9/2013	2/10/2013	11/2/2000
Coverage	$60 \times 69 km^2$	$190 \times 196 km^2$	$85 \times 113 km^2$

### 3.4 Glacier Inventory

The Global Land Ice Measurement from Space (GLIMS) project has the goal of inventorying a majority of the world's glaciers. The project is a cooperation of several institutions world-wide (Raup et al., 2007). Glacier mapping was mainly based on satellite data. The glaciers in the Ak-Shirak massif were mapped on an Advanced Spaceborne Thermal Emission and Reflection Radiometer (ASTER) scene. The ASTER satellite image was taken on October 3 2002. Thus, the mapped glaciers show the glacial extent of 2002. Mapping was done by members of the Russian Academy of Sciences (Khromova, 2005).

## 4 Methods

### 4.1 Rock Glacier Inventory

In order to estimate the hydrological significance of the ice-rich permafrost, all ice-rich permafrost features have to be mapped, their thickness and ice content have to be estimated. The mapping and characterisation of permafrost depth and distribution requires integrated multiple geophysical approaches (Harris et al., 2009). However, such a detailed investigation was not possible in the scope of this thesis and thus a more proximate approach was chosen. To estimate the hydrological significance of the ice-rich permafrost, rock glaciers, as the visible permafrost indicators were mapped and their thickness and ice content were estimated using a rough approximation.

This rock glacier inventory aims to detect and map all typical rock glacier features in the Ak-Shiirak massif. Based on the rock glacier inventory, the evaluation of the spatial rock glacier distribution and the estimation of the total ice stored in rock glaciers will be evaluated.

Similar approaches using rock glaciers have been carried out mainly in the European Alps e.g. (Curtaz et al., 2011; Frauenfelder et al., 2003; Guglielmin and Smiraglia, 1998; Kellerer-Pirklbauer et al., 2012; Krainer and Ribis, 2012; Nyenhuis et al., 2005; Scotti et al., 2013) and in the Andes e.g. (Brenning, 2005; Esper Angillieri, 2009; Falaschi et al., 2014; Rangecroft et al., 2014). In Asia only few rock glacier inventories exist e.g. (Bolch, 2004; Bolch and Marchenko, 2009; Gorbunov, 1998; Ishikawa, 2002). For the Central Tien Shan region, no rock glacier inventory exist so far. This inventory is thus of special interest.

#### 4.1.1 Approach

All rock glaciers in the Ak-Shiirak massif were mapped using high-resolution satellite images. To compare the mapped rock glaciers with the glacier extent, an existing glacier inventory was used (see section 3.4). The study area was delimited by the surrounding rivers (see figure 2 in section 2.1).

Since rock glaciers have similar spectral properties as their surroundings, an automatic delineation of rock glaciers from remote sensing data is difficult (Brenning, 2009). Therefore, rock glaciers were identified manually on remote sensing images. The following geomorphological characteristics of rock glaciers (based on Barsch (1996)) were used:

- Steep ( $\geq 30^\circ$ ) and relatively light-coloured front and side slopes
- A darker, bouldery surface with furrows and ridges

- The mean gradient of the upper surface is much less than that of the front and side slopes
- The upper end may either grade into a steep talus slope or be a depression between the talus slope and the rock glacier

The remote sensing data used for mapping were a SPOT-5 panchromatic satellite image and a Landsat8 satellite image. Additionally, GoogleEarth was used to check and verify. The high-resolution GoogleEarth image in the study area, is a QuickBird satellite image, taken in 2002. The QuickBird image has a spatial resolution of 0.6m (panchromatic) and 2.4m (multispectral). Even on high-resolution images with a spatial resolution of 0.6m, the detection of rock glaciers is not easy. Especially the upper delineation of rock glaciers is difficult and the distinction between rock glaciers and other periglacial features needs a lot of experience.

To compare the inventoried rock glaciers, glacier outlines based on the GLIMS database were used. The manual mapping was done in ArcGIS. The features were stored in a geodatabase. All features were projected to the WGS\_1984\_UTM\_Zone\_44N.

The following parameters were calculated for every rock glacier feature:

- Minimum altitude at the front [m]
- Maximum altitude of rock glacier [m]
- Elevation range of altitude [m]
- Length [m]
- Width [m]
- Area [m<sup>2</sup>]
- Slope [°]
- Aspect

The geomorphometry was based on a SRTM DEM with 30m spatial resolution. In the northern part of the study area, a SRTM DEM with 90m spatial resolution only, was available. The 90m DEM was thus scaled down to a spatial resolution of 30m. Altitude, elevation range, length, width and area were directly measured as parameters from rock glacier polygons. Slope was calculated as the arctangent function of the ratio of elevation range of altitude and rock glacier length. The mean aspect was calculated in ArcGIS.

The estimation of the glacier ice volume was based on the glacier ice thickness model GlabTop (Glacier bed Topography). GlabTop is based on an empirical relation between the average basal shear stress and the elevation range of individual glaciers, calibrated with geometric information from paleoglaciers, and validated with radio echo soundings on contemporary glaciers (Linsbauer et al., 2012). The modelled glacier thickness showed a spatial resolution of 30m. The glacier ice-thickness modelling was done by Andreas Linsbauer and Tobias Bolch.

To estimate the ice content of rock glaciers, the thickness of the ice-rich layer of every rock glacier had to be calculated. The thickness of the ice-rich layer was calculated with a commonly used estimation (cf. Brenning (2005)) (see equation 1). The ice volume of the ice-rich permafrost was assumed to be 50% (Arenson et al., 2002; Barsch, 1996; Burger et al., 1999).

The manual mapping of rock glaciers on satellite images is rather inaccurate. The uncertainty due to sampling variance in a similar study was in the order of -50% to +100% (Azócar and Brenning, 2010). Similar uncertainties could be expected.

$$h = 50 \times A^{0.2} \tag{1}$$

where:

- h = Thickness of ice-rich rock glacier permafrost [m]
- A = Rock glacier area [km<sup>2</sup>]

## 4.2 Geomorphological Map

In order to investigate the formation and geomorphological characterisation of an ice-debris complex, a geomorphological map has to be created.

Geomorphological maps can be considered graphical inventories of a landscape depicting landforms and surface as well as subsurface materials (Otto and Smith, 2013). Geomorphological mapping is the attempt to quantitatively and qualitatively characterise the properties of earth's surface (Demek, 1976). A geomorphological map should therefore present a full picture of the landscape and contain information about the distribution and correlations of forms of a certain appearance, size, origin and age. It must include morphographic, morphometric, morphogenetic and morphochronologic data (Klimaszewski, 1982) (in Gustavsson et al. (2006)).

Geomorphological mapping is a crucial tool in land management, risk management, environmental, scientific and engineering purposes. In this study, the main aim of geomorphological mapping is to visualise the dominant process domains and to better understand the origin and the genesis of an ice-debris complex.

### 4.2.1 Process Domains

Process domains are spatially identifiable areas characterised by distinct suites of geomorphological processes (Montgomery, 1999). In process domains, one or a collection of natural processes are dominating the shaping of earth surface (Brardinoni and Hassan, 2006).

#### Glacial Process Domain

Processes and landforms assigned to the glacial process area are directly formed by glaciers or glacier motion. This process domain contains the following geomorphological features: *glacier*, *supraglacial debris*, *moraine accumulation*, *ice-cored moraine* and *permanent snow patches*.

#### Periglacial Process Domain

Periglacial processes are related to frost processes and are related to permafrost distribution. In this process domain *periglacial slopes*, *active rock glaciers*, *less active rock glaciers* and *periglacial deposits* were mapped.

#### Gravitational Process Domain

Gravitational processes are the result of gravitational attraction. In this process domain

*gravitative accumulation area, rock slide, vegetation covered talus slope* and *landslides* were mapped.

### **Fluvial Process Domain**

In the fluvial process domain, areas mainly shaped by the influence of liquid water are mapped such as: *fluvial deposit area, fluvio-glacial deposits* and *lakes*.

#### **4.2.2 Geodatabase Design**

Geomorphological mapping is based on the geomorphological mapping legend of the University of Lausanne (cf. Lambiel et al. (2013)). The legend is a morphogenetic mapping system, built on the following principles:

- The colours represent process categories
- The signatures have a genetic significance and are in the colour of the related process
- The morphodynamic differentiation of erosion and accumulation area is achieved by white and coloured surface respectively
- The morphography, slope gradient and the lithology are not represented.

The ArcGIS version of the geomorphological mapping legend consists of a geodatabase, containing three feature classes "points", "lines" and "surfaces" (Lambiel et al., 2013). Geomorphological symbolisation was predefined, but was manually adapted for some classes. This legend was chosen, because it is best suitable in high and middle mountain regions (Lambiel et al., 2013) and, the geodatabase architecture as well as the symbolisation could be adopted.

#### **4.2.3 Geomorphological Mapping**

Geomorphological mapping was mainly based on remote sensing and to a minor extent also on on-site photography. A SPOT-5 panchromatic satellite imagery and a SRTM DEM was used. Additionally, GoogleEarth and on-site photography, taken during the field campaign (13-18 September 2014), were used.

The geomorphological mapping was done in ArcGIS. A copy of the geodatabase of the University of Lausanne was created. Geomorphological features ("polygons", "lines" or "points") were then created and stored in the geodatabase. All created features in the geodatabase were defined by the following attributes:

- OBJECTID Unique value of every object
- SHAPE Defines if the object is a "polygon", "line" or "point" feature
- SHAPE\_LENGTH Length of object (in m)
- SHAPE\_AREA Area of object (in  $m^2$ )
- RuleID Defines the geomorphological class of the object

All created features in the geodatabase were projected to the WGS\_1984\_UTM\_Zone\_44N. In order to have a consistent and logic database, the following topology rules, based on Demel and Hauenstein (2005), were applied:

- Polygons must not have gaps
- Polygons must not overlap
- Points must be disjoint
- Lines may overlap lines or polygons
- Points may overlap lines or polygons

The map visualisation was mainly done, based on the predefined symbology of the geo-database and was manually adapted (see figure 10).

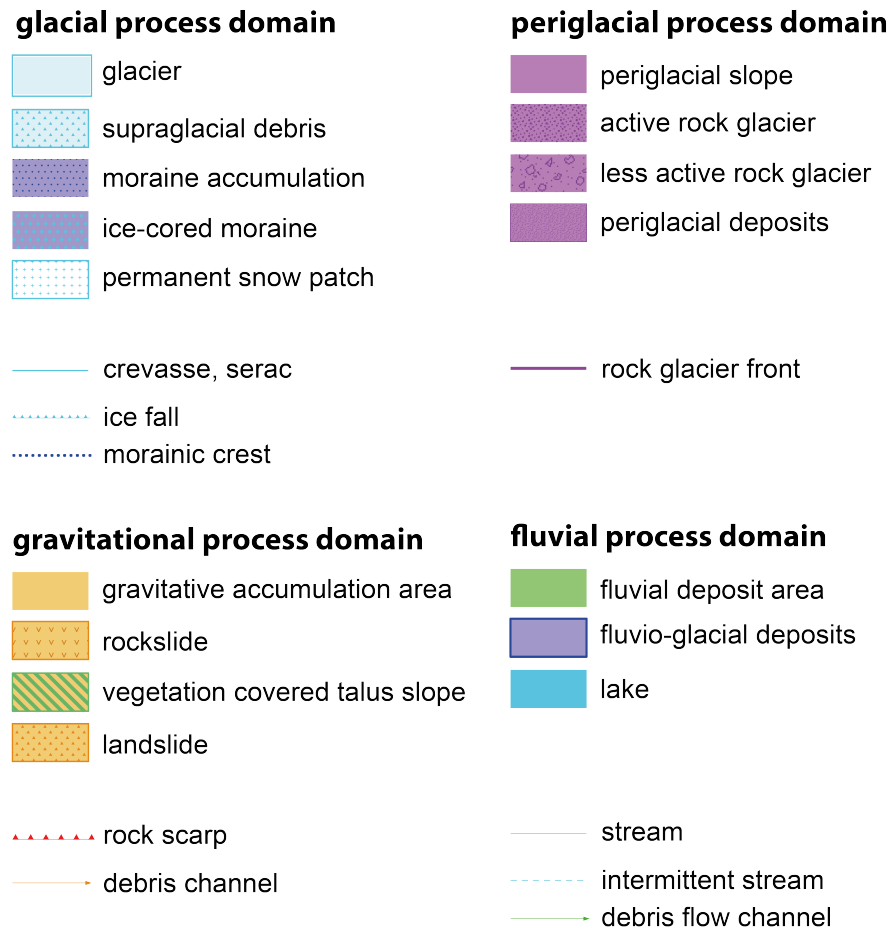


Figure 10: Visualisation of the geomorphological legend

### 4.3 Ground Penetrating Radar

In order to investigate the internal characteristics of a glacier-ice-debris complex (see section 1.3) geophysical methods have to be applied.

Most common geophysical methods in periglacial environments are electrical methods, electromagnetic methods, refraction seismics and GPR (Burger et al., 2006; Hauck and Kneisel, 2008). When conducting geophysical studies, it is recommended to combine at least two geophysical methods, to validate the results (Burger et al., 2006; Hauck and Kneisel, 2008). Due to the limited time, and logistical reasons a single device was used. Considering the potential weakness of a single method investigation, we decided to use GPR.

In different studies combining geophysical methods, GPR turned out to be most suitable for the determination of internal structures of talus deposits (Otto and Sass, 2006; Sass, 2006) as well as the delineation of internal boundaries of massive ice (Schrott and Sass, 2008). Successful GPR studies were conducted on permafrost soils (e.g. Arcone (2002); Moorman et al. (2003), talus slopes (e.g. Otto and Sass (2006); Sass (2006) and rock glaciers (e.g. Berthling et al. (2000); Hausmann et al. (2012); Isaksen et al. (2000); Krainer et al. (2012); Monnier et al. (2013).

Therefore, GPR is the most suitable and effective method to investigate the internal structures of a glacier-ice-debris complex.

#### 4.3.1 Background and Physical Principles

GPR or Radio Echo Sounding (RES) is a geophysical method for non destructive subsurface investigations. GPR is based on the transmission and detection of electromagnetic radiation of frequencies between 10MHz and 5GHz (Daniels, 2004).

Electromagnetic impulses are sent into ground and reflected at subsurface boundaries of materials with different electromagnetic properties. Electromagnetic waves will therefore be reflected back to the receiver antenna. The amplitude of the received reflections can be plotted as a function of time. When plotting a series of reflections, a profile of underground reflections develops (Takahashi et al., 2007).

Thus, GPR basically detects changes in the electromagnetic wave propagation, which is determined by the electric permittivity ( $\epsilon$ ), the electric conductivity ( $\sigma$ ), and the magnetic permeability ( $\mu$ ). In GPR use, the magnetic permeability is normally of little importance and will therefore not be described (Berthling and Melvold, 2008).

Electric permittivity describes the resistance of a medium when setting an electric field

in it. Electric permittivity mainly determines the velocity of propagation of a material, which depends mostly on its water content. Electric permittivity is normally expressed relative ( $\epsilon_r$ ) to permittivity in free space ( $\epsilon_0$ ) ( $8.854 \times 10^{-12}$  F/m) (see equation 2) (Daniels, 1996). The relative permittivity normally has values between 3 (ice) and 80 (pure water) (Hubbard and Glasser, 2005).

$$\epsilon_r = \frac{\epsilon}{\epsilon_0} \quad (2)$$

Electric conductivity  $\sigma$  (S/m) describes the ability of a material to conduct electric current. Electric conductivity is principally controlled by the amount of dissolved salts in water. The bigger the impurity of a medium, the higher the electric conductivity (Hubbard and Glasser, 2005; Berthling and Melvold, 2008).

There are three important parameters when working with GPR:

- Radar wave velocity
- Radar wave power loss
- Radar wave resolution

They all depend on the electrical properties of the underground material (Davis and Annan, 1989).

### **Radar Wave Velocity**

For electric conductivities lower than 100mS/m, which is the case for the materials in the study area, the propagation velocity remains constant at frequencies between 10 and 1000MHz (Davis and Annan, 1989). Therefore in this study, the velocity of propagation  $v$  is mainly depending on the relative permittivity  $\epsilon_r$  and can be described as follows:

$$v = \frac{c_0}{\sqrt{\epsilon_r}} \quad (3)$$

where  $c_0$  (299'792'458 m/s) is the speed of light in free space.

For granite, with a relative electric permittivity of 4-6, a velocity of wave propagation of about 0.13m/ns results. If the propagation velocity is known, absolute measurements of depth can be done.

### Radar Wave Power Loss

The second parameter on which wave propagation is depending on, is radar wave power loss. Most of the power loss is occurring as material attenuation loss, spreading loss and scattering loss (Daniels, 2004). The attenuation loss of a material is given by:

$$L_a = 8.686 \times 2 \times R \times 2\pi f \sqrt{\left(\frac{\mu_0 \mu_r \epsilon_0 \epsilon_r}{2} (\sqrt{(1 + \tan^2 \delta)}) - 1\right)} \quad (4)$$

where:

- f = Frequency in Hz
- $\tan \delta$  = Loss tangent of material
- $\mu_r$  = Relative magnetic susceptibility of material
- $\mu_0$  = Absolute magnetic susceptibility of free space

The attenuation therefore increases with electric permittivity, electric conductivity and radar frequency. As a consequence, the penetration depth decreases with higher frequencies (Hubbard and Glasser, 2005).

Another factor creating loss is the geometrical spreading, which occurs when transmitting radar signals from the antenna. It is conventionally related to the inverse fourth power of distance for a point reflector (Daniels, 2004; Davis and Annan, 1989).

Table 3: Typical relative electrical permittivity, electrical conductivity, velocity and attenuation in common earth surface at 100MHz (based on Davis and Annan (1989))

Material	$\epsilon_r$	$\sigma$ (mS/m)	v (m/ns)	$\alpha$ (dB/m)
Air	1	0	0.3	0
Distilled water	80	0.01	0.033	0.002
Fresh water	80	0.5	0.033	0.1
Salt water	80	0.5	0.033	1000
Dry sand	3-5	0.01	0.15	0.01
Saturated sand	20-30	0.1-1	0.06	0.03-0.3
Limestone	4-8	0.5-2	0.12	0.4-1
Shales	5-15	1-100	0.09	1-100
Silts	5-30	1-100	0.07	1-100
Clays	5-40	2-1000	0.06	1-300
Granite	4-6	0.01-1	0.13	0.01-1
Dry salt	5-6	0.01-1	0.13	0.01-1
Ice	3-4	0.01	0.16	0.01

The third factor adding loss is, scattering. Scattering includes energy loss processes such as reflection, refraction and diffraction (Hubbard and Glasser, 2005). Scatter loss are all unwanted and unrelated signals, with the same spectral characteristics as the target wavelets and occurring in the same time window (Daniels, 1996).

Further wave losses are caused by absorption due to conduction or relaxation (Hubbard and Glasser, 2005). In table 3 typical electromagnetic properties are listed for the most common materials.

### Radar Wave Resolution

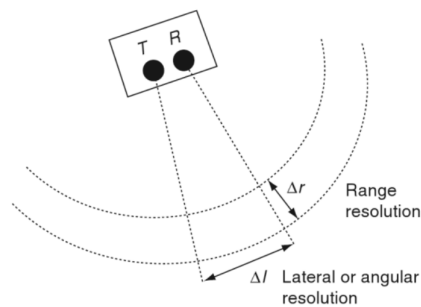


Figure 11: Vertical and lateral resolution; figure source: (Jol, 2009)

Resolution is understood as the limit of certainty in determining the position and geometrical aspects (e.g. size, shape, thickness) of a target (Jol, 2009). GPR resolution has two main aspects: vertical (range or depth) resolution and lateral (angular) resolution (see figure 11).

Two reflected pulses can be detected individually, when they are not overlapping. The widely accepted opinion is that two pulses are distinguishable if separated by half their "half width" (Jol, 2009). When separated closer together, two pulses will likely be detected as a single event. Therefore the radial resolution is as follows:

$$\Delta r = \frac{Wv}{4} \quad (5)$$

The radial resolution length is independent of distance from source, and depending on the pulse width and propagation velocity.

Lateral resolution is depending on the distance from source and therefore defined as follows (Jol, 2009):

$$\Delta l = \sqrt{\frac{vrW}{2}} \quad (6)$$

where:

- v = Velocity of propagation
- r = Distance to target
- W = Width of amplitude

#### 4.3.2 Devices

The GPR survey was done using two different devices: Malå ProEx and VIRL-6.

##### Malå ProEx

Malå ProEx is a modular full-range GPR device developed by Malå Geoscience in Sweden. Malå ProEx consists of a control unit, a monitor and an antenna. The control unit is the core device for synchronizing the radar impulses, stacking and storing of the radar traces. Trace coordinates are stored with an external GPS device, which is connected to an USB-port (see figure 12).

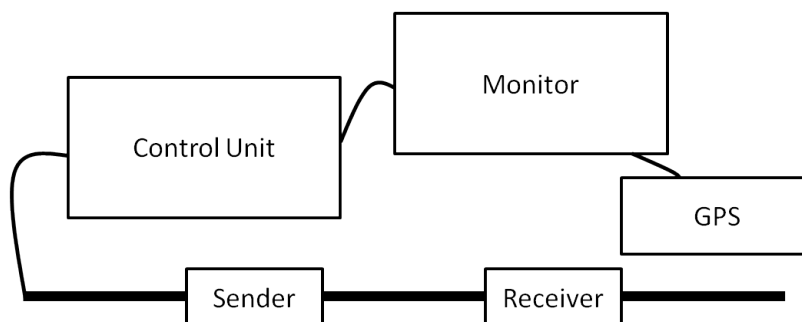


Figure 12: System design of Malå ProEx (own figure)

An unshielded 25MHz Rough Terrain Antenna (RTA) was used. RTA is a robust GPR antenna, containing sender and receiver, in one snake-like protection hose. The antenna has a total length of 13m. The sender-receiver distance is 6.2m. The penetration depth

is technically limited to 300m. Based on equation 5 an electromagnetic pulse with a frequency of 25MHz, has a wavelength of 5.2m. A vertical resolution of about 1.3m can be calculated. The horizontal resolution is as described depending on the distance from the source.

### VIRL-6

The second GPR device is a self-construction radar built by Vasilenko et al. (2011). VIRL-6 is a compact lightweight impulse radar, designed for glaciological applications (Vasilenko et al., 2011). The radar is built up of two main parts: a transmitter (TX) and a receiver (RX) linked with a synchronization system. The central device is a Control and Recording Unit (CRU). The CRU performs the synchronization of pulse generation, stacking of signal and data storage (Vasilenko et al., 2011), (see figure 13). The coordinates are stored with a connected GPS device.

A 20MHz antenna was used. The antenna has a length of 12m (6m transmitting and 6m receiving antenna). The penetration depth is up to 600m. The vertical resolution in a material with an electromagnetic velocity of 0.13m/ns is according to equation 5 about 1.6m.

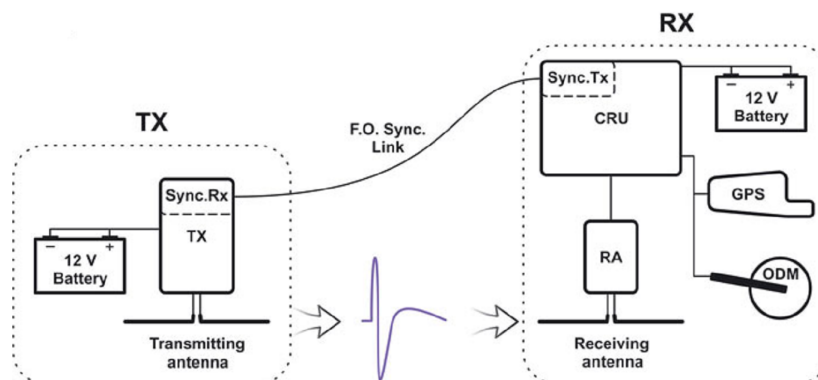


Figure 13: System design of VIRL-6; figure source: (Vasilenko et al., 2011)

### 4.3.3 Data Acquisition

There are three established antenna set-ups when using GPR for profiling: Common mid-point (CMP), common offset (CO) and wide-angle reflection and refraction (WARR). The little used WARR set-up keeps one antenna fixed (transmitter or receiver) and moves the other antenna away. WARR only works well with horizontal plan reflectors (Hubbard and Glasser, 2005). In the more used CMP set-up, the transmitter and receiver are altered

apart at a constant interval (Berthling and Melvold, 2008).

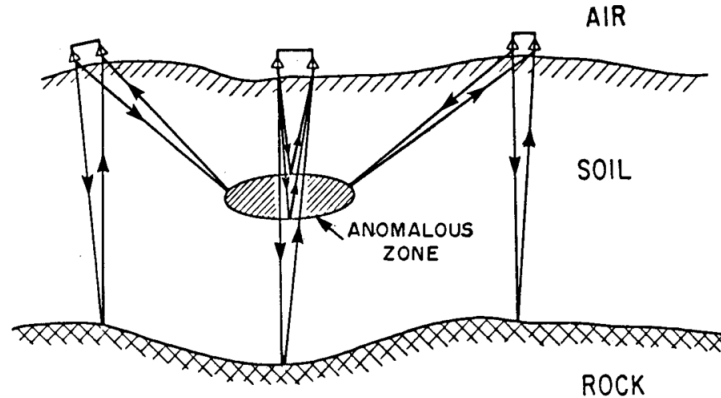


Figure 14: Common offset mode; figure source: (Davis and Annan, 1989)

CMP set-up is mostly used to obtain information about propagation of radar waves of the investigated underground.

In this study, the GPR survey was done using CO mode. CO is the most commonly used antenna set-up. In CO mode, the transmitter and the receiver are separated at a constant distance and moved together along the profile. Both, buried obstacles and internal horizons can be detected using this mode (see figure 14).

An appropriate antenna spacing is necessary. Too close antennas will likely mask reflections from the upper part, whereas too large spacing will decrease the penetration depth (Berthling and Melvold, 2008). The antenna spacing used in this study was 6.2m (Malå ProEx) and 5.8m (VIRL-6).

The second parameter which has to be chosen is the time interval between the measurements. The antenna can either be moved continuously or stepwise. The step-mode has the advantage of a better ground coupling but will need more time. In this study, the measurements were taken continuously every 0.5s (Malå ProEx) and every 0.2s (VIRL-6) respectively.

Within three days (14-16 September, 2014), a total of 44 GPR profiles were taken. 12 profiles were taken using Malå ProEx (red line) and 32 profiles were taken using VIRL-6 (black line)(see figure 15. The total length of all profiles is 21.5km. All parts of the glacier-ice-debris complex were covered, apart from the orographic right lateral moraine, as well as the upper rock glacier-like tongue.

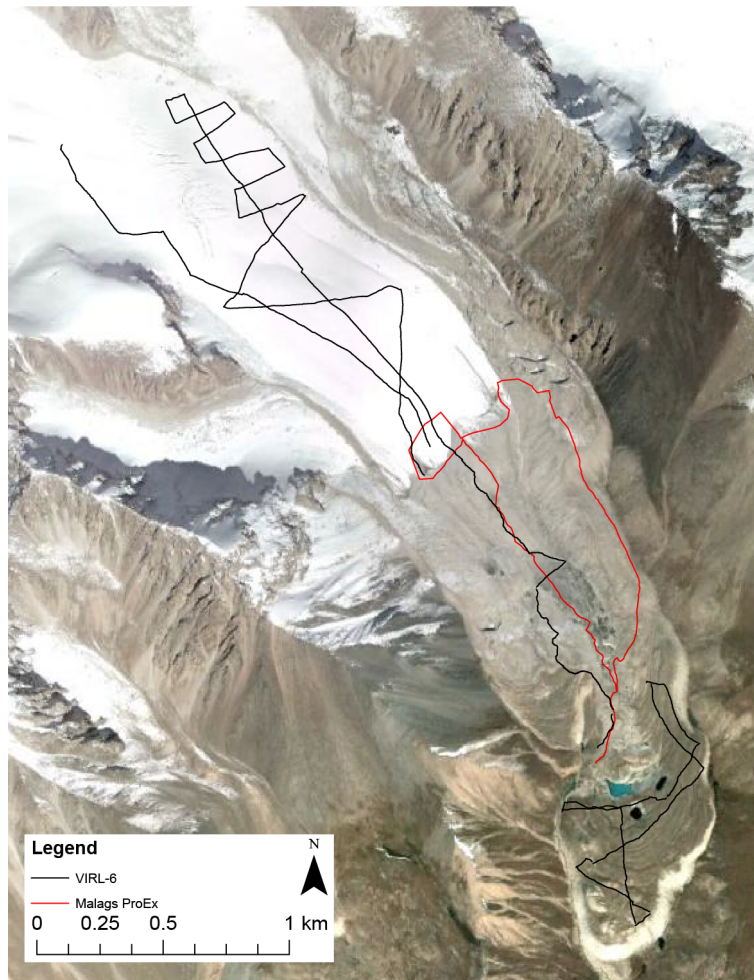


Figure 15: GPR profiles taken on the glacier and the ice-debris complex (figure based on a GoogleEarth scene)

#### 4.3.4 Data Processing

The main objective of data processing in GPR is to improve the radar signals. GPR raw data needs to be improved before interpretation can be done. The processing contains techniques to enhance reflections and reduce noise or to represent geometry of reflections more correctly (Berthling and Melvold, 2008). With existing processing software, an unlimited data manipulation is possible. However, the cost-benefit ratio has to be kept in mind. In this study all data processing was done using ReflexW 7.2.3 software by K.J. Sandmeier. All data processing was done after the data acquisition in order not to lose important information. In the following section, all processing steps applied will be described and discussed.

### Static Correction

In a first step, the proper alignment of the surface was corrected. Due to the rough terrain, the GPR antenna was carried above ground and not directly on the ground. Thus, radar waves first travel through air, before hitting the ground. Therefore, the first radar signal identified, is the arrival of the so-called air wave, reflected at the surface. The main interest however are travel times into the ground, measured from surface. So radar traces are shifted physically upwards (back in time), to get a proper alignment of zero time to the surface (Neal, 2004). In figure 16 traces will be shifted upwards, until the first break appears at the time zero. the correct alignment of the first break is important, when converting travel times into absolute depth values. The static correction was done manually for all profiles.

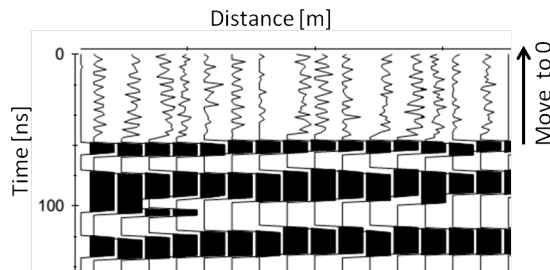


Figure 16: Static correction of the first break in radar traces (own figure)

### Signal Saturation Correction

The main aim of the signal saturation correction is to reduce noise and to improve the signal-to-noise ratio. The signal saturation correction is often achieved applying frequency filters. Frequency filters remove or reduce stipulated frequency ranges (Hubbard and Glasser, 2005). High-frequency and low-frequency noise can be removed. Low-frequency noise can occur due to the proximity of transmitter and receiver. Electrostatic and inductive fields close to the transmitter can cause low-frequency noise. (Jol, 2009). This so-called wow noise can push traces to the sides forming bow shapes. Wow noise can be suppressed using a high-pass filter (Neal, 2004). In ReflexW the *subtract-mean (dewow)* filter was applied. *Subtract-mean (dewow)* calculates a running mean value for every value of each trace. The running mean will then be subtracted from the central point (Sandmeier, 2014).

To remove high-frequency and low-frequency noise, another filter had to be applied. Appropriate frequency filters are best determined by trial-and-error (Hubbard and Glasser, 2005). Hence, the *bandpassbutterworth* filter was determined. *Bandpassbutterworth* re-

tains a frequency range defined by a low-cut and a high-cut frequency (Sandmeier, 2014). Frequencies outside defined boundaries will be set to zero. Noise can be suppressed using this filter when differing from the signal in its frequency content. (Sandmeier, 2014). Although the *subtract-mean (dewow)* filter was applied, the *bandpassbutterworth* filter is useful, because only low-frequencies outside defined range are set to zero, whereas the *subtract-mean (dewow)* affects the whole range.

### Signal Amplification

As described in section 4.3.1, the radar signal quickly attenuates with depth. Profound reflections are hardly visible. For the profile interpretation, a more equalized signal is needed. Therefore, signal amplification aims to compensate the rapid signal power loss. When applying a time-dependent gain function, the amplitudes can be equalized and a more balanced profile results (Jol, 2009).

In ReflexW, the time-dependent *gain function* was applied. The *gain function* consists of a linear and an exponential part:

$$g(t) = (1+a \times t) \times e^{(b \times t)} \quad (7)$$

where:

$$a = \frac{a'}{\text{pulsewidth}}$$

$$b = \frac{b' \times v}{8.69} \text{ with } v = 0.1 \text{m/ns}$$

The pulse width is automatically taken from the nominal frequency or automatically determined from the first arrival (Sandmeier, 2014). Two filter parameters  $a'$  (linear) and  $b'$  (exponential) must be entered manually. Parameters depend on the specific data and ground material. In this study, the linear parameter was set to 0.8 and the exponential parameter was set 0.

Another filter used, was the automatic gain control (AGC). AGC is a continuously adaptive gain function. AGC computes an average signal over a time window for every data trace. The data point in the centre of the window is amplified by the ratio of the desired output value to the average signal amplitude (Annan, 1999b; Berthling and Melvold, 2008). AGC is suitable where the continuity of stratigraphic horizons is of interest (Annan, 1999b). When applying gain functions it has to be kept in mind, that ambient and systematic noise can be amplified as well. Effects of the *gain function* and AGC (window

length = 2.5ns) are apparent in figure 17.

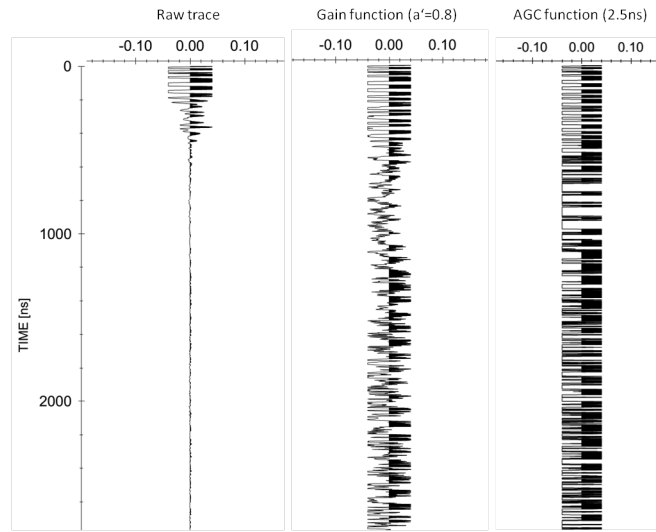


Figure 17: Effects of different gain functions on a single radar trace: raw trace (left), gain function (middle) and AGC function (right))(own figure)

### Migration

Electromagnetic waves propagate conically into the ground, with increasing radius with depth (Berthling and Melvold, 2008). Point reflectors and steeply inclined reflectors are therefore systematically distorted, as detected reflections can origin anywhere on the wave front (Berthling and Melvold, 2008). GPR reflections only give proper information about depth, when measured perpendicular to the surface, at the zero-offset position. As a consequence, point reflectors will be represented as upward-directed hyperbolas (Hubbard and Glasser, 2005).

Migration is the process of correcting geometrical irregularities such as dipping slopes, planar reflectors and hyperbolas (Hubbard and Glasser, 2005). Migration attempts to correctly position subsurface layers (Neal, 2004). Migration is a very important processing step and requires knowledge of the velocity structure (Berthling and Melvold, 2008).

In ReflexW *fk migration* (Stolt) was applied. *Fk migration* (Stolt) is based on a two-dimensional Fourier transform over time and space (Stolt, 1978). The method works in the frequency-wavenumber (fk) range (Sandmeier, 2014). The transformation is based on a constant ground velocity, which was 0.13m/ns in this study.

### Further Filtering

A vast variety of filters exists to improve the data. Another filter applied on GPR profiles

was *background removal*. *Background removal* subtracts an averaged trace from all traces. The averaged trace is built up from the chosen time/distance range of the current session (Sandmeier, 2014). Thus horizontal clutter can be removed. It has to be kept in mind, that real reflections could be removed as well.

Some of the profiles taken by VIRL-6 at the rock glacier tongue, show a heavy distortion between 500 and 700ns. In order to minimize the disturbing signal, a *multiplication* filter was applied between 500 and 700ns. The multiplication factor was 0.32. It has to be noted that reflections hidden by the distortion signal, can only partly be recovered.

### Topographic Correction

The last processing step done, was the topographic correction of the radar profiles. In ReflexW, *correct 3D-topography* filter was applied. *Correct 3D-topography* performs a time-independent correction for each trace in time direction, based on z-coordinates (Sandmeier, 2014). Coordinates need to be stored for every single trace.

During data acquisition, the GPS device of Malå ProEx was not working properly. Therefore the coordinates were taken from a hand held GPS and manually interpolated. A linear interpolation was done, resulting in a bit angular surface of some GPR profiles.

### 4.3.5 Subsurface Velocity Estimation

Normally in GPR profiles, the depth axis is the two-way traveltime (TWT) (Berthling and Melvold, 2008). A depth conversion of the TWT requires knowledge of the subsurface velocities.

In this thesis the specification of the depth axis was based on an assumption of the electromagnetic properties of the subsurface. All profiles, except the profiles on the glacier, were plotted with a subsurface velocity of 0.13m/ns. The assumption of the subsurface velocity was based on other GPR studies on rock glaciers or moraines (e.g. Farbrot et al. (2005); Sass (2006); Odell et al. (2009)). Since the electromagnetic properties of the subsurface are not known, the depth specifications show some uncertainties (see table 4). A variance of  $\pm 0.02$ ns leads to an uncertainty of  $\pm 2$ m in 10m depth,  $\pm 8$ m in 50m depth and  $\pm 15$ m in 100m depth.

Table 4: Uncertainty at the time to depth conversion

Subsurface velocity	Depth at $t=77\text{ns}$	Depth at $t=384\text{ns}$	Depth at $t=769\text{ns}$
0.11ns	8m	42m	85m
0.12ns	9m	46m	92m
<b>0.13ns</b>	<b>10m</b>	<b>50m</b>	<b>100m</b>
0.14ns	11m	54m	108m
0.15ns	12m	58m	115m

A more precise method to determine the subsurface velocity are on-site measurements. An average subsurface velocity is best obtained by CMP measurements (see section 4.3.3). Other possibilities to find out the subsurface velocity are through ground truthing or hyperbolic fitting (Jol, 2009). Due to technical limitations, no CMP measurements could be conducted. Therefore the velocity estimation is based on hyperbola fitting. The subsurface velocity can be estimated, by fitting a synthetic curve to a hyperbolic reflection. A hyperbola is the result of a point reflector in an unmigrated GPR profile.

In figure 18  $x_0$  is the position of a point reflector.  $t_0$  is the corresponding TWT.  $t_n$  is the TWT in position  $x_n$ .  $v$  is the velocity of the electromagnetic wave.

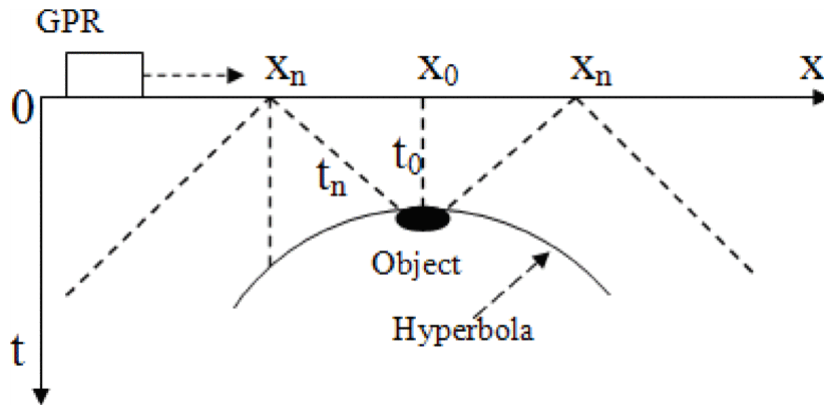


Figure 18: Hyperbola fitting (figure source: (Liu et al., 2010))

The following hyperbola equation (based on (Chen et al., 2004) results:

$$\frac{t_n^2}{t_0^2} - \frac{4(x_n - x_0)^2}{(vt_0)^2} = 1 \tag{8}$$

Hence the subsurface velocity can be estimated. However, the method is technically limited. Curve fitting only works, when hyperbolas are present in profiles. Furthermore, it has to be assumed, that sender and receiver of a GPR device are in the same position. Only the average velocity can be estimated. Hence a homogeneous subsurface has to be expected. Hyperbola fitting tends to produce approximate velocities with an error of  $\pm 10\%$  (Jol, 2009). This method was used in several GPR studies investigating rock glaciers (e.g. Florentine et al. (2014); Fukui et al. (2008); Monnier et al. (2013)). It was thus applied in this study as well.



## 5 Results

### 5.1 Rock Glacier Inventory

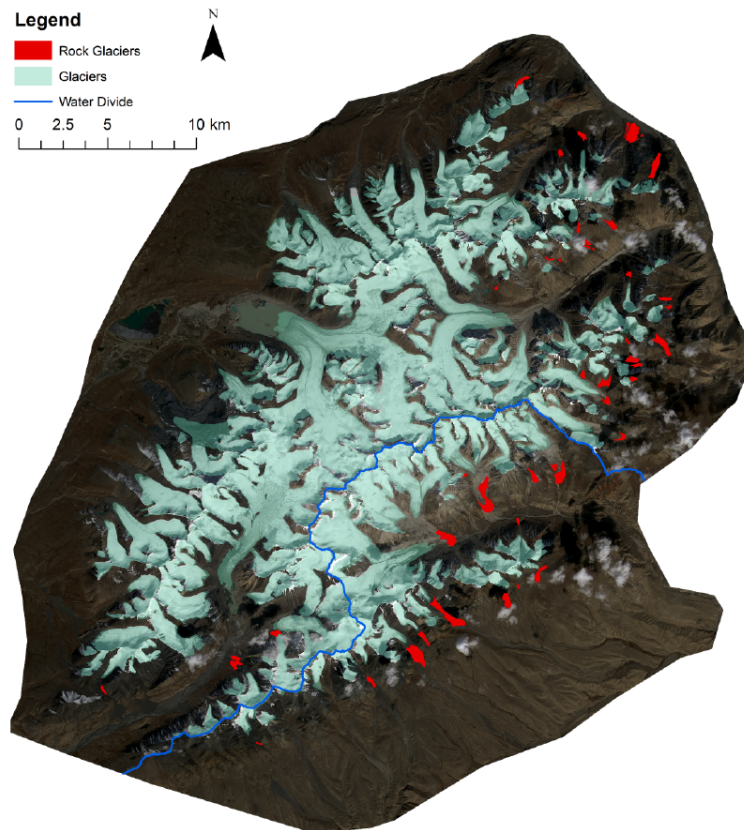


Figure 19: The rock glacier inventory

Figure 19 shows the mapped rock glaciers in red and the glaciers in blue. The blue line indicates the water divide. The southern part is draining into the Aksu-Tarim catchment, the northern part is draining into the Naryn-Syr Darya catchment. A larger version of this figure is found in Appendix A.1.

#### 5.1.1 Key Characteristics of Rock Glaciers

A total of 63 rock glaciers, covering an area of  $8.8\text{km}^2$  were identified and mapped (see figure 19). Rock glaciers are most prominent on the southern and eastern side of the Ak-Shiirak massif and on south facing slopes in the inner valleys. The glacierized area consists of 178 glaciers covering an area of  $360\text{km}^2$ . The glacierized area covers about 27%

and rock glaciers cover about 0.7% of the total study area. Rock glaciers cover about 2.4% of the glacierized area (see table 5).

Table 5: Comparison of glacier and rock glacier area

	Area [km <sup>2</sup> ]	%	%
Study area	1319	100	
Glacierized area	360	27.3	100
Rock glacier area	8.8	0.7	2.4

The mean altitude at the rock glacier front in the Ak-Shiirak massif is at about 3880m a.s.l. The mean altitude at the rock glacier front is lowest in the northern part of the Ak-Shiirak massif at rock glaciers in north facing direction. The lower minimum altitude in these rock glaciers could be due to the lower direct solar radiation in north facing slopes, or due to inactivity of rock glacier features. The minimum altitude at the rock glacier front can be a good approximation for the lower permafrost boundary. Gorbunov (1996) stated continuous permafrost in the Central Tien Shan ranges to occur above 3600m a.s.l. Due to global warming, the lower boundary of continuous permafrost will likely be even higher.

The mean maximum altitude of rock glaciers is at about 4000m a.s.l. and is often delimited by adjacent glaciers or recently deglaciated glacier forefield. The mean elevation range of altitude is 139m. Rock glaciers have a mean length of 656m and a mean width of 295m. Rock glacier cover a mean area of about 140000m<sup>2</sup>. The mean slope is 12.2°(see table 6).

Table 6: Key characteristics of rock glaciers

Key characteristics	Mean	Median	Minimum	Maximum
Minimum altitude at the front [m]	3883	3920	3073	4339
Maximum altitude of rock glacier [m]	4022	4034	3160	4398
Elevation range of altitude [m]	139	109	29	480
Length [m]	656	550	153	2380
Width [m]	295	256	83	699
Area [km <sup>2</sup> ]	0.14	0.09	0.01	0.74
Slope[°]	12.2	11.6	5.3	21.8

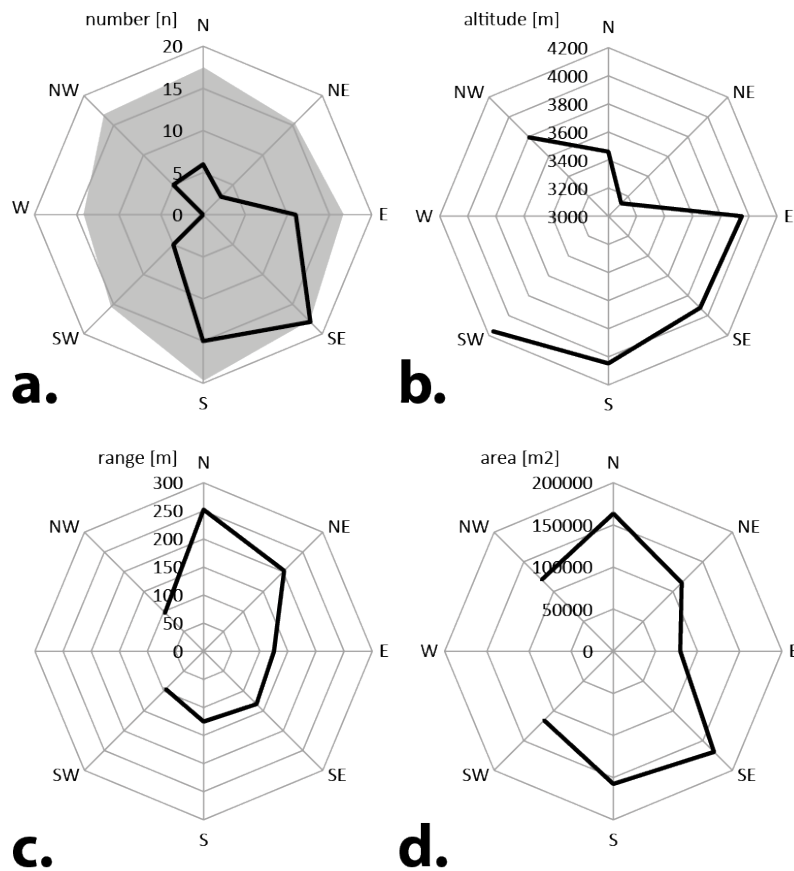


Figure 20: Key characteristics of the inventoried rock glaciers: a. Mean slope aspect of rock glaciers and in grey the aspect distribution of the relief; b. mean lower minimal altitude; c. mean range; d. mean area

Rock glaciers are most prominent on south-eastern slopes (see figure 20a). About 70% (n=44) of the inventoried rock glaciers occur on eastern, south-eastern or southern slopes. The grey bar in figure 20a indicates the aspect distribution of the relief. The south-western to north-eastern orientation of the mountain range is recognisable, with slightly more dominant southern and northern slopes.

The mean lower minimum altitude of the mapped rock glaciers is highest in south facing (E, SE, S, SW) slopes and lower in north facing slopes (NW, N, NE) (see figure 20b). The height difference is most likely caused by the stronger direct solar radiation on south facing slopes. The mean elevation range of altitude shows a similar north-south trend. The mean elevation range of altitude is higher on north facing slopes than on south facing slopes (see figure 20c). Rock glacier expanse is biggest on southern, south-eastern and northern slopes, but does not show a clear trend (see figure 20d).

### 5.1.2 Ice Content

A total glacier ice volume of  $21.7\text{km}^3$  was calculated. The total volume of the ice-rich permafrost in rock glaciers was estimated to be  $0.329\text{km}^3$ . The ice-rich permafrost was assumed to have a volumetric ice content of 50%. Thus, a total ice volume of  $0.165\text{km}^3$  was calculated (see table 7).

Table 7: Ice content of glaciers and rock glaciers

Parameter	Value
Glacier ice volume	$21.7\text{km}^3$
Volume of ice-rich permafrost in rock glaciers	$0.329\text{km}^3$
Rock glacier ice volume (50%)	$0.165\text{km}^3$

### 5.1.3 Rock Glacier to Glacier Ratio

The rock glacier to glacier ratio helps to estimate the hydrological relevance of rock glaciers. The rock glacier to glacier ratio was calculated for the Aksu and the Naryn catchment (see figure 19), within the study area, as well as for the whole study area. The Aksu catchment covers most of the southern part of the Ak-Shiirak massif as well as the inner valley, where the area of detailed investigation is situated. The part draining in to the Aksu-Tarim catchment holds a glacier ice volume of more than  $3\text{km}^3$ . The estimated rock glacier ice volume is  $0.09\text{km}^3$ , resulting in a rock glacier to glacier ratio of 1:34 (see table 8). In the part draining in to the Naryn-Syr Darya catchment, the glacier ice volume is  $0.68\text{km}^3$ . The rock glacier ice volume is about  $0.07\text{km}^3$ . The resulting rock glacier to glacier ice volume ratio is 1:9. For the whole study region, a ratio of 1:23 is therefore resulting.

Table 8: Ratio of rock glacier to glacier ice volume

Area	Rock glacier ice volume	Glacier ice volume	Rock glacier to glacier ice volume ratio
Aksu	$0.09\text{km}^3$	$3.07\text{km}^3$	1:34
Naryn	$0.07\text{km}^3$	$0.68\text{km}^3$	1:9
<b>Ak-Shiirak</b>	<b><math>0.165\text{km}^3</math></b>	<b><math>3.75\text{km}^3</math></b>	<b>1:23</b>

## 5.2 Geomorphological Map

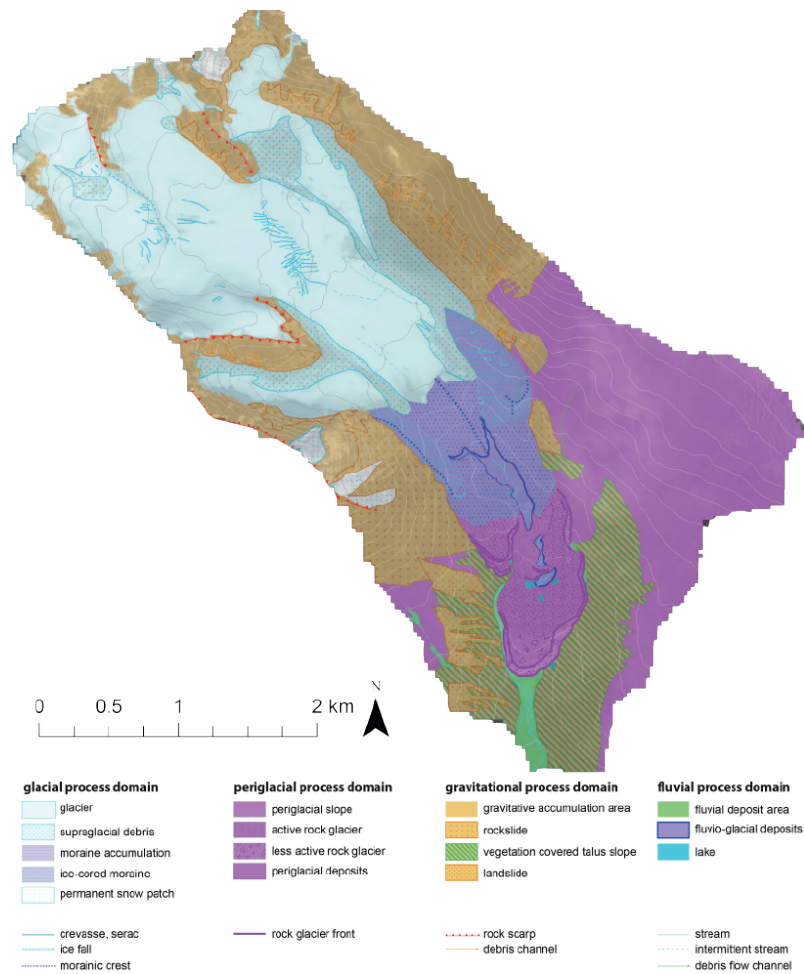


Figure 21: The geomorphological map

Figure 21 shows the geomorphological map. A larger version of the geomorphological map is found in appendix A.2.

### 5.2.1 Surface Area of Process Domains

A total area of 13.9km<sup>2</sup> was mapped. Of the total mapped area 40.6% were mapped as glacial process domain, 25.6% as periglacial process domain, 31.9% as gravitational process domain and 1.9% as fluvial process domain (see table 9). About 26% of the area were mapped as glaciers, 21% as periglacial slope and 12.4% as gravitative accumulation area.

Table 9: Distribution of the surface area of the geomorphological process domains

<b>Glacial process domain</b>	<b>Area [<math>km^2</math>]</b>	<b>%</b>
Glacier	3.6	25.9
Supraglacial debris	0.9	6.6
Moraine accumulation	0.5	3.8
Ice-cored moraine	0.4	2.9
Permanent snow patch	0.2	1.4
	<b>5.66</b>	<b>40.6</b>
<b>Periglacial process domain</b>	<b>Area [<math>km^2</math>]</b>	<b>%</b>
Periglacial slope	2.9	21.0
Active rock glacier	0.4	3.1
Less active rock glacier	0.1	0.8
Periglacial deposits	0.1	0.7
	<b>3.57</b>	<b>25.6</b>
<b>Gravitational process domain</b>	<b>Area [<math>km^2</math>]</b>	<b>%</b>
Gravitative accumulation area	1.7	12.4
Rockslide	1.3	9.6
Vegetation covered talus slope	1.1	8.4
Landslide	0.2	1.6
	<b>4.45</b>	<b>31.9</b>
<b>Fluvial process domain</b>	<b>Area [<math>km^2</math>]</b>	<b>%</b>
Fluvial deposit area	0.1	1.0
Fluvio-glacial deposits	0.1	0.8
Lake	0.009	0.1
	<b>0.26</b>	<b>1.9</b>
<b>Total</b>	<b>13.94</b>	<b>100.0</b>

### 5.2.2 Geomorphological Genesis of the Ice-Debris Complex

The origin of the investigated ice-debris complex can generally be separated in three different parts (see black delimitation in figure 22). The three parts describe distinct landform sequences with different origins. In the lower part, the different landform sequences meet and form a complex ice-debris tongue.

In the eastern and in the western part, small cirque glaciers, surrounded by steep rock walls are the initial points of the ice-debris complex formation. Rock wall erosion due to frost weathering lead to supraglacial deposition of debris. Another distinct indicator for supraglacial debris deposition is a large debris deposition on the north eastern cirque glacier, likely resulting from a bigger rock slide.

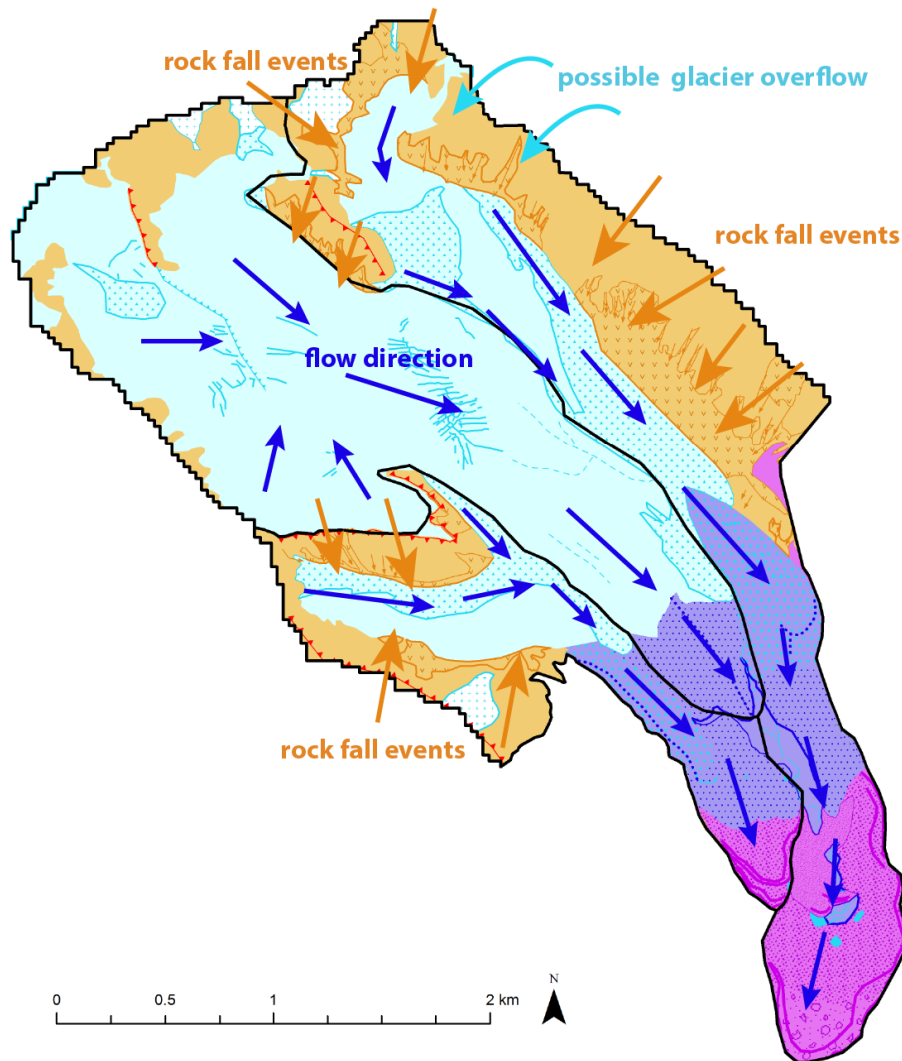


Figure 22: Geomorphological Genesis of the Ice-Debris Complex

The glacier with supraglacial debris is flowing downvalley, where steep rock walls lead to further debris input. Snowfall or avalanches on the steep slopes could have led to a snow and ice deposition on the ice-debris complex. In the eastern part, an overflow of the adjacent glacier with irregular ice avalanches was likely in former times, leading to enhanced ice input. Steady ice and debris input lead to an ice-debris mixture. With a higher debris proportion, the ice-debris complex starts to behave more like a rock glacier and less like a normal glacier. The geomorphological sequence of the lateral landform parts at the eastern and the western margin are the same: *glacier - supraglacial debris - ice-cored moraine - moraine accumulation - active rock glacier - (less active rock glacier)*. Therefore, the both lateral parts show a typical landform transition.

The third part, affecting the genesis of the ice-debris complex, is the main glacier in the center of the ice-debris complex (see figure 22). The geomorphological sequence is less complex: *glacier - moraine accumulation*. The glacier shows almost no supraglacial debris, as there are not enough steep rock walls at the glacier margin. At the glacier tongue, a medial moraine originates as the consequence of the glacier. The medial moraine has likely originated as a result of glacier downwasting and the deposition of englacial debris.

### 5.3 Ground Penetrating Radar

GPR measurements were recorded in a tributary valley of the Coendy valley (see figure 2). A glacier with adjacent ice-debris complex was investigated. The investigated ice-debris complex has a length of about 2.3km and a maximum width of 770m. The elevation range of the ice-debris complex is 300m, the glacier tongue is situated on about 4130m a.s.l. and the lower rock glacier slope on 3830m a.s.l.

A total of 44 GPR profiles were recorded. The total length of the recorded profiles was more than 20km. All profiles taken, showed clear reflections and the stratigraphy could be detected. The penetration depth was variable, but over all between 20-70m. The stratigraphy showed different patterns. Strong reflections in the uppermost 6-8m occurred on all profiles and were caused by air and surface wave arrival and above ground reflectors. Therefore, the estimation of the active layer thickness was difficult.

The ice-debris complex consisted of different, mostly distinct landforms. In order to facilitate the orientation and interpretation, the ice-debris complex was divided in five landform classes: glacier, medial moraine, lateral moraine, rock glacier tongue and glacio-fluvial plain. Here, the GPR profiles for all landform classes are shown.

In order to enhance legibility, all profiles were plotted to the same length. The profile analysis was done in the original profile length. Profiles without comments are found in appendix A.3. Profiles not discussed in this thesis are found in appendix A.4.

#### 5.3.1 Glacier

On the glacier, two longitudinal and a zigzag profile, describing several transects, were taken (see figure 23). VIRL-6 device was used. All profiles cover a distance of 7460m. The electromagnetic velocity for glacier was assumed to be between 0.16m/ns (Davis and Annan, 1989) and 0.167m/ns (Annan, 1999*a*) in (Hubbard and Glasser (2005)). A clear bedrock surface was evident in all profiles.

#### Longitudinal Profile G-L1

The longitudinal profile G-L1 describes a longitudinal section on the western branch of Geologov glacier. The profile had a length of 2080m originating at the glacier tongue (4140m a.s.l.) and ending in the accumulation area (4390m a.s.l.).

The stratigraphy of the profile was characterised by a distinct bedrock reflector, marking the glacier bed. The maximum depth of the bedrock reflector was 135-145m. The mean depth was 80m respectively. Beside the bedrock reflector, two distinct reflection patterns were evident. In the lower part (0-770m) the glacier ice showed no reflections apart from

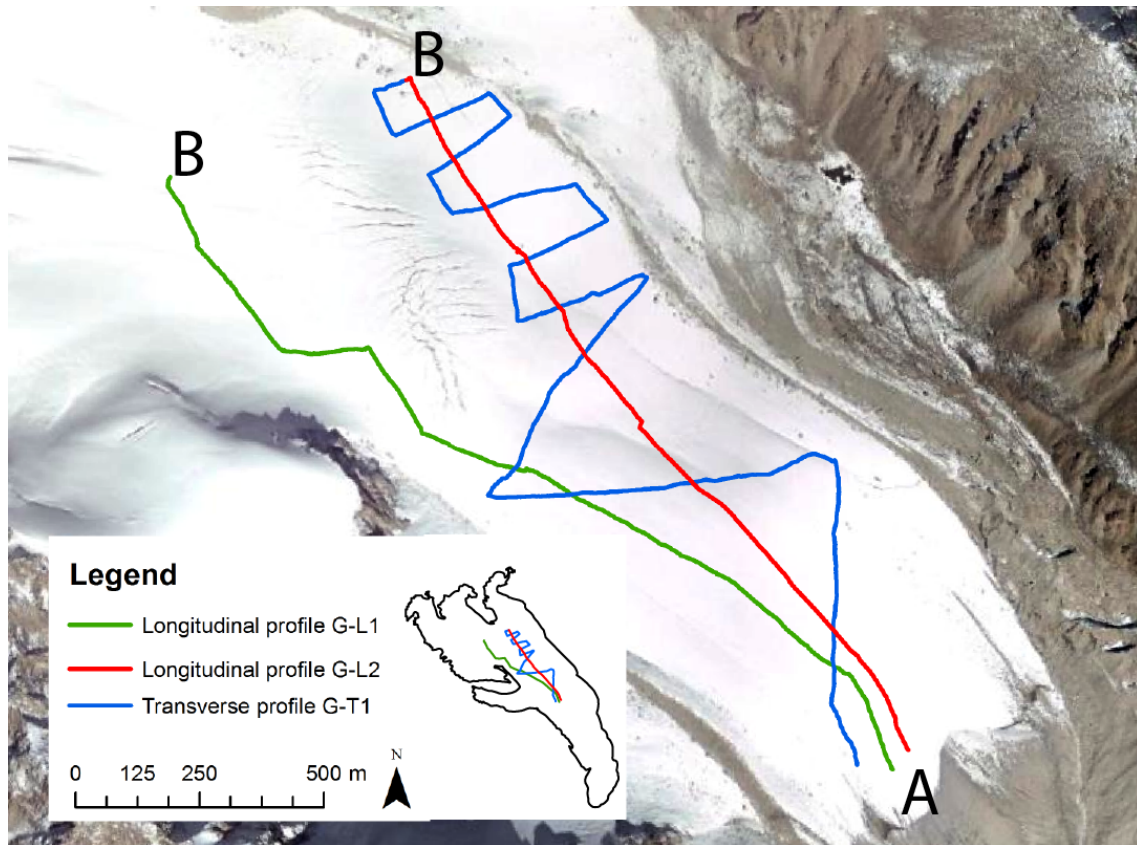


Figure 23: Map of GPR profiles on the glacier (map is based on a GoogleEarth scene)

sporadic low-amplitude hyperbolas, probably caused by buried boulders or crevasses. In the upper part (770-1550m and 1670-1950m) the stratigraphy showed chaotic pattern around the bedrock reflector. The chaotic stratigraphy was built up by overlapping hyperbolas, which were likely indicating temperate ice.

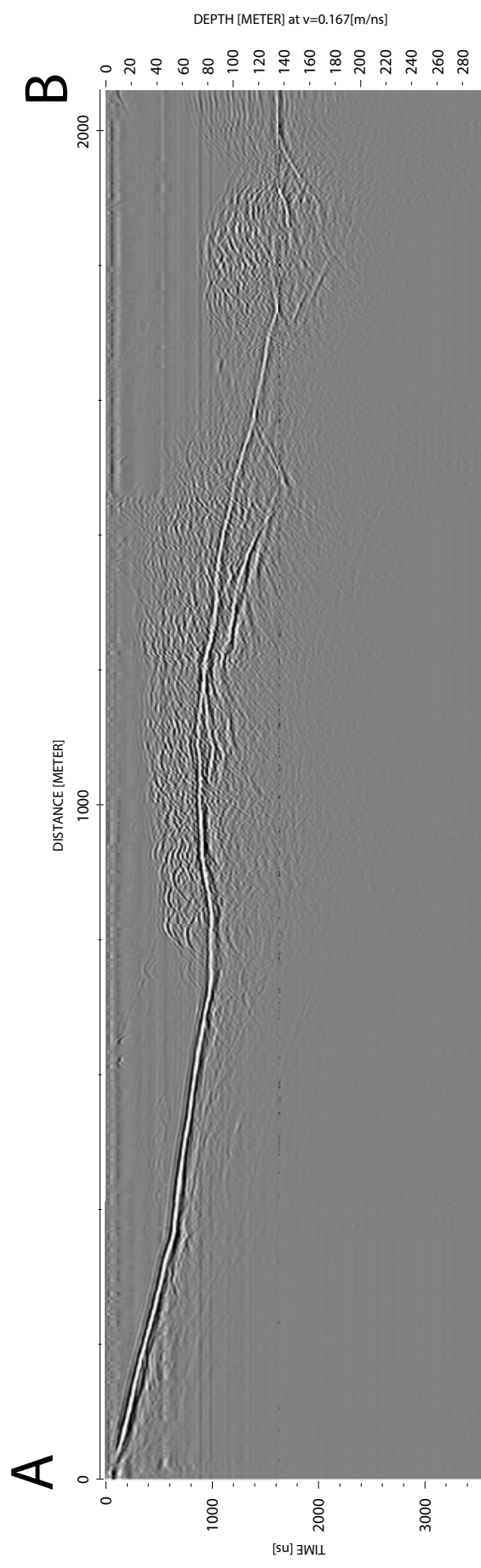


Figure 24: Longitudinal profile G-L1 on the western branch of Geologov glacier

**Longitudinal Profile G-L2**

The longitudinal profile G-L2 had a total length of 1730m, originating at the glacier tongue (4140m a.s.l.) and ending close to a medial moraine. The profile was situated east of the longitudinal profile G-L1. Clear reflections were evident in the whole profile.

The profile G-L2 (see figure 25) was characterised by a distinct bedrock reflector below the glacier ice. The bedrock reflector had a maximum depth of 95-100m and a mean depth of 62m. The stratigraphy of the glacier was almost reflection free, apart from some low-amplitude hyperbolic curves, which were the result of englacial blocks. The stratigraphy of the bedrock showed two different patterns. In the lower part (0-900m) loose low-amplitude reflectors were apparent. In the upper part (900-1730m), stratigraphy was characterised by high-amplitude, steeply inclined reflectors and bedrock parallel reflector bands.

**Transverse Profile G-T1**

The transverse profile G-T1 is built up by several cross profiles, linked to a zigzag shaped profile. The profile was taken in north to south direction, originating at the end of longitudinal profile G-L2 and ending at the tongue of Geologov glacier. The profile had a total length of 3650m.

The most prominent element of the GPR profile (see figure 25) was the undulating bedrock reflector. Undulation was caused by the zigzag acquisition of the profile. The bedrock reflector had a maximum depth of 98-103m and a mean depth of 62m respectively. Beside the bedrock reflector, several hyperbolic curves were evident (e.g. 610-620m and 260-2380m). A more chaotic pattern was evident (2320-2700m), probably indicating temperate ice at the glacier bed. The stratigraphy of the bedrock was more chaotic, as the stratigraphy of the glacier ice.

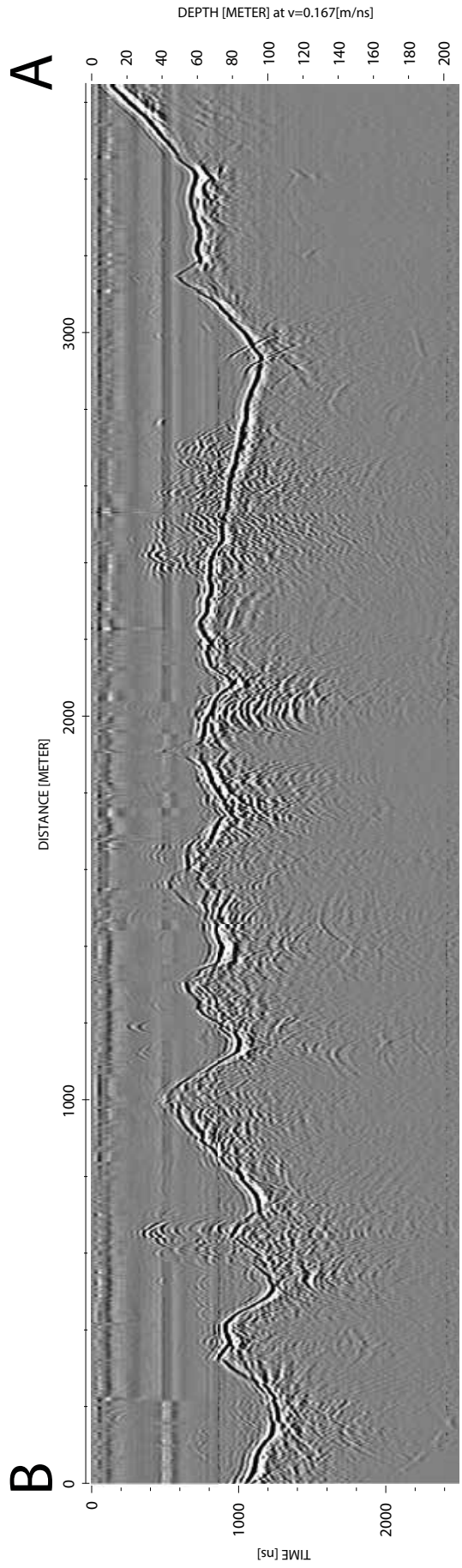
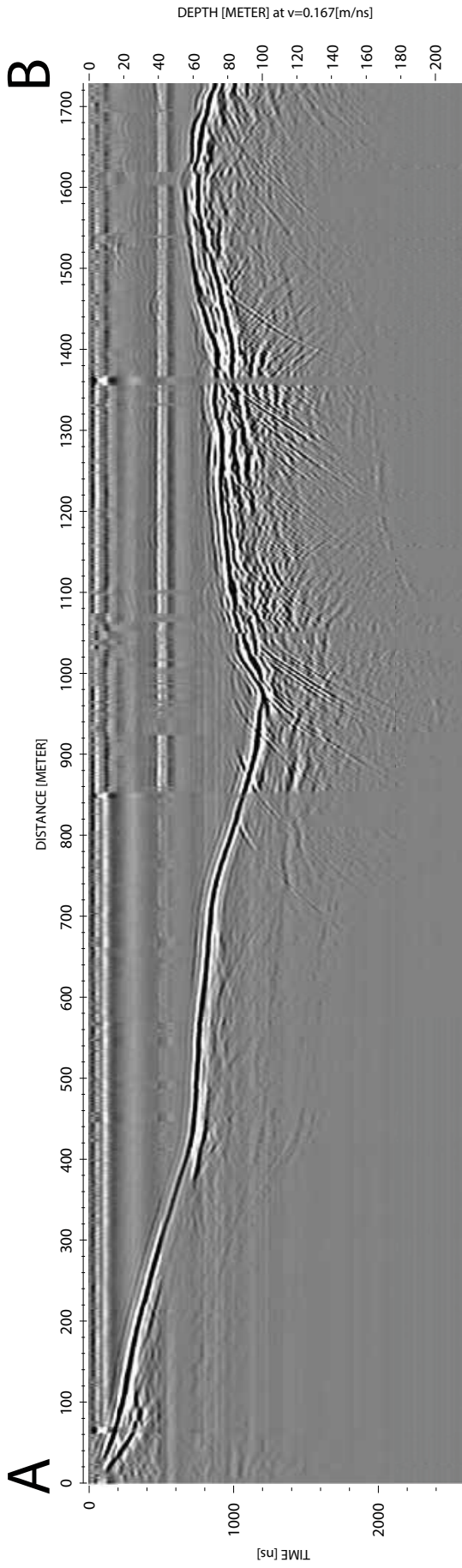


Figure 25: Longitudinal profile G-L2 (left) and zigzag profile (right) taken on Geologov glacier

### 5.3.2 Medial Moraine

On the medial moraine, eight GPR profiles were taken using Malå ProEx (3 profiles) and VIRL-6 (5 profiles). Out of 8 profiles, three merged profiles are showed in this study: two longitudinal and one transverse profile (see figure 26). All profiles cover a total length of 2576m. Clear reflections were detected on all profiles.

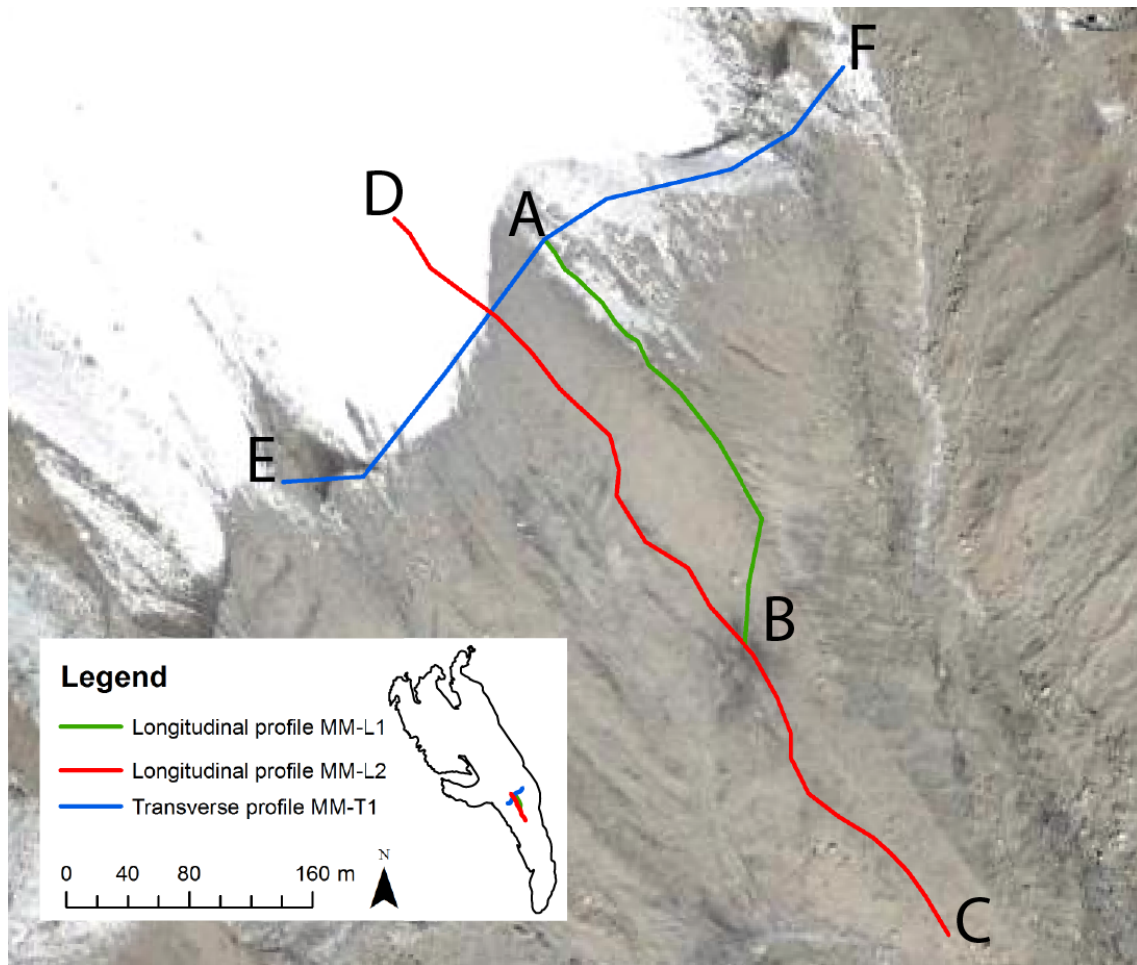


Figure 26: Map of GPR profiles on the medial moraine (map is based on a GoogleEarth scene)

#### Longitudinal Profile MM-L1

The profile MM-L1 (see figure 27) was taken along the medial moraine describing a longitudinal section. The profile was taken in southward direction, ending at the moraine front (see figure 26). Clear reflections were evident in the whole profile.

Most prominent reflectors in the profile were continuous and surface parallel air and ground wave arrivals. Below the surface reflectors, the stratigraphy was characterised by a strong attenuation of reflections within 30-35m. Some distinct reflectors were apparent. A clear dipping layer was visible after 10-30m up to a depth of 25m. The dipping layer was possibly related to a dipping layer found in the transverse profile in 30-40m depth. The reflector was possibly indicating an internal boundary layer. Below the dipping layer, a surface parallel reflector (0-25m) could be found in about 50m depth, which would be interpreted as a bedrock reflector. The depth of the bedrock in the transverse profile was in the same range (about 55m). Another distinct reflector (525-550m) was emerging towards the surface in 20-25m depth. In the lower zone of the profile, another reflector (590-650m) occurred in 20m depth with surface parallel orientation. Both reflectors were interpreted as internal boundary layers, probably indicating buried ice lenses.

Apart from distinct reflectors, low-amplitude reflections occurred. The stratigraphy of these reflectors was variable. In the upper zone (0-200m), reflections were describing weak reflector bands dipping to the south. The dipping reflector bands were interpreted as internal shear horizons of the lateral moraine (cf. Lukas and Sass (2011)). In the central part (200-380m), reflections were mainly undulating. In the steep part, reflections appeared surface parallel, but were slightly undulating. Reflections were deformed due to the topographic correction of the profile. In the lower zone, weak reflection bands were again undulating, but in surface parallel orientation. The stratigraphy could thus be interpreted as the result of layering, during the landform genesis. The mean subsurface velocity was  $0.104 \pm 0.055\text{m/ns}$ .

### **Longitudinal Profile MM-L2**

The second longitudinal profile (see figure 27) was taken using VIRL-6 device. The profile was taken in the opposite direction compared with the longitudinal profile MM-L1. The profile originated out of the tail of the medial moraine, and was orientated in south-to-north direction (see figure 26). The profile had a total length of 886m and reflections were visible in the whole profile. Some noise occurred.

The stratigraphy was characterised by surface parallel reflector bands in the lower zone (0-720m) and a more oblique pattern in the upper zone (720-886m). Several low-amplitude but continuous reflectors were apparent in the lower zone up to 20m depth. A high-amplitude reflector (240-275m) emerged to the surface from 12m depth. The inclined reflector could be interpreted as a shear horizon, caused by unstable slope conditions on the medial moraine. Another high-amplitude reflector (580-660m) was evident in a depth of 23m with surface parallel orientation. The reflector was probably proceeding

up to the top of the medial moraine (800m), but the reflector was disturbed by some noise. This reflector could be interpreted as an internal boundary layer. The top part of the medial moraine was characterised by a more oblique stratigraphy. Another high-amplitude, surface parallel reflector (705-760m) was detected in about 12m depth. A deep layer (830-880m) was found in 50m depth, slanting up to 30m. The slanting reflector would be interpreted as a bedrock reflection. Since the longitudinal profile L2 was not crossing the top of the medial moraine, the bedrock in 30m depth is correlating with the bedrock detection in 50m depth on top of the moraine. The mean subsurface velocity was  $0.13 \pm 0.6 \text{m/ns}$ , but only few suitable hyperbolas were found.

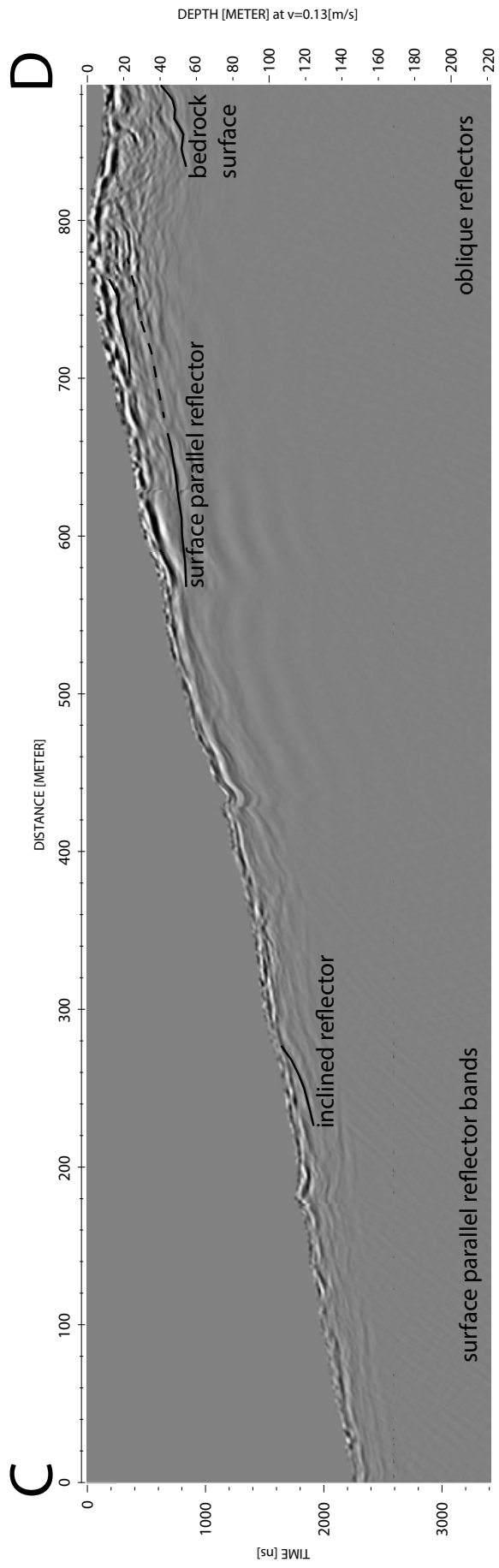
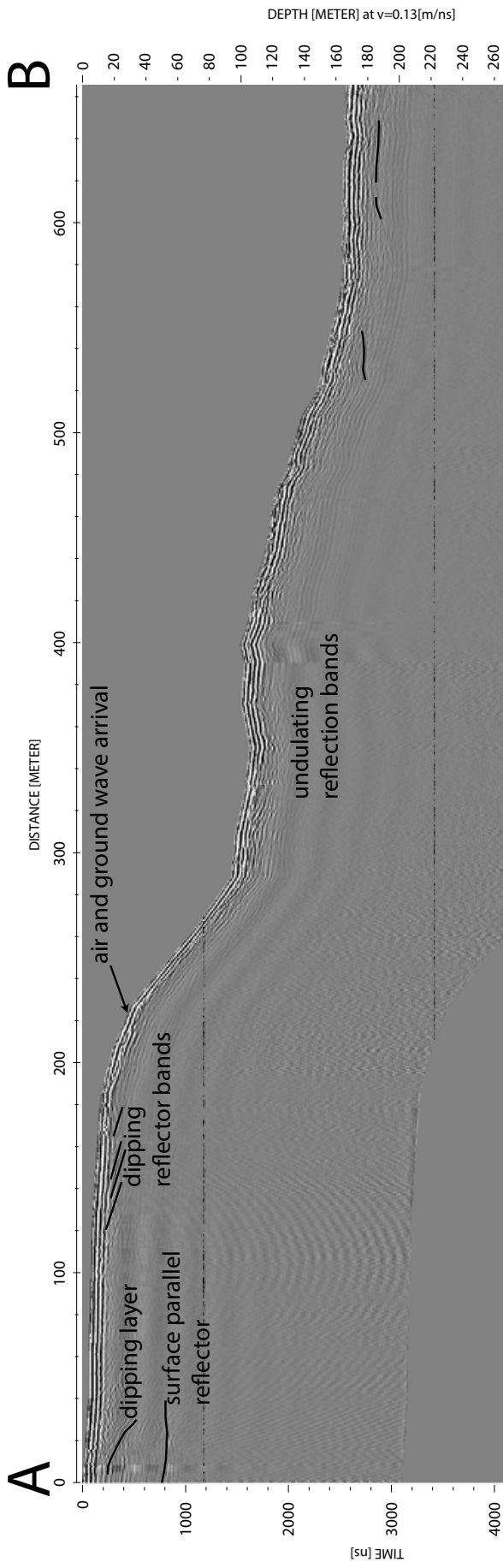


Figure 27: Longitudinal profiles on the medial moraine: Longitudinal profile MM-L1 (left) and longitudinal profile MM-L2 (right)

**Transverse Profile MM-T1**

The transverse profile MM-T1 (see figure 28) described a clear transect of the medial moraine, in west-to-east direction. This profile is a result of three merged profiles. The total length of the profile was 450m. Clear reflections occurred along the whole profile and many distinct reflectors were evident.

The stratigraphy was characterised by surface parallel reflection bands (0-55m, 175-225m and 285-450m) as well as several clear visible internal high-amplitude reflectors. Unstratified, chaotic reflections occurred on the western slope (60-170m) and on top of the medial moraine (225-285m). The chaotic stratigraphy is a potential indicator for ice rich debris. Several distinct reflectors were evident. A continuous and surface parallel reflector (0-50m) was found in 15m depth. Another surface parallel reflector (170-205m) was evident in 20 depth. The surface parallel reflectors were probably indicating internal boundary layers caused by glacial deposits (Lukas and Sass, 2011). A slanting layer (100-115m) was dipping from the surface in eastern direction. The inclined layer was cutting off a zone with oblique high-amplitude reflectors. The high-amplitude reflectors were possibly indicating an ice-rich layer. The curve fitting in this zone, resulted in a subsurface velocity of 0.16m/ns.

Two prominent reflectors (230-260m) were found in 55m depth, probably marking the bedrock surface. The reflectors were dipping in eastern direction and were in the same depth as the possible bedrock reflectors in the longitudinal profiles. Another prominent reflector (330-385m) was evident as a continuous slightly dipping layer. The reflector was situated in 30-40m depth. Other high-amplitude reflectors (250-280m) in 35m were likely extending this continuous reflector to the top of the moraine. The reflector could be interpreted as an internal boundary layer, indicating the lower end of the ice-rich moraine deposits.

The radial reflections (400-450m) were due to the influence of water. After 430m a small glacial stream was crossed, likely causing these radial reflections. The GPR signal was amplified by contact with water. The mean subsurface velocity was  $0.128 \pm 0.022$  m/ns. High velocities (0.15-0.16m/ns) were measured close to the surface. Ice rich debris or massive ice is therefore likely to occur on the medial moraine.

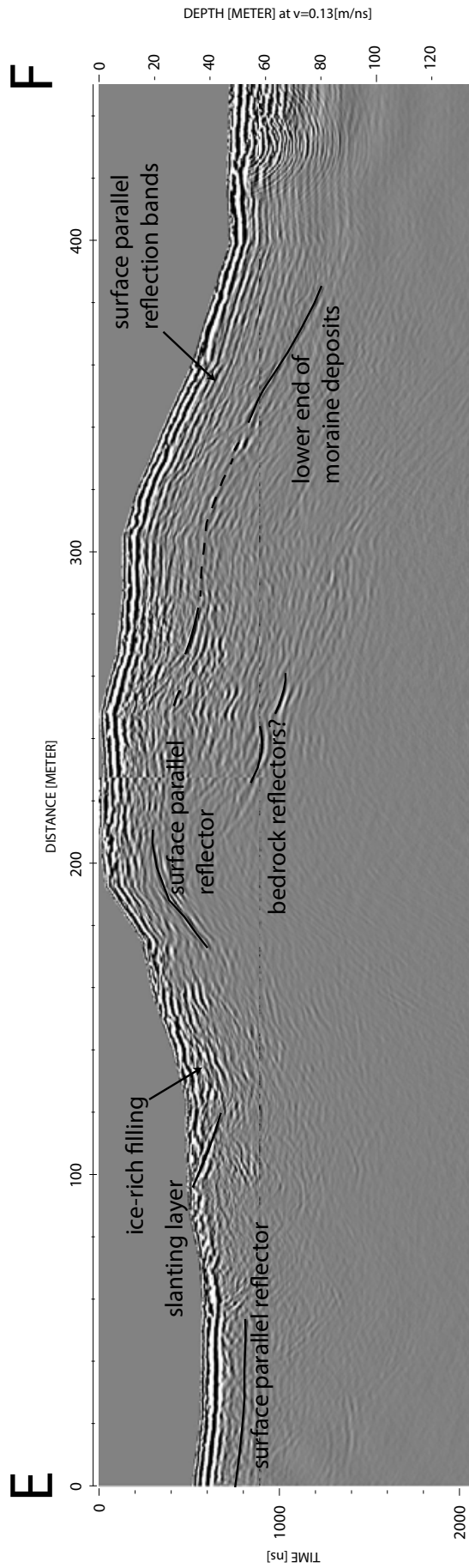


Figure 28: Transverse profile MM-T1 on the medial moraine

### 5.3.3 Lateral Moraine

The orographic left lateral moraine was investigated using Malå ProEx device. A longitudinal and a transverse profile were realised (see figure 29). The total length of the profiles was 1264m. Both profiles showed clear recognisable reflections.

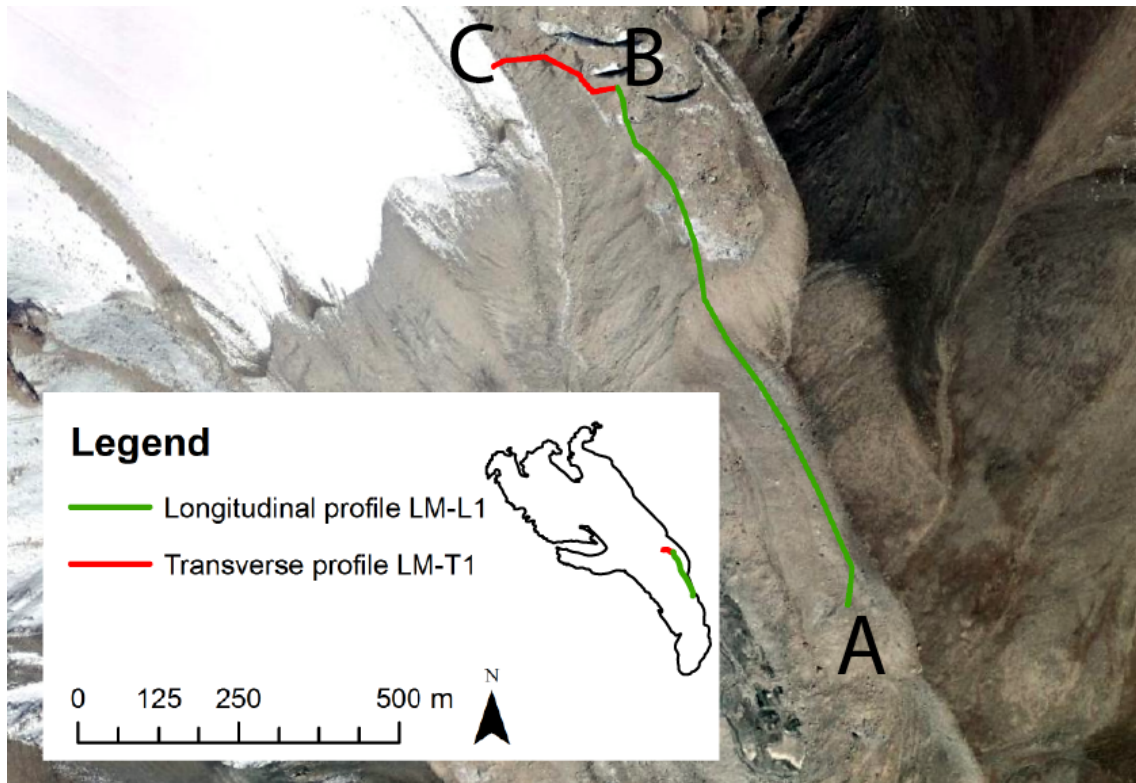


Figure 29: Map of GPR profiles on the lateral moraine (map is based on a GoogleEarth scene)

#### Longitudinal Profile LM-L1

The longitudinal profile LM-L1 (see figure 30) describes a longitudinal transect of the lateral moraine. The profile was recorded in south-north direction, originating out of the lower end of the moraine. The profile had a total length of 1031m. Clear reflections were evident in the whole profile. The profile could be characterised by a high-amplitude surface parallel reflector band close to the surface. Below these reflectors, a more chaotic and strongly attenuating stratigraphy appeared.

The strong surface reflectors were due to air and ground wave arrivals, which were intensified by the rough and blocky surface of the lateral moraine. Apart from surface reflectors,

the stratigraphy of the profile could be divided in two zones. A lower zone (0-680m) which was characterised by a strong signal attenuation in 20-25m depth and an upper zone (680-1031m), which would be characterised by strong and oblique reflections.

In the lower zone, no distinct stratigraphy was apparent, but some clear reflectors were visible. A clear reflector was evident (120-150m) in a depth of 15m. Another reflector (490-560m) was detected, in a depth of 15m. A potential correlation between these two reflectors could not be found. A possible explanation of these reflectors would be the occurrence of buried ice lenses. The reflectors could be caused by the lower end of buried massive ice. Subsurface velocities of 0.15-0.16m/ns were measured along hyperbolas, right above the reflectors. Buried obstacles have similar electromagnetic properties, as clear ice. Hence buried massive ice is very likely to occur, above these distinct reflectors. The appearance of massive ice is strengthened, by a typical stratigraphy of overlapping small hyperbolas (Moorman et al., 2003). Between 130-570m an interrupted, weak reflector was visible in depths of 40-65m. The reflector could be caused by the bedrock surface.

The upper zone (680-1031m) of the profile, was characterised by a strong and chaotic stratigraphy, which reached depths of 50m. In comparison to the lower zone, reflections in the upper zone showed higher amplitudes. The strong oblique reflectors, were interpreted as the result of an ice-debris matrix. Strong reflections could be caused, due to different electromagnetic velocities of ice and debris.

A surface parallel reflector (800-850m) in 12m depth could be distinguished, likely indicating buried massive ice. A weak reflector (980-1031m) could be detected, dipping up from 45m to 30m, potentially indicating the bedrock surface.

The separation of the lower and the upper zone was correlating with the surface topography. In the upper zone, the lateral moraine was significantly wider than in the lower zone. Based on the topography and stratigraphy, the upper zone was therefore interpreted as an ice-cored moraine, whereas, the lower zone could be interpreted as a lateral moraine with less ice content. The mean subsurface velocity was  $0.135 \pm 0.02$  m/ns. About 0.1-0.16m/ns in the lower zone and 0.1-0.15m/ns in the upper zone.

### **Transverse Profile LM-T1**

The transverse profile (see figure 30) showed a transect of the western slope of the lateral moraine (see figure 29). The profile was recorded in a east-to-west direction, starting at the top of the moraine and ending at the margin of the glacier. The profile had a total length of 233m and reflections were clearly visible in the whole profile.

The profile showed clear reflections building a chaotic stratigraphy. The signal depth decreased towards the glacier from 70-100m depth(0-60m distance) to 40-60m depth (60-

190m) and 25-30m depth (190-233m). Two prominent reflectors were evident. The first reflector (5-58m) had a syncline shape. The depth of the reflector was 9-18m. Above this reflector, a relatively reflection free zone occurred. The syncline reflector could be interpreted as the lower boundary of buried massive ice. Below this prominent reflector, three less prominent but more or less parallel reflectors occurred in depths of 30m, 45m and 65m respectively. These reflectors probably showed the stratification of ice and debris layers.

A second prominent reflector (170-230m) was evident in a depth of 25-40m. The reflector had again a syncline shape and could be interpreted as bedrock surface or the lower buried margin of the lateral moraine. Again, indicators for buried ice occurred above this reflector. Hence, massive ice of up to 25m thickness could be expected.

In the center of the profile (60-110m) a zone with little reflection occurred, close to the surface. A maximum depth of 20m was apparent. Next to the reflection zone, a zone with little distinct reflections and a rather oblique stratigraphy was found. In this part of the lateral moraine, massive ice (reflection free zone) and ice-rich debris (oblique stratigraphy) is likely to be expected. The mean subsurface velocity was  $0.11 \pm 0.038$  m/ns, but only few suitable hyperbolas were found.

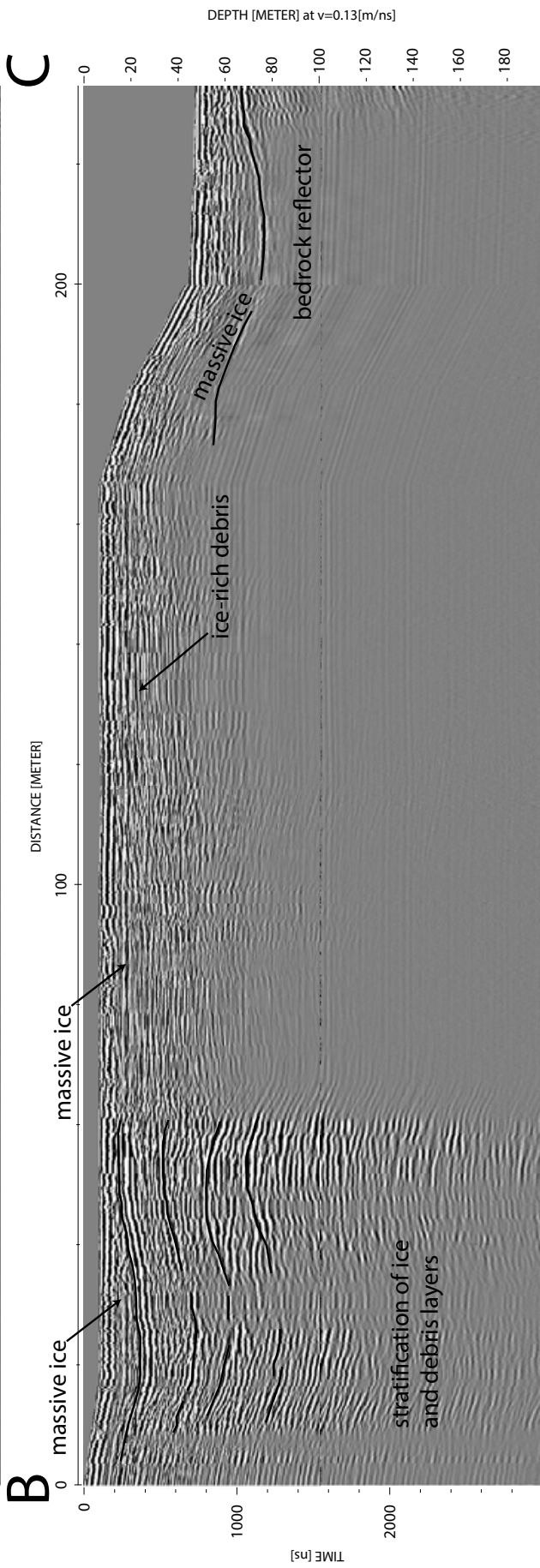
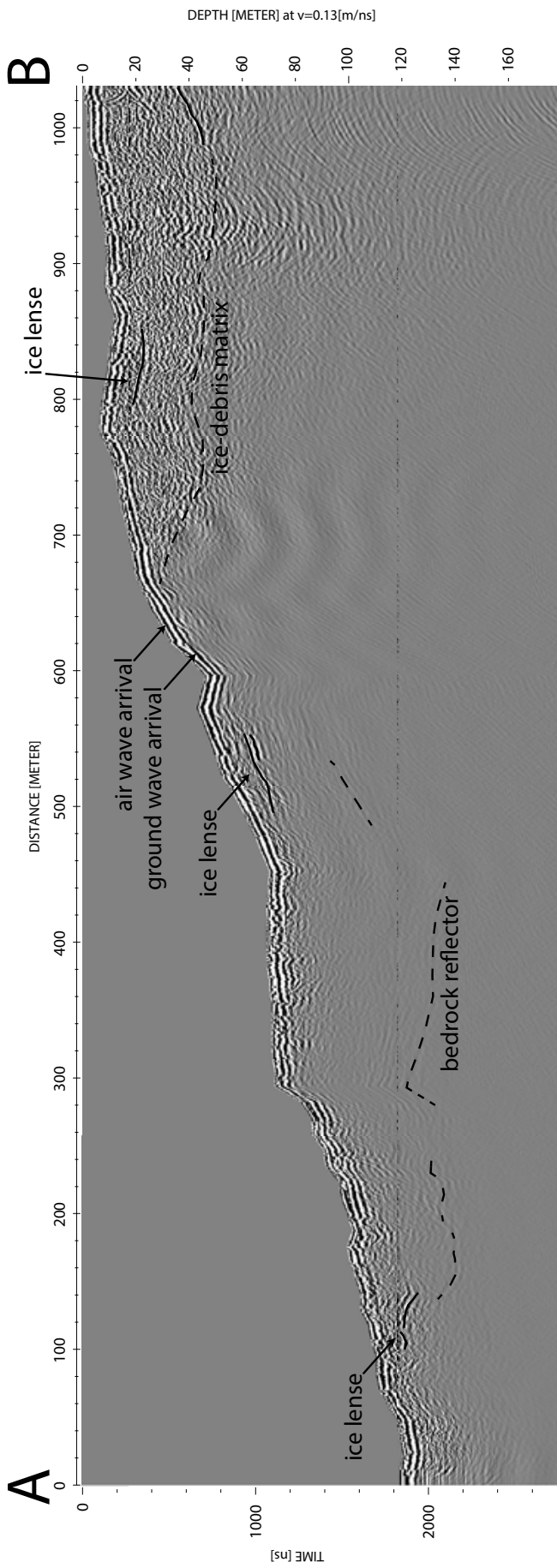


Figure 30: GPR profiles on the lateral moraine:  
 Longitudinal profile LM-L1 (left) and transverse profile LM-T1 (right)

### 5.3.4 Rock Glacier Tongue

At the rock glacier tongue, a total of 15 GPR profiles were taken, using VIRL-6 device (see figure 31). The total profile length was about 7.1km. All profiles showed clear visible reflections. A severe signal distortion occurred between 500-700ns, making the identification of reflections in this part difficult.

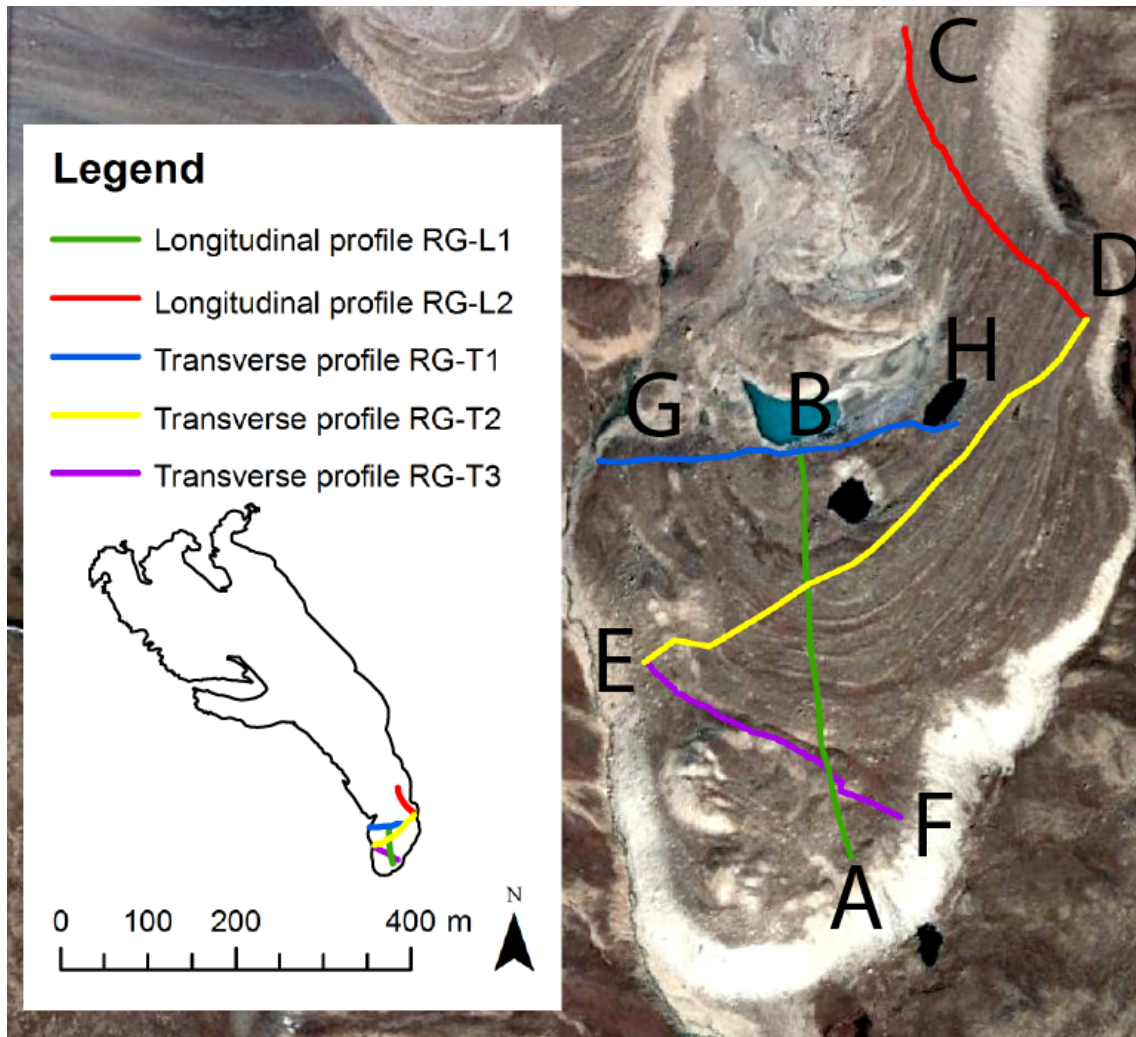


Figure 31: Map of GPR profiles on the rock glacier tongue (map is based on a GoogleEarth scene)

#### Longitudinal Profile RG-L1

The lower longitudinal profile RG-L1 had a total length of 571m. The profile was taken

against flow direction of the rock glacier, starting at the rock glacier front and ending close to a periglacial lake. The profile showed clear identifiable stratigraphy, down to a depth of 40m (front) and to a depth of 50m (upper part).

The stratigraphy of the profile RG-L1 (see figure 32) was characterised by weak surface parallel reflector bands in the lower part (0-220m) of the profile. In the upper part (220-571m), a more chaotic stratigraphy prevailed. Two strong surface parallel reflectors were evident in the lower part of the profile. The first reflector (15-35m) in 20m depth and the second reflector (190-245m) was evident in 15m depth. More less pronounced reflectors were visible. The surface parallel stratigraphy could be interpreted as different internal layers. The surface parallel reflectors in rock glaciers are commonly explained as the result of frequent mass movements covering snow cover in the rooting zone of rock glaciers (Berthling et al., 2000; Degenhardt, 2009; Farbrot et al., 2005). Hence the surface parallel reflectors were likely caused by alternating layering of rockfall deposits and snow cover or avalanches.

The stratigraphy of the upper part was characterised by chaotic and undulating reflectors. A syncline layer (260-290m) was found in 20-25m depth. The most prominent element of the profile were several reflectors (340-380m), slanting up to the surface. The slope of the dipping layers was between 21-44°. The slope of these inclined layers was less steep, than inclined layers, measured on another rock glacier in the northern Rocky Mountains (see Florentine et al. (2014)). The slanting layers were likely related to the concave ridges at surface. The transverse ridges are a potential indicator for the internal deformation. Hence the slanting layers were interpreted as debris bands, deformed by creep behaviour of the rock glacier tongue (Florentine et al., 2014; Fukui et al., 2008). Based on hyperbola fitting, the estimated subsurface velocity was 0.06-0.12m/ns in the lower part and 0.06-0.155m/ns in the upper part respectively.

A mean velocity of  $0.11 \pm 0.029$ m/ns resulted.

### **Longitudinal Profile RG-L2**

The second longitudinal profile RG-L2 (figure 32) had a length of 439m. The profile was located at the eastern margin of the rock glacier tongue. The profile was taken in flow direction of the rock glacier (see figure 31). The stratigraphy of the profile showed strong reflections in the upper 10-13m, followed by a surface parallel or slightly undulating pattern.

The strong surface reflector was likely due to ground and air wave reflections. The surface reflector was followed by a zone of sub parallel reflections, which occurred up to a depth

of 40-50m. Surface parallel reflections start to become more undulating after 220m. A distinct surface parallel reflector (60-240m) was evident in 25-30m depth, probably indicating the bedrock surface. Two smaller, horizontally situated reflectors (105-170m) were evident in a maximum depth of 20m, emerging to the surface. A possible explanation of these reflectors, could be an internal water flow path. Emerging water was observed close-by, reinforcing the possibility of internal water flow paths. In the lower part of the profile (300-400m) a clear reflector was visible in a depth of 70m, slanting up to 50m. This reflector could again be interpreted as a bedrock indicator. The depth of the bedrock reflection was significantly deeper than further up in the profile. Compared to the height of the rock glacier tongue, the bedrock was expected in shallower depth. The deep bedrock reflector could be interpreted as a debris filled glacial over deepening. The estimated subsurface velocity was 0.1-0.13m/ns in the upper part (0-300m) and 0.05-0.07m/ns in the lower part (300-439m) respectively. Thus, the mean subsurface velocity was  $0.093 \pm 0.03$  m/ns.

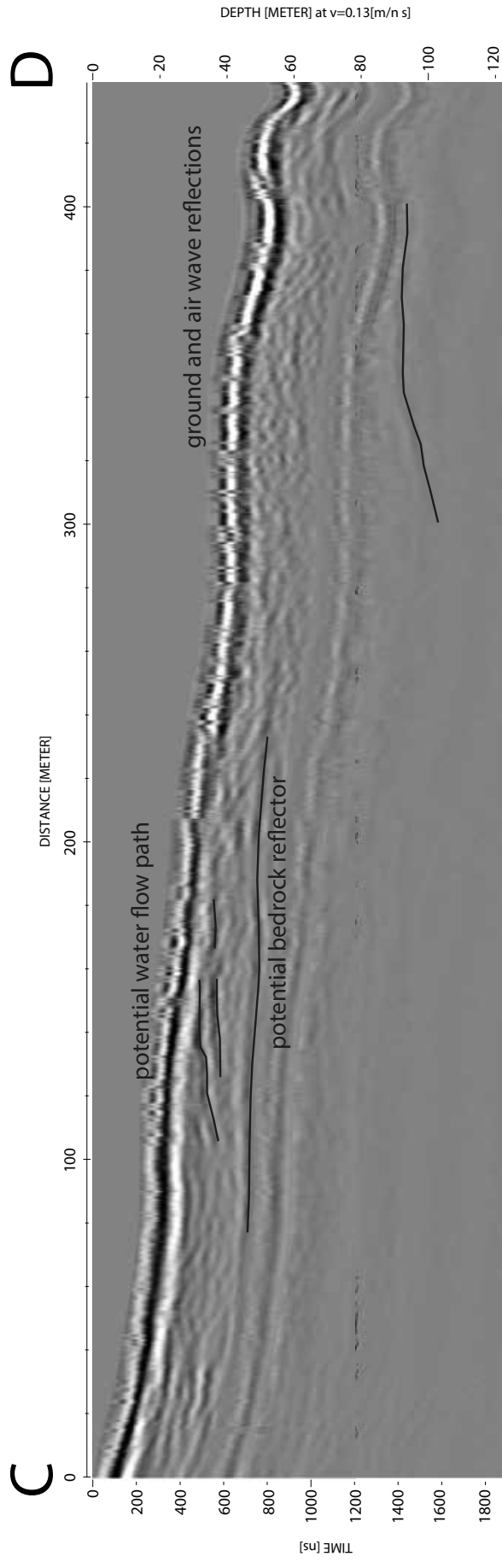
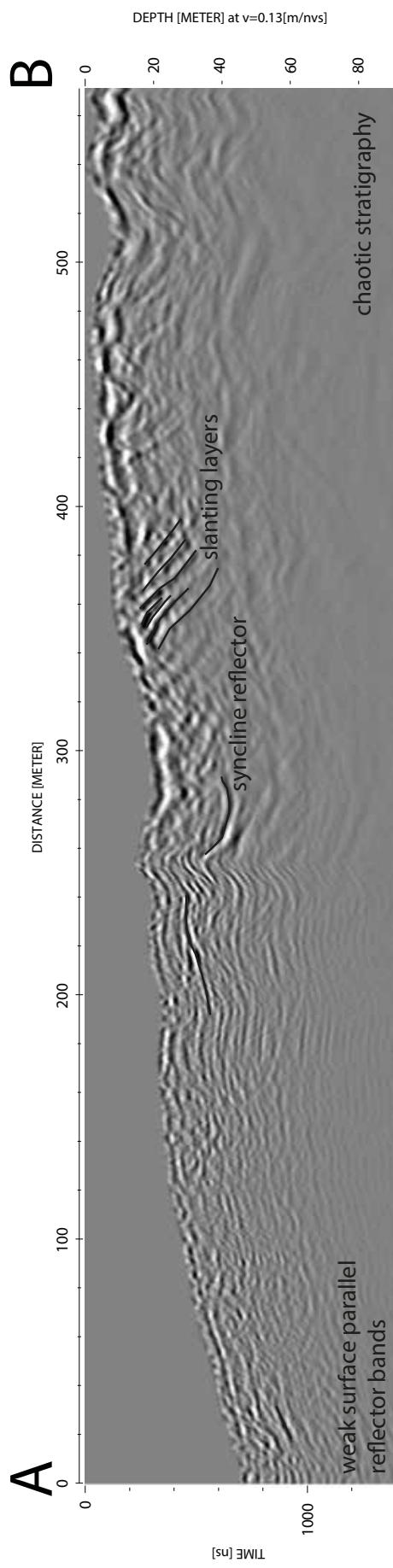


Figure 32: Longitudinal profiles on the rock glacier tongue: RG-L1 (left) and RG-L2 (right)

**Transverse Profile RG-T1**

The transverse profile RG-T1 describes a clear transect of the upper part of the rock glacier tongue (see figure 31). The profile had a total length of 461m, and was taken in west-to-east direction.

The stratigraphy (see figure 33) was characterised by weak surface parallel reflections in the eastern part (0-100m) and a chaotic pattern caused by overlapping of inclined layers in the western part (100-461m). Clear reflections were apparent to a depth of 50m. Below 50m, reflections started to fade out. A strong reflector (170-230m) was found in 75-80m depth, probably indicating the bedrock surface.

Several high-amplitude short reflectors (e.g. 105-115m, 195-200m) were found in 10-15m depth, building a surface parallel line. The reflectors were likely caused by buried boulders or ice lenses. In the unmigrated profile, these point reflectors occurred as hyperbolic curves, but were geometrically corrected, using the migration function. The hyperbolas were used to estimate the subsurface velocities of the point reflectors. The estimated velocity was 0.12m/ns (65-75m), 0.12-0.17m/ns (195-200m) and 0.13-0.17m/ns (270-275m). Clear ice has an electromagnetic wave velocity of 0.167m/ns see table 3 in methods section 4.3.1. The estimated velocity showed similar values. Hence, buried ice-lenses could be expected in depths of 10-15m.

Further, weak low-amplitude reflectors were apparent. The reflectors were building syncline structures, dipping up to surface in eastern direction. Visible ridges on the rock glacier surface, lead to the assumption, that slanting reflectors were also caused by internal deformation. Syncline structures in transversal GPR profiles were also found in other studies and interpreted as slanting debris-rich layers, related to ridges at surface (Fukui et al., 2008; Monnier et al., 2013). Thus, the inclined layers were likely indicating internal deformation due to rock glacier creep. The mean subsurface velocity was  $0.1 \pm 0.034$ m/ns.

**Transverse Profile RG-T2**

The second transversal profile RG-T2 described a more diagonal transect of the rock glacier tongue (see figure 31). This profile was taken diagonal to the flow direction, in south-western direction. The profile was originating at the north-eastern margin and had a total length of 717m. The stratigraphy could be clearly distinguished in the whole profile. In the upper 30m, the reflections were well recognizable. In a depth of 30-70m the reflections were less clear distinguished. Below 70m no reflections were detectable.

The stratigraphy (see figure 33) was characterised by undulating reflector bands in surface parallel orientation. Undulating reflector bands were overlapped by weak, strongly inclined, hyperbolic reflections, letting the stratigraphy look chaotic. Strongly inclined

reflections, could be interpreted as multiple hyperbolas, caused by many small ice lenses (Moorman et al., 2003). Therefore, smaller ice lenses are likely to be found. The composition of the rock glacier tongue could be expected to be an ice-debris mixture, which is commonly accepted (e.g. (Haeberli et al., 2006)).

Some distinct, surface-parallel reflectors were visible. An almost surface parallel reflector (5-40m) was apparent in 13-15m depth. Other reflectors were found in 21m depth (260-290m) and 15m depth (590-615m). The layered stratigraphy could be explained as the result of stratified ice and debris layers. The stratification was the result of rockfall and avalanche events in the rooting zone of the rock glacier.

A high-amplitude reflector (45-70m) was evident in the upper part of the profile. The reflector was dipping from 10 to 20m depth, probably indicating an internal shear horizon. A deep low-amplitude reflector was evident, most likely caused by the bedrock surface. This bedrock reflector was found in 50m depth after 100m, dipping to more than 80m depth, after 450m. A thickness of 80m could be strengthened by comparison with the valley topography. The estimated subsurface velocity was  $0.12 \pm 0.031 \text{m/ns}$ .

### **Transverse Profile RG-T3**

The third transversal profile RG-T3 (see figure 33) described another diagonal transect of the rock glacier tongue. This transect was recorded in south-eastern direction. The profile originated at the end of the profile RG-T2 (see figure 31). The total length of the profile was 375m. In the whole profile, the stratigraphy was clearly detectable to depths of 30-40m. No reflections were detected below 70m.

The stratigraphy of the profile was characterised by undulating and chaotic reflections in the upper part (0-120m) of the profile and mainly weak surface parallel reflection bands in the lower part (120-375m) of the profile. The most prominent reflectors were found in the upper part of the profile. A surface parallel high-amplitude reflector (17-42m) was found in 25m depth. This reflector was surrounded by more distinct, surface parallel reflectors (5-15m and 50-60m) in a about 20m depth.

Another distinct reflector was found in the middle section of the profile (120-160m), dipping from 8 to 17m. The reflector may be a shear horizon and is possibly related to the bulge-like features visible on the surface. Just below this dipping layer, a further distinct reflector was found (140-180m) in a depth of 20m. The reflector was orientated parallel to the surface and was probably indicating an internal boundary between materials with different electromagnetic velocities. The stratification could be explained, as the result of rockfall and avalanche deposits in the rooting zone of the rock glacier.

In the lower part of the profile, surface parallel reflection bands dominated. The reflection

bands were interrupted by several syncline reflectors, dipping up to the surface in north-western direction. Syncline reflectors could be again interpreted as the result of internal deformation, due to rock glacier creep.

Between 100-200m, a clear reflector in a depth of 70m was apparent. The deep reflector could be related to the bedrock surface. The depth of the bedrock surface was correlating with the bedrock reflectors in the profiles RG-T1 and RG-T2. The estimated subsurface velocity was  $0.094 \pm 0.024 \text{m/ns}$ .

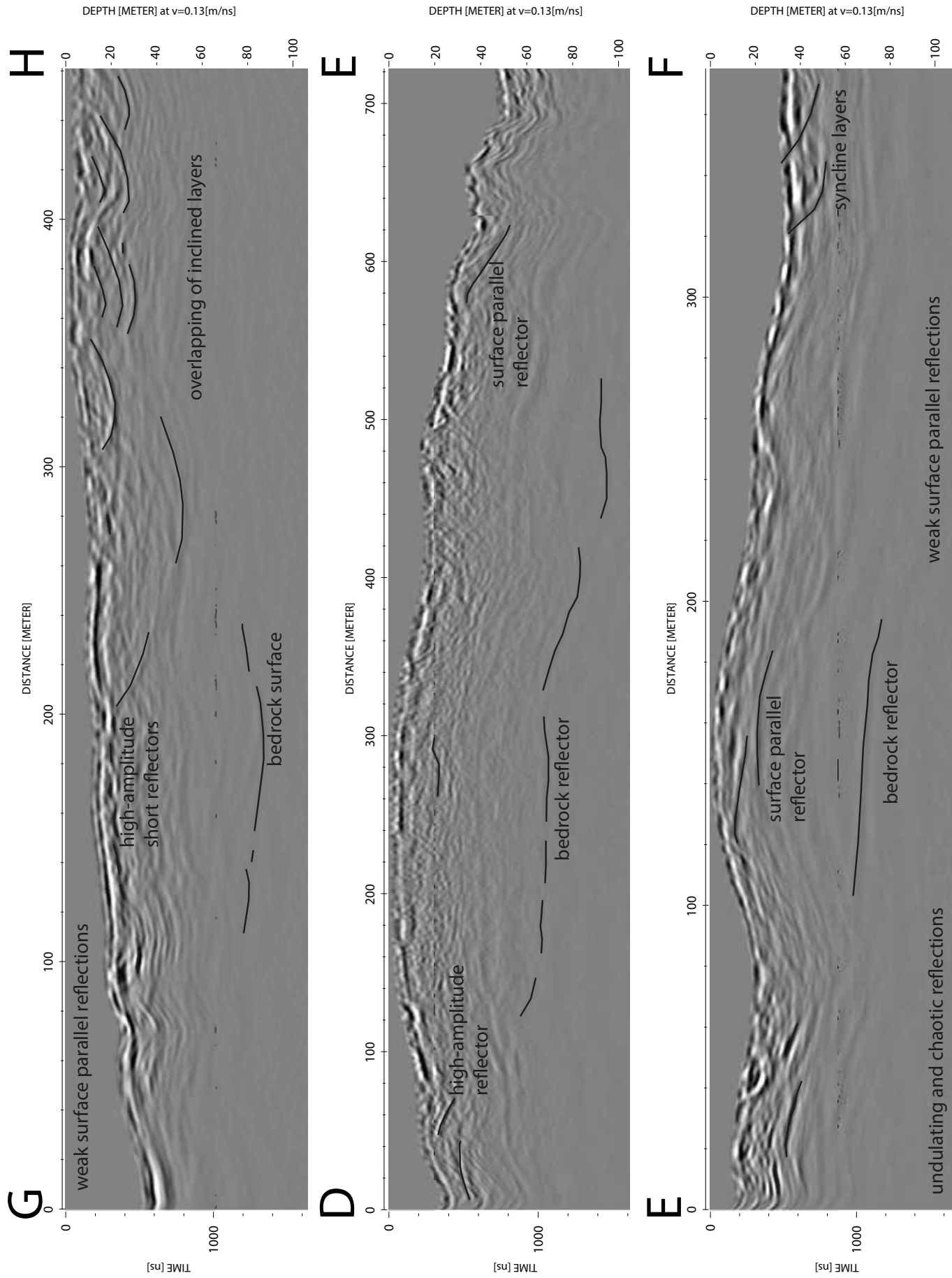


Figure 33: Transverse profiles on the rock glacier tongue: RG-T1 (left), RG-T2 (center) and RG-T3 (right)

### 5.3.5 Glacio-Fluvial Plain

On the glacio-fluvial plain, one longitudinal and one transverse profile were taken (see figure 34). The longitudinal profile was recorded using Malå ProEx, and the transverse profile using VIRL-6. The profiles had a total length of 842m. Reflections were found in both profiles.

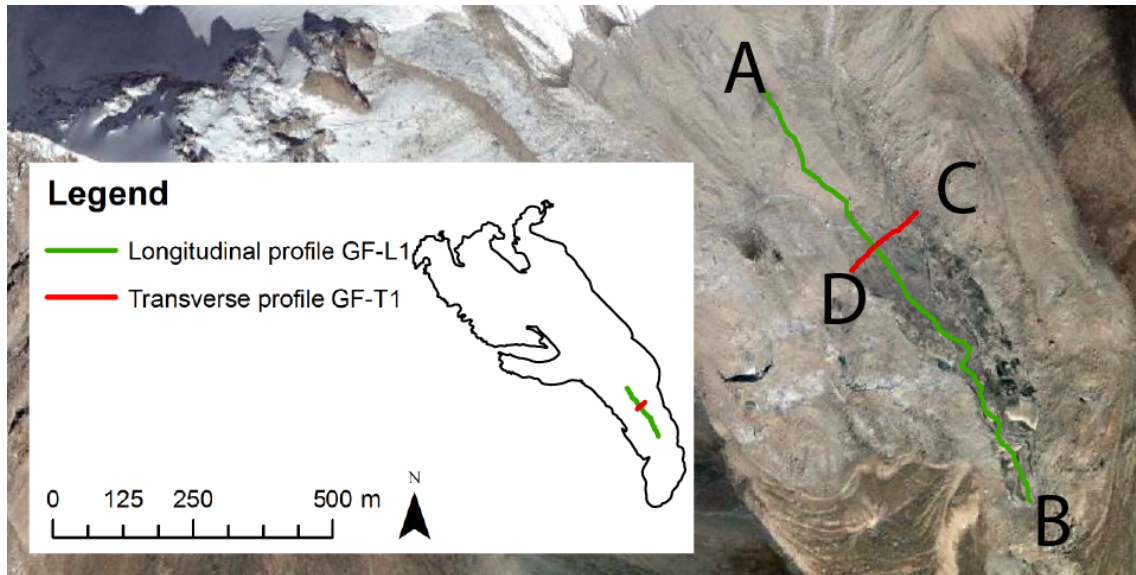


Figure 34: Map of GPR profiles on the glacio-fluvial plain (map is based on a GoogleEarth scene)

#### Longitudinal Profile GF-L1

The longitudinal profile GF-L1 (see figure 35) was in north-to-south direction, starting at the tail of medial moraine. The profile had a total length of 672m. Reflections were visible in the whole profile.

The stratigraphy of the profile could be characterised by continuous surface parallel reflections in the upper part of the profile followed by a rather oblique pattern. Two prominent zones were apparent where a chaotic stratigraphy was visible to a depth of 30m (0-200m) and 40m (270-515m). The second zone of the oblique stratigraphy was built up by several syncline hyperbolas. Besides the two zones, an oblique stratigraphy was visible as low-amplitude reflections up to a depth of 75m.

In the second prominent zone, a dipping reflector (300-360m) was visible. The reflector was dipping from 10m to a depth of 30m and was likely describing the lower margin of the glacio-fluvial sediment fillings. A distinct, syncline reflector (630-660m) was evident

in a depth of 40-45m. The reflector was probably indicating the bedrock surface. Surface parallel reflections were probably caused by air and ground wave arrivals, but likely also by fluvial sedimentation, as not only two but more than six reflectors were apparent. Such a stratified pattern often appears in fluvial sediments (cf. Beres et al. (1999)). The higher penetration depths in the two prominent zones were possibly caused by the occurrence of liquid water. The estimated subsurface velocity was  $0.096 \pm 0.022 \text{m/ns}$ .

### **Transverse Profile GF-T1**

The transverse profile GF-T1 (see figure 35) described a transect of the flood plain. The profile was in a north-eastern direction. The profile origin was on the south-western margin. The profile had a total length of 173m. Reflections were visible along the whole profile.

The stratigraphy of the profile could be characterised by several high-amplitude reflectors in surface parallel orientation. The reflectors were visible up to 40m depth, but deepest reflectors and reflectors with high-amplitudes were found in the center of profile. These parallel reflections were likely caused by glacio-fluvial sedimentation processes.

A high-amplitude reflector (10-30m) was found in about 20m depth, in surface parallel orientation. The reflector was probably correlated with a discontinuous high-amplitude reflector (40-90m) in the same depth. The high-amplitude reflector could be interpreted as an internal boundary layer, probably caused by the lower end of glacio-fluvial fillings. An inclined reflector (100-115m) was apparent in 40m depth. The reflector could likely be extended, building a syncline layer around the prominent zone. The reflector was probably indicating the lower margin of glacio-fluvial stratification. 15m below this reflector, another distinct reflector was evident. The reflector was probably indicating the bedrock surface in a depth of 55m. The bedrock detection was in greater depth, as in the longitudinal profile GF-L1. Since the bedrock was detected further south in the longitudinal profile, no correlation between these two bedrock reflectors could be made. The subsurface velocity was  $0.1 \pm 0.03 \text{m/ns}$ , but only few suitable hyperbolas were found.

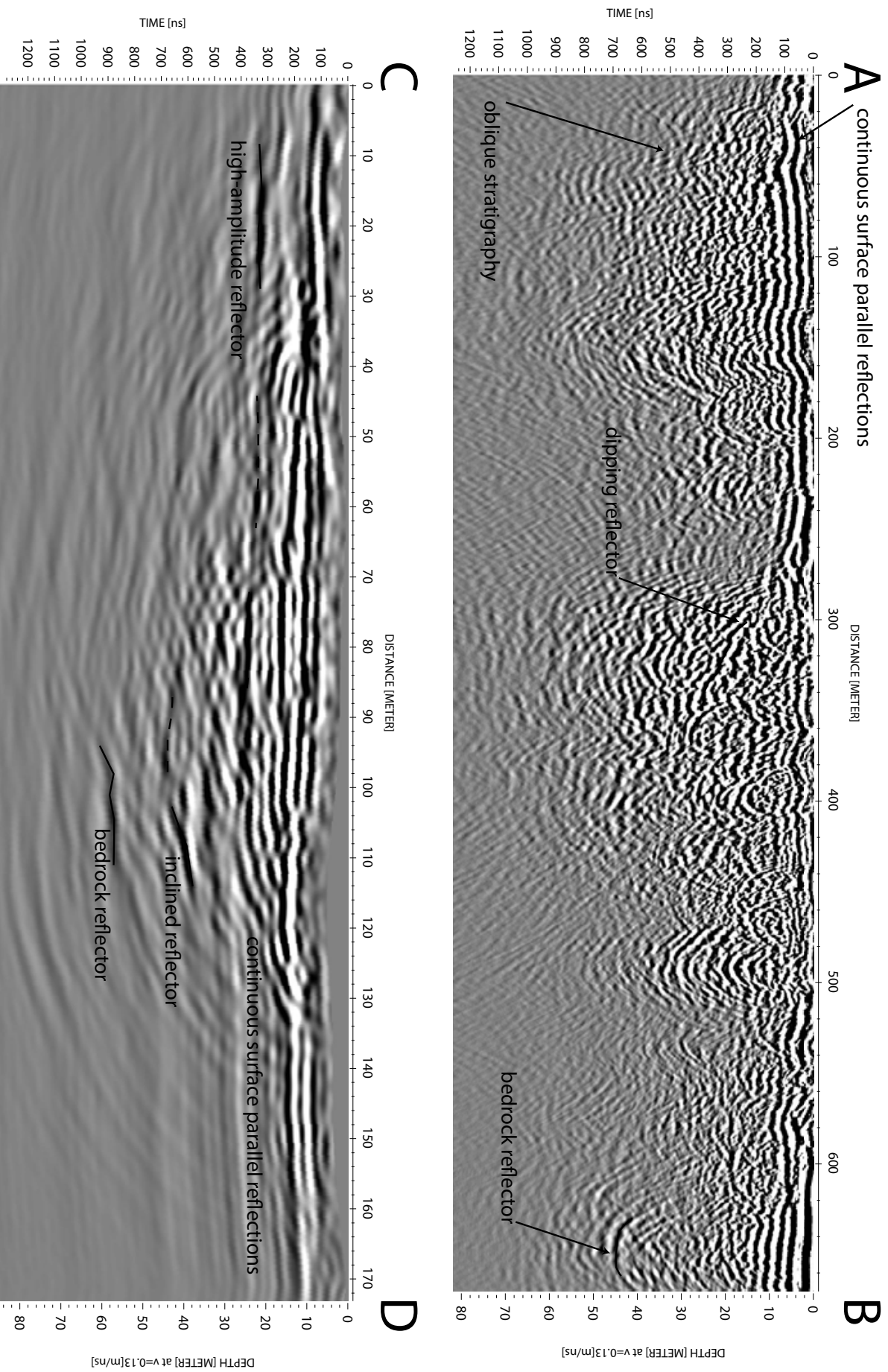


Figure 35: GPR profiles on flood plain GF-L1 (left) and GF-T1 (right)

## 6 Discussion

GPR measurements on glaciers are widespread and provide good results (e.g. Kutuzov et al. (2015); Machguth et al. (2006)). GPR is also used to study the internal structures of rock glaciers (Merz et al. (2015); Monnier et al. (2014)). However, to understand the complex internal structures and its origin of a rock glacier, the whole landform continuum has to be considered. The use of GPR to investigate a whole proglacial ice-debris complex is relatively new and unknown but proved to be a suitable method (cf. Monnier et al. (2014)).

### 6.1 Structure of Landforms

Based on the GPR profiles a proglacial ice-debris complex was investigated and different landforms could clearly be distinguished. Glacier, moraines, glacio-fluvial plain and rock glacier features could be detected and showed distinct internal structures (see figure 36). The distinction between glacier and adjacent moraine was most pronounced and more difficult between periglacial landforms.

The distinction of geomorphological landform features could be also made on a landform assemblage in the Andes, where the distinction between debris-covered glacier and moraine was most pronounced and more difficult between moraine and rock glacier features (Monnier et al., 2014). Thus, it can be hypothesised, that the internal structures of landforms of the same geomorphological process domain are more difficult to distinguish.

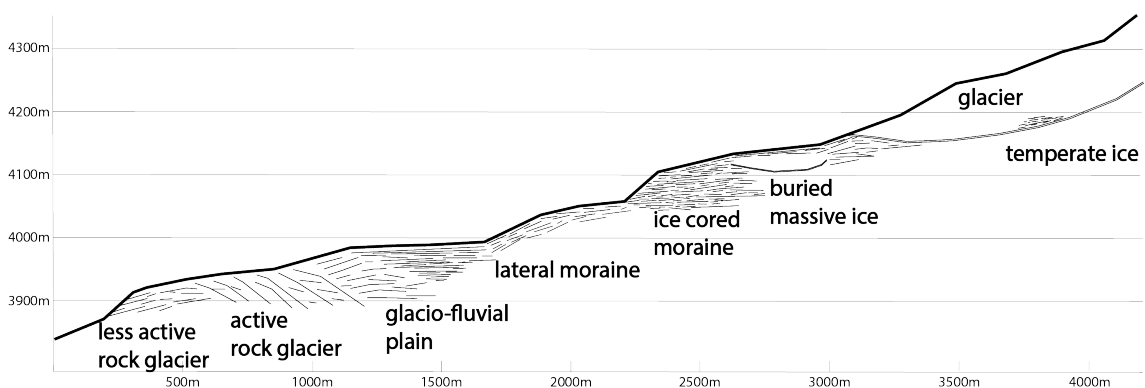


Figure 36: Internal structures of the investigated ice-debris complex (own figure)

### **Glacier**

GPR profiles on the glacier showed almost no internal reflections but a distinct bedrock reflector. The homogeneity of glacier ice and its very low electrical conductivity lead to an almost reflection free stratigraphy. A more chaotic pattern close to the bedrock reflector was interpreted as temperate ice (see figure 24). Similar stratigraphy was also found on other glaciers and interpreted as temperate ice (cf. Irvine-Fynn et al. (2006)). The change in GPR pattern is most likely due to a changing dielectric constant, caused by intracrystalline liquid water. The investigated glacier is therefore interpreted as a polythermal glacier. Glaciers in the Central Tien Shan are considered to be of polythermal or even cold nature (Osmonov et al., 2013; Shi and Liu, 2000).

### **Moraines**

In the glacier ice-debris complex, the lateral and medial moraines are adjacent to the glacier. The moraines are thus the first landform of the periglacial process domain. GPR profiles taken on the moraines, showed a completely different pattern than on the glacier. The stratigraphy was much more heterogeneous with a chaotic pattern, surface parallel and dipping reflectors. Similar heterogeneous stratigraphy was also found by Langston et al. (2011) in a proglacial moraine in the Canadian Rocky Mountains.

An exposure on the lateral moraine of Gornergletscher allowed field evidence to GPR measurements (cf. Lukas and Sass (2011)). The sub parallel GPR reflectors were interpreted as alternating clast- and matrix-supported stratified diamicts and intercalated sorted debris units (Lukas and Sass, 2011). A similar composition could be expected in the medial moraine. The investigated lateral moraine however showed clear indicators for buried ice. Especially in the upper part distinct reflectors and the stratigraphy varied from the stratigraphy in the medial moraine. In the lower part of the lateral moraine (see figure 29) the pattern was more similar to the pattern found in the medial moraine.

### **Rock Glacier**

The stratigraphy of the rock glacier as a whole landform, was characterised by mostly surface parallel, slightly undulating or dipping reflector bands. Surface parallel reflectors were more pronounced in the longitudinal profiles. Transverse profiles showed a more undulating stratigraphy. Even undulating or dipping reflectors, consisted of layered and mostly parallel reflection bands. Thus, the internal structure of the rock glacier, was mainly dominated by a layered stratigraphy.

A surface parallel stratigraphy, is common in rock glaciers. A similar stratigraphy was

found in rock glaciers in Svalbard (Berthling et al., 2000; Farbrot et al., 2005; Isaksen et al., 2000), Colorado (Degenhardt, 2009), Antarctic (Fukui et al., 2008) and in the Alps (Maurer and Hauck, 2007; Monnier et al., 2013). The layered stratigraphy is interpreted as alternating ice-rich and ice-poor layers. Alternation of ice-rich and ice-poor layers were also found in boreholes. Monnier et al. (2013) found vertical alternation of ice-rich and ice-poor layers with an extracted ice content of 15-30%. Vonder Mühl and Holub (1992) found a massive ice layer, followed by debris layers in Murtel-Corvatsch rock glacier and Fukui et al. (2008) found only very thin debris layers alternating with thick layers consisting of bubbly ice.

The layered stratigraphy could also be explained by the two-layer model. The model explains rock glaciers to be built up of an outer layer consisting of blocky materials and an inner layer consisting of a fine-grained ice-debris matrix (Wahrhaftig and Cox, 1959; Haeberli et al., 2006). Since strong air and ground wave arrivals were apparent as high-amplitude reflectors in the upper 6-8m, the active layer was hard to detect. Therefore, no distinct reflector was visible marking the inner and the outer layer. Hence, the existing profiles are interpreted to only show the ice-rich inner layer.

The longitudinal profile RG-L1 (see figure 32) showed two distinct patterns. A weak surface parallel stratigraphy and a more chaotic stratigraphy in the upper part. These two patterns were interpreted as a more active rock glacier, where the stratigraphy was more chaotic and a less active rock glacier, where the stratigraphy was more surface parallel. The prominent slanting layers could describe internal shear horizons and are likely related to the concave ridges at the surface. The shear horizons were slanting up to the surface in creep direction. Reflectors were slanting because the creeping rate is higher, closer to the surface. Arenson et al. (2002) state, that in degrading permafrost and due to enhanced ice melt, creep rate increases towards the surface. Hence, slanting layers are indicating enhanced creep towards the surface and could also be an indicator for degrading permafrost.

### **Glacio-Fluvial Plain**

The stratigraphy of the glacio-fluvial plain was more chaotic in the longitudinal profile and surface parallel in the transverse profile. The GPR stratigraphy was interpreted as the result of sedimentation of glacio-fluvial-deposits. However, glacio-fluvial sediments are notoriously difficult for GPR, due to the high clay and water content (Woodward and Burke, 2007).

## 6.2 Genesis of the Landform Complex

The analysis of the geomorphological characteristics of the investigated ice-debris complex showed a polygenetic origin with different landform sequences. The landform sequences showed a transition from glacial to periglacial landforms. Similar geomorphological transitions were also found in the Andes (Monnier et al., 2014) and in the Northern Tien Shan (Gorbunov et al., 1992).

In the geomorphological map, the landform transition was most pronounced, where rock-falls from steep rock slopes have lead to debris input. The large glacier part, without supraglacial debris, does not show a distinct transition. Thus, the transition from a glacial to a periglacial landform is mainly depending on the availability of debris and is therefore the result of glacier and permafrost related deposits (cf. Etzelmuller and Hagen (2005); Haeberli (2005*a*)).

The landform transition is not only geomorphologically but also structurally visible. With ongoing glacier to rock glacier transition, the layered stratigraphy is becoming more pronounced. The layered stratigraphy is the result of rock wall erosion as well as snowfall and avalanches, which have created an alternating deposition of ice or snow and debris layers on the glacier. The layered stratigraphy is thus an indicator, that debris and ice in the ice-debris complex are originating from the adjacent rock walls and helps to understand the creep and deformation behaviour of the ice-debris complex.

To better understand the genesis of ice-debris complexes, it is important to understand under what circumstances ice-debris complexes occur. The spatial distribution of the inventoried rock glaciers (see section 5.1) provide information on favourable conditions of rock glaciers. The inventoried rock glaciers were often a part of an ice-debris complex. Hence, the inventoried rock glaciers can serve as a proxy for ice-debris complexes.

In the Ak-Shiirak massif, the inventoried rock glaciers are found most prominently on south-to-eastern slopes and are situated in continuous (or less in discontinuous) permafrost (rough estimation based on the permafrost zonation index by Gruber (2012)). The investigated ice-debris complex has a southern aspect and is situated in continuous permafrost. The occurrence of permafrost can be confirmed by ground temperature measurements around the investigated ice-debris complex. The occurrence of permafrost is required for rock glaciers to occur (Barsch, 1996; Haeberli, 1985; Wahrhaftig and Cox, 1959) and is thus also a prerequisite for similar ice-debris complexes to exist. The dominant south-facing aspect is likely resulting in a higher solar radiation and less winter precipitation,

due to the lee side of the Ak-Shiirak massif.

Beside the south-facing aspect and the occurrence of permafrost, the ice-debris complexes in the Ak-Shiirak massif are characterised to appear below glaciers surrounded by steep and heavily eroded rock walls. In the Northern Tien Shan, the distribution and characteristics of large rock glaciers is hypothesized to relate to the same conditions. Beside the location below glaciers and the topographic characteristics, intensive weathering and rock avalanches triggered by seismic activity are hypothesized (Bolch and Gorbunov, 2014).

The investigated ice-debris complex in the Ak-Shiirak range has probably formed during glacier advances in the late Pleistocene-Holocene and during the Little Ice Age (LIA). In the Kyrgyz Tien Shan, several glaciation maxima resulted in multiple moraines and drifts from late Quarternary glaciations (Koppes et al., 2008). Radiocarbon dating from buried soils in a lateral moraine (Narama and Okuno, 2006) and ice-core boreholes on an ice cap (Takeuchi et al., 2014) suggest that the Tien Shan region was considerably warmer at the end of the Pleistocene than at present. With glacier advances, the extent and altitudinal range of permafrost has changed as well several times during the Holocene (Gorbunov, 1996). The massive buried ice in the upper lateral moraine could be an indicator for a readvance of the glacier, followed by the incorporation of glacier ice in the ice-debris complex (Monnier and Kinnard, 2015*a*).

The complex appearance and the large rock glacier tongue, lead to the assumption that the investigated ice-debris complex has formed during former glacier advances.

### 6.3 Ice Content

Ice is ubiquitous in a glacial-periglacial environment. The investigated ice-debris complex not only consist to a major part of ice, but was also shaped under the influence of ice. Geomorphological features like ice cliffs, ridges and furrows as well as thermocarst are distinct indicators for the presence of buried ice.

To estimate the ice content and distribution of subsurface ice in the ice-debris complex, GPR measurements were taken. GPR profiles showed distinct indicators of ice like the almost reflection free glacier ice, delimited by the glacier bed, or buried ice lenses in the ice-cored moraine. The ice content is more difficult to estimate, where an ice-debris matrix is apparent, or a layered stratigraphy of alternating ice and debris layers could be found. In order to estimate the ice content of the different landforms, an attempt in measuring the subsurface velocities by using the hyperbolic fitting method, was applied. The hyperbola fitting method is a rough approximation only. The subsurface velocity is depending

on the ice, air and liquid water content of the subsurface, as well as from the electromagnetic properties of the subsurface material. Subsurface velocities above 0.15m/ns can be interpreted as ice or dry sand, whereas subsurface velocities below 0.06m/ns can be interpreted as saturated sand, or clay (after Davis and Annan (1989)). Thus, the result of hyperbola fitting has to be interpreted as a general subsurface parameter and not from the ice content only. This method was already used in other GPR studies on rock glaciers (cf. Florentine et al. (2014); Fukui et al. (2008); Monnier et al. (2013)).

The results of the hyperbolic fitting method are summarised in table 10. The subsurface velocity was highest on the medial and on the lateral moraine and were lowest on the rock glacier and on the glacio-fluvial plain. The moraines could thus be interpreted to consist of more blocky and dry material containing ice lenses or air pockets, whereas the rock glacier and the glacio-fluvial plain could be interpreted to consist of more fine-grained and wet material, probably containing less ice. However, the estimated velocities are based on GPR measurements, which represent a two-dimensional model along a transect. Thus, a statement about the subsurface properties of a whole landform, only based on a few transects is not very significant, since the subsurface properties of such landforms can be very heterogeneous. Furthermore, two different GPR devices were used, with an unshielded antenna. This would mean, that prominent hyperbolic reflectors used for curve fitting, might also originate from aboveground.

Considering the methodological uncertainties, a quantitative estimation of the ice content was not possible. Nevertheless, the hyperbola fitting method can help with the spatial distribution of the subsurface ice. In the transverse profile MM-T1 on the medial moraine (see figure 28) the highest velocities (0.15-0.16m/ns) were measured close to the surface, which could indicate, the ice-rich ice-debris matrix to occur closer to the surface. On the longitudinal profile RG-L1 on the rock glacier (see figure 32), the less active and the more active part could be identified. The less active rock glacier part, probably containing less subsurface ice, showed lower subsurface velocities, compared to the upper, more active rock glacier part.

Another possibility to estimate the ice content of periglacial landforms, is to use geomorphological characteristics. Janke et al. (2015) developed a system do classify debris-covered glaciers and rock glaciers based on satellite imagery. Debris-covered glaciers and rock glaciers are understood to be part of a landform continuum, as they degrade from valley glaciers, to debris-covered glaciers and eventually rock glaciers (Giardino and Vitek, 1988) in (Janke et al. (2015)). The classification scheme consists of six classes. The classification system is linked to field observations and measurements of the ice content. Thus,

Table 10: Subsurface velocities of GPR profiles in [m/ns]

Landform	Number	Mean	Std deviation	Minimum	Maximum
MM-L1	5	0.104	0.055	0.07	0.2
MM-L2	3	0.13	0.36	0.09	0.16
MM-T1	11	0.128	0.022	0.1	0.16
<b>Medial moraine</b>		<b>0.121</b>			
LM-L1	39	0.135	0.02	0.08	0.16
LM-T1	6	0.11	0.038	0.065	0.17
<b>Lateral moraine</b>		<b>0.123</b>			
RG-L1	29	0.11	0.029	0.06	0.155
RG-L2	7	0.093	0.03	0.05	0.13
RG-T1	8	0.1	0.034	0.07	0.17
RG-T2	17	0.12	0.031	0.07	0.19
RG-T3	16	0.094	0.024	0.06	0.14
<b>Rock glacier</b>		<b>0.099</b>			
GF-L1	6	0.096	0.022	0.06	0.12
GF-T1	9	0.1	0.03	0.06	0.15
<b>Glacio-fluvial plain</b>		<b>0.102</b>			

the ice content could be estimated using the geomorphological features only.

The classification system could partly be applied to the investigated ice-debris complex. The transition of the glacier with supraglacial debris (*class 2 - fully covered*, ice content: 65-85%) to the ice-cored moraine (*class 3 - buried glacier*, ice content: 45-65%) at the northern margin of the ice-debris complex could be classified. The rock glacier tongue was classified as *class 4 - proper rock glaciers* with an estimated ice content of 25-45%.

Clear distinguishable landform features can be classified using this approach. However with more complex landform assemblages, classification will become more difficult. Snowfall, available debris and temperature that affect glacial and periglacial processes make it difficult to assign landforms to a single class (Janke et al., 2015).

Using either method, it is assumed that the ice content in the landform continuum will decrease with the transition from a glacier to a rock glacier. A significant assignment of ice proportion to the different landform elements of this ice-debris complex is not possible without accurate on-site measurements.

#### 6.4 Hydrological Significance

With ongoing glacier recession, it is expected that ice-rich permafrost bodies compensate at least partly the recession in snow and glacier melt derived runoff (Bolch and Marchenko, 2009; Sorg et al., 2012). Therefore, an estimation of the regional storage and release potential of the ice-rich permafrost was done. According to Barsch (1992), rock glaciers are the visible expression of creeping ice-supersaturated mountain permafrost. Thus, the inventoried rock glaciers were used to estimate the hydrological significance. The hydrological significance of rock glaciers is primarily related to the ice-debris matrix, which functions as an aquifer, having recharge, discharge, through-flow and storage characteristics (Burger et al., 1999). To estimate the hydrological significance, the ice storage potential of rock glaciers was compared to the storage potential of glaciers. Hence a ratio of rock glacier to glacier ice volume (see section 5.1.3) was calculated and compared to other regions (see table 11).

In the semi-arid Andes (3:1)(Azócar and Brenning, 2010), in the arid Andes (1:2.7)(Azócar and Brenning, 2010) and in the Andes of Santiago (1:7)(Brenning, 2005), the hydrological significance is expected to be higher than in the Central Tien Shan (1:23)(Bolch and Marchenko, 2009), where glaciers hold 23 times more ice volume than rock glaciers. In the Swiss Alps (1:83)(Brenning, 2005), the hydrological significance is expected to be much lower. In the Northern Tien Shan, the hydrological significance is only slightly lower than in the Central Tien Shan.

A higher rock glacier to glacier ice volume ratio does not necessarily mean that less ice is stored in rock glaciers, but that the glacierized area is bigger. Therefore, the ice volume ratio is strongly depending on the occurrence, size and spatial distribution of glaciers. Considering the geographical latitude (see table 11), the hydrological significance of rock glaciers is increasing with a lower geographical latitude. This correlation can be explained with a higher solar radiation, with lower geographical latitude, resulting in enhanced glacier melt and a good insulation of rock glacier ice, due to a debris layer.

However, the manual mapping of rock glacier bodies only using remote sensing data is rather inaccurate. Especially the delimitation of the upper rock glacier end, which often ends as a transition into a scree slope, is difficult (Krainer and Ribis, 2012). The rock glacier inventory does not distinguish between active and inactive rock glaciers. The ice content of inactive rock glaciers is thus calculated the same way as active rock glaciers, although in the investigated rock glacier tongue, clear GPR patterns show differences between active and less active parts. The estimated ice content of rock glaciers and hence

the rock glacier to glacier ice volume ratio is thus a rough guess. In a similar study, uncertainties were estimated to be in the order of -50% -100% (Azócar and Brenning, 2010). In this study, the uncertainty is expected to be in the same range.

Table 11: Hydrological significance of rock glaciers as water stores worldwide

<b>Location</b>	<b>Latitude</b>	<b>Ratio of rock glacier to glacier ice volumes</b>	<b>Source</b>
Semi-arid Andes(Chile)	29°-32°S	3:1	Azócar and Brenning (2010)
Arid Andes(Chile)	27°-29°S	1:2.7	Azócar and Brenning (2010)
Andes of Santiago(Chile)	32°-34°S	1:7	Brenning (2005)
Central Tien Shan	41°N	1:23	This study
Northern Tien Shan (Kazakhstan/Kyrgyzstan)	42°-44°N	1:31	Bolch and Marchenko (2009)
Swiss Alps	45°-47°N	1:83	Brenning (2005), based on data from Barsch (1996)

This estimation focussed on the rock glaciers only. For a more holistic estimation of the hydrological significance, the whole periglacial area, especially the ice-debris complexes have to be considered. GPR measurements showed distinct patterns of ice-rich permafrost and buried massive ice in the morainic parts of the ice-debris complex. On an ice-debris complex in the southern part of the Ak-Shiirak massif, point GPR measurements in 2012 revealed massif buried ice. Ice depths of up to 300m were measured (cf. Bolch et al. (2015)). In the Northern Tien Shan, permafrost related periglacial landforms such as lacustrine and alluvial sediments, moraines, rock glaciers and other blocky materials are expected to contain up to 80% of ice (Bolch and Marchenko, 2009). Hence, the estimation of the total water stored in ice-rich permafrost and permafrost related ice-debris complexes is difficult. With ongoing global warming and associated glacier melt, ice stored in permafrost related landforms such as ice-debris complexes, will become an increasingly important fresh water source (Bolch and Marchenko, 2009).



## 7 Conclusion and Outlook

In this thesis, internal structures and geomorphological characteristics of an ice-debris complex were investigated and described, in order to understand the origin of the landform complex and to get information about its ice content. The hydrological significance of such landforms was addressed, creating a rock glacier inventory and estimating a rock glacier to glacier ice volume ratio.

More than 20km of GPR profiles were taken to investigate internal structures. The GPR profiles were mostly characterised by a surface parallel layered stratigraphy. It is assumed, that the layered stratigraphy is the result of the alternating deposition of rock and ice avalanches. Beside the layered stratigraphy, the profiles indicated bedrock, buried massive ice lenses, distinct reflection patterns and internal shear horizons. Based on the GPR profiles, the ice-debris complex was divided into five landform classes: glacier, medial moraine, lateral moraine, rock glacier tongue and glacio-fluvial plain. The assigned landform classes fitted well with the developed geomorphological map. In the geomorphological map, the glacial (40%), gravitational (32%) and periglacial (26%) process domains were the most dominant.

The detection of the ice content using GPR was more difficult. Unless buried massive ice, with a distinct boundary between ice and adjacent debris is present, the quantification of the ice content solely using GPR measurements is hardly possible. Additional CMP or geoelectrical measurements could improve the interpretation of GPR profiles and hence the detection of buried ice. The use of the curve fitting method to identify the subsurface properties, proved to be only partly suitable, as only a limited amount of suitable hyperbolas were apparent and thus too high uncertainties occurred. When applying GPR, one should know what subsurface properties are to be expected.

The use of mainly satellite imageries to develop a geomorphological map, was successful. GPR measurements combined with geomorphological information helped to better understand the origin and transition of this ice-debris complex. The ice-debris complex could be structurally as well as geomorphologically characterized and is understood as an intermediate landform shaped by the interaction of glacial and periglacial process domains.

The hydrological significance of ice-rich permafrost related landforms was addressed by creating a rock glacier inventory for the Ak-Shiirak massif. A total of 63 rock glaciers were mapped. About 70% of the rock glaciers had a southern to eastern slope aspect. The ice content of the inventoried rock glaciers was estimated to be  $0.165\text{km}^3$ . Compared

to adjacent glacier ice, a rock glacier to glacier ice volume ratio of 1:23 was calculated. The hydrological significance of the ice stored in rock glaciers is in the same range as in the Northern Tien Shan, but less significant compared to the ice stored in rock glaciers in the Dry Andes. The major drawback of a rock glacier inventory is that only a part of the periglacial environment was considered for the estimation of the hydrological significance; ice-cored moraines or other permafrost related landforms were ignored.

With ongoing global warming, glaciers will further retreat and ice-rich permafrost will degrade. Water stored in ice-rich permafrost and permafrost related landforms will become a more important source for fresh water. The glacier recession will leave moraine depositions, dead ice bodies or ice-rich permafrost and will lead to an increased proglacial environment. These circumstances offer favourable conditions for ice-debris complexes to develop. It is thus likely, that the transformation of glaciers to ice-debris complexes or rock glaciers will increase with ongoing global warming (cf. Monnier and Kinnard (2015*b*)). Considering the increasing hydrological importance of permafrost related landforms, especially in a region where fresh water is scarce, a more detailed quantification of the water storage is desirable. Insights on the internal characteristics, the ice content and the development of ice-debris complexes remains unsatisfactory. Further research and geophysical investigations are recommended.

---

## References

- Aizen, V. B., Aizen, E. M. and Melack, J. M. (1995), Climate, Snow Cover, Glaciers and Runoff in the Tien Shan, Central Asia, *Water Resources Bulletin* 31(6), 1113–1129.
- Aizen, V. B., Aizen, E. M., Melack, J. M. and Dozier, J. (1997), Climatic and Hydrologic Changes in the Tien Shan , Central Asia, *Journal of Climate* 10, 1393–1404.
- Aizen, V. B., Kuzmichenok, V. A., Surazakov, A. B. and Aizen, E. M. (2007), Glacier changes in the Tien Shan as determined from topographic and remotely sensed data, *Global and Planetary Change* 56, 328–340.
- Annan, A. P. (1999a), Ground Penetrating Radar Workshop Notes, *Sensors and Software Inc.* .
- Annan, A. P. (1999b), Practical Processing of GPR Data, *Sensors and Software Inc.* (905).
- Arcone, S. (2002), Stratigraphic profiling with ground-penetrating radar in permafrost: A review of possible analogs for Mars, *Journal of Geophysical Research* 107(E11), 5108.
- Arenson, L., Hoelzle, M. and Springman, S. (2002), Borehole deformation measurements and internal structure of some rock glaciers in Switzerland, *Permafrost and Periglacial Processes* 13(2), 117–135.
- Azócar, G. F. and Brenning, A. (2010), Hydrological and geomorphological significance of rock glaciers in the dry Andes, Chile (27-33S), *Permafrost and Periglacial Processes* 21(1), 42–53.
- Barnett, T. P., Adam, J. C. and Lettenmaier, D. P. (2005), Potential impacts of a warming climate on water availability in snow-dominated regions., *Nature* 438(November), 303–309.
- Barsch, D. (1977), Nature and importance of mass-wasting by rock glaciers in alpine permafrost environments, *Earth Surface Processes* 2, 231–245.
- Barsch, D. (1992), Permafrost Creep and Rockglaciers, *Permafrost and Periglacial Processes* 3, 175–188.
- Barsch, D. (1996), *Rockglaciers - Indicators for the Present and Former Geoecology in High Mountain Environments*, Springer.

## REFERENCES

---

- Benn, D. I. (2009), Glaciofluvial Sediments, *in* V. Gornitz, ed., 'Encyclopedia of Paleoclimatology and Ancient Environments', Springer, p. 394.
- Benn, D. I. and Evans, D. J. A. (1998), *Glaciers and Glaciation*, Hodder Education.
- Beres, M., Huggenberger, P., Green, A. G. and Horstmeyer, H. (1999), Using two- and three-dimensional georadar methods to characterize glaciofluvial architecture, *Sedimentary Geology* 129(1-2), 1–24.
- Bernauer, T. and Siegfried, T. (2012), Climate change and international water conflict in Central Asia, *Journal of Peace Research* 49, 227–239.
- Berthling, I. (2011), Beyond confusion: Rock glaciers as cryo-conditioned landforms, *Geomorphology* 131(3-4), 98–106.
- Berthling, I., Etzelmüller, B., Isaksen, K. and Sollid, J. L. (2000), Rock glaciers on Prins Karls Forland. II: GPR soundings and the development of internal structures, *Permafrost and Periglacial Processes* 11(4), 357–369.
- Berthling, I. and Melvold, K. (2008), Ground-penetrating radar, *in* C. Hauck and C. Kneisel, eds, 'Applied Geophysics in Periglacial Environment', Cambridge University Press, pp. 81–97.
- Böhner, J. (2006), General climatic controls and topoclimatic variations in Central and High Asia, *Boreas*. 35(2005), 279–295.
- Bolch, T. (2004), Using ASTER and SRTM DEMs for studying Glaciers and Rockglaciers in Northern Tien Shan, *Proceedings Part I of the Conference Teoreticheskiye i Prikladnyye Problemy geografii na rubeschje Stoletij* (June), 254–258.
- Bolch, T. (2007), Climate change and glacier retreat in northern Tien Shan (Kazakhstan/Kyrgyzstan) using remote sensing data, *Global and Planetary Change* 56(1-2), 1–12.
- Bolch, T. and Gorbunov, A. P. (2014), Characteristics and Origin of Rock Glaciers in Northern Tien Shan (Kazakhstan/Kyrgyzstan), *Permafrost and Periglacial Processes* 25(4), 320–332.
- Bolch, T., Kulkarni, a., Kaab, a., Huggel, C., Paul, F., Cogley, J. G., Frey, H., Kargel, J. S., Fujita, K., Scheel, M., Bajracharya, S. and Stoffel, M. (2012), The State and Fate of Himalayan Glaciers, *Science* 336, 310–314.

- Bolch, T., Kutuzov, S., Rohrbach, N., Fischer, A. and Osmonov, A. (2015), Geomorphology and Ice Content of Glacier - Rock Glacier - Moraine Complexes in Ak-Shiirak Range ( Inner Tien Shan , Kyrgyzstan ), *Geophysical Research Abstracts* 17(EGU2015-10743-2).
- Bolch, T. and Marchenko, S. (2009), Significance of glaciers , rockglaciers , and ice-rich permafrost in the Northern Tien Shan as water towers under climate change conditions, *Proceedings of the Workshop "Assessment of Snow-Glacier and Water Resources in Asia"* pp. 28–30.
- Brardinoni, F. and Hassan, M. A. (2006), Glacial erosion, evolution of river long profiles, and the organization of process domains in mountain drainage basins of coastal British Columbia, *Journal of Geophysical Research: Earth Surface* 111, 1–12.
- Brenning, A. (2005), Climatic and geomorphological controls of rock glaciers in the Andes of Central Chile: Combining statistical modelling and field mapping, *Dissertation* p. 153.
- Brenning, A. (2009), Benchmarking classifiers to optimally integrate terrain analysis and multispectral remote sensing in automatic rock glacier detection, *Remote Sensing of Environment* 113(1), 239–247.
- Burger, K., Degenhardt, J. and Giardino, J. (1999), Engineering geomorphology of rock glaciers, *Geomorphology* 31(1-4), 93–132.
- Burger, R., Sheehan, A. F. and Jones, C. H. (2006), *Introduction to Applied Geophysics - Exploring the Shallow Subsurface*, W.W. Norton & Company Inc.
- Chen, D., Huan, C. and Li, Y. (2004), An integrated method of statistical method and hough transform for GPR targets detection and location, *Acta Electronica Sinica* 32(9), 1468–1471.
- Curtaz, M., Vagliasindi, M., Letey, S., Morra, U. and Pogliotti, P. (2011), A new rock glaciers inventory in the North-Western Alps, *Geophysical Research Abstracts* 13.
- Daniels, D. J. (1996), *Surface-Penetrating Radar*, The Institution of Electrical Engineers.
- Daniels, D. J. (2004), *Ground Penetrating Radar*, The Institution of Electrical Engineers.
- Davis, J. L. and Annan, A. P. (1989), Ground-Penetrating Radar for High-Resolution Mapping of Soil and Rock Stratigraphy, pp. 531–551.

## REFERENCES

---

- Degenhardt, J. J. (2009), Development of tongue-shaped and multilobate rock glaciers in alpine environments - Interpretations from ground penetrating radar surveys, *Geomorphology* 109(3-4), 94–107.
- Demek, J. (1976), *Handbuch der geomorphologischen Detailkartierung*, Hirt Verlag.
- Demel, W. and Hauenstein, P. (2005), Cartography of habitats by Colour Infrared Aerial Images - Guidelines for Delimitation and Interpretation, *Alpine Habitat Diversity - HABITALP* pp. 1–28.
- Dikikh, A. N. (1993), Lednikovyi stok rek Tyan-Shanya i ego rol' v formirovanii obshego stoka (Glacier runoff in the rivers of Tien Shan and its role in total runoff formation), *Materialy Glaciologicheskikh Issledovaniy* 77, 41–50.
- Dyurgerov, M., Kunakhovitch, M. and Mikhaleiko, V. (1993), Mass balance monitoring of the three Tien Shan glaciers [in Russian], *Data of Glaciological Studies* 77, 79–86.
- Esper Angillieri, M. Y. (2009), A preliminary inventory of rock glaciers at 30S latitude, Cordillera Frontal of San Juan, Argentina, *Quaternary International* 195, 151–157.
- Etzelmüller, B. and Hagen, J. O. (2005), Glacier-permafrost interaction in Arctic and alpine mountain environments with examples from southern Norway and Svalbard, *Geological Society, London, Special Publications* 242, 11–27.
- Evans, D. J. A. (1993), High-latitude rock glaciers: A case study of forms and processes in the Canadian arctic, *Permafrost and Periglacial Processes* 4, 17–35.
- Falaschi, D., Castro, M., Masiokas, M., Tadono, T. and Ahumada, A. L. (2014), Rock Glacier Inventory of the Valles Calchaquíes Region, Salta, Argentina, Derived from ALOS Data, *Permafrost and Periglacial Processes* 25, 69–75.
- Farbrot, H., Isaksen, K., Eiken, T., Kääh, A. and Sollid, J. L. (2005), Composition and internal structures of a rock glacier on the strandflat of western Spitsbergen, Svalbard, *Norsk Geografisk Tidsskrift - Norwegian Journal of Geography* 59(2), 139–148.
- Farr, T., Rosen, P., Caro, E., Crippen, R., Duren, R., Hensley, S., Kobrick, M., Paller, M., Rodriguez, E., Roth, L., Seal, D., Shaffer, S., Shimada, J., Umland, J., Werner, M., Oskin, M., Burbank, D. and Alsdorf, D. (2007), The Shuttle Radar Topography Mission, *Reviews of Geophysics* pp. 1–33.

- Florentine, C., Skidmore, M., Speece, M., Link, C. and Shaw, C. . (2014), Geophysical analysis of transverse ridges and internal structure at Lone Peak Rock Glacier, Big Sky, Montana, USA, *Journal of Glaciology* 60(221), 453–462.
- Frauenfelder, R., Haeberli, W. and Hoelzle, M. (2003), Rockglacier occurrence and related terrain parameters in a study area of the Eastern Swiss Alps, *8th International Conference on Permafrost* pp. 253–258.
- French, H. M. (2007), *The Periglacial Environment*, John Wiley & Sons.
- Fukui, K., Sone, T., Strelin, J. A., Torielli, C. A., Mori, J. and Fujii, Y. (2008), Dynamics and GPR stratigraphy of a polar rock glacier on James Ross Island, Antarctic Peninsula, *Journal of Glaciology* 54(186), 445–451.
- Giardino, J. R. and Vitek, J. D. (1988), The significance of rock glaciers in the glacial-periglacial landscape continuum, *Journal of Quaternary Science* 3(1), 97–103.
- Giese, E. (2004), Climate Data from Tien Shan meteo station kindly provided.
- Giese, E. and Mossig, I. (2004), Klimawandel in Zentralasien, *Diskussionsbeiträge // Zentrum für internationale Entwicklungs- und Umweltforschung* 17.
- Gorbunov, A. P. (1996), Monitoring the Evolution of Permafrost in the Tien Shan, *Permafrost and Periglacial Processes* 7, 297–298.
- Gorbunov, A. P. (1998), Rock glaciers, Zailiysiky Range, Kungei Ranges, Tienshan, Kazakhstan, in ‘International Permafrost Association, Data and Information Working Group, comp. Cirumpolar Active-Layer Permafrost System (CAPS)’.
- Gorbunov, A. P., Seversky, E. V. and Titkov, S. N. (1996), Geocriologicheskie Usloviya Tyan-Shanya i Pamira (Geocryological Conditions of the Tien Shan and Pamir), *Permafrost Institute publishers* .
- Gorbunov, A. P., Titkov, S. N. and Polyakov, V. G. (1992), Dynamics of Rock Glaciers of the Northern Tien Shan and the Djungar Ala Tau , Kazakhstan, *Permafrost and Periglacial Processes* 3, 29–39.
- Gruber, S. (2012), Derivation and analysis of a high-resolution estimate of global permafrost zonation, *The Cryosphere* 6(1), 221–233.
- Guglielmin, M. and Smiraglia, C. (1998), The rock glacier inventory of the Italian Alps, (55), 375–382.

## REFERENCES

---

- Gustavsson, M., Kolstrup, E. and Seijmonsbergen, A. C. (2006), A new symbol-and-GIS based detailed geomorphological mapping system: Renewal of a scientific discipline for understanding landscape development, *Geomorphology* 77, 90–111.
- Haeberli, W. (1985), Creep of Mountain Permafrost: Internal Structure and Flow of Alpine Rock Glaciers, *Mitteilungen der Versuchsanstalt für Wasserbau, Hydrologie und Glaziologie* (77).
- Haeberli, W. (2005a), Investigating glacier-permafrost relationships in high-mountain areas: historical background, selected examples and research needs, *Geological Society, London, Special Publications* 242, 29–37.
- Haeberli, W. (2005b), Mountain Glaciers in Global Climate-related Observing Systems, in U. Huber, M. Reasoner and H. Bugmann, eds, ‘Global Change and Mountain Regions’, pp. 169–175.
- Haeberli, W. and Beniston, M. (1998), Climate Change and Its Impacts on Glaciers and Permafrost in the Alps, *Ambio* 27(4), 258–265.
- Haeberli, W., Hallet, B., Arenson, L., Elconin, R., Humlum, O. and Ka, A. (2006), Permafrost Creep and Rock Glacier Dynamics, *Permafrost and Periglacial Processes* 214, 189–214.
- Harris, C., Arenson, L. U., Christiansen, H. H., Etzelmüller, B., Frauenfelder, R., Gruber, S., Haeberli, W., Hauck, C., Hölzle, M., Humlum, O., Isaksen, K., Kääh, A., Kern-Lütschg, M. a., Lehning, M., Matsuoka, N., Murton, J. B., Nötzli, J., Phillips, M., Ross, N., Seppälä, M., Springman, S. M. and Vonder Mühl, D. (2009), Permafrost and climate in Europe: Monitoring and modelling thermal, geomorphological and geotechnical responses, *Earth-Science Reviews* 92(3-4), 117–171.
- Hauck, C. and Kneisel, C. (2008), *Applied Geophysics in Periglacial Environments*, Cambridge University Press.
- Hauck, C., Vonder Müll, D. and Maurer, H. (2003), Using DC resistivity tomography to detect and characterize mountain permafrost, *Geophysical Prospecting* 51, 273–284.
- Hausmann, H., Krainer, K., Brückl, E. and Mostler, W. (2007), Internal Structure and Ice Content of Reichenkar Rock Glacier (Stubai Alps, Austria) Assessed by Geophysical Investigations, *Permafrost and Periglacial Processes* 18, 245–258.

- Hausmann, H., Krainer, K., Brückl, E. and Ullrich, C. (2012), Internal structure , ice content and dynamics of Ölgrube and Kaiserberg rock glaciers (Ötztal Alps , Austria) determined from geophysical surveys, *Austrian Journal of Earth Sciences* 1, 12–31.
- Hubbard, B. and Glasser, N. (2005), *Field techniques in glaciology and glacial geomorphology*, John Wiley & Sons.
- Humlum, O. (1996), Origin of rock glaciers: observations from Mellemfjord, Disko Island, central West Greenland, *Permafrost and Periglacial Processes* 7, 361–380.
- Ikeda, A. and Matsuoka, N. (2002), Degradation of talus-derived rock glaciers in the upper engadin, Swiss alps, *Permafrost and Periglacial Processes* 13, 145–161.
- Immerzeel, W. W., van Beek, L. P. H. and Bierkens, M. F. P. (2010), Climate Change Will Affect the Asian Water Towers, *Science* 328, 1382–1385.
- IPCC (2014), Climate Change 2014: Synthesis Report. Contribution of Working Groups I, II and III to the Fifth Assessment Report of the Intergovernmental Panel on Climate Change, Technical report, IPCC, Geneva, Switzerland.
- Irvine-Fynn, T. D. L., Moorman, B. J., Williams, J. L. M. and Walter, F. S. A. (2006), Seasonal changes in ground-penetrating radar signature observed at a polythermal glacier, Bylots Island, Canada, *Earth Surface Processes and Landforms* 31, 892–909.
- Isaksen, K., Odegard, R. S., Eiken, T. and Sollid, J. L. (2000), Composition, Flow and Development of Two Tongue-Shaped Rock Glacier in the Permafrost of Svalbard, *Permafrost and Periglacial Processes* 11, 241–257.
- Ishikawa, M. (2002), Inventory of Rock Glaciers along the Ghunsa Valley, Kanchanjunga Himal, Eastern Nepal, *National Snow and Ice Data Center* .
- Janke, J. R., Bellisario, A. C. and Ferrando, F. A. (2015), Classification of debris-covered glaciers and rock glaciers in the Andes of central Chile, *Geomorphology* 241, 98–121.
- Jol, H. M. (2009), *Ground Penetrating Radar: Theory and Applications*, Elsevier.
- Kääb, A., Chiarle, M., Raup, B. and Schneider, C. (2007), Climate change impacts on mountain glaciers and permafrost, *Global and Planetary Change* 56, 56–58.
- Kellerer-Pirklbauer, A., Lieb, G. K. and Kleinfelchner, H. (2012), A new rock glacier inventory of the eastern European Alps, *Austrian Journal of Earth Sciences* 105/2, 78–93.

## REFERENCES

---

- Khromova, T. (2005), 'GLIMS glacier database'.
- Klimaszewski, M. (1982), Detailed geomorphological maps, *ITC Journal* .
- Koppes, M., Gillespie, A. R., Burke, R. M., Thompson, S. C. and Stone, J. (2008), Late Quaternary glaciation in the Kyrgyz Tien Shan, *Quaternary Science Reviews* 27, 846–866.
- Krainer, K., Mussner, L., Behm, M. and Hausmann, H. (2012), Multi-disciplinary investigation of an active rock glacier in the sella group (Dolomites; Northern Italy), *Austrian Journal of Earth Sciences* 105(2), 48–62.
- Krainer, K. and Ribis, M. (2012), A Rock Glacier Inventory of the Tyrolean Alps (Austria), *Austrian Journal of Earth Sciences* 105/2, 32–47.
- Krysanova, V., Wortmann, M., Bolch, T., Merz, B., Duethmann, D., Walter, J., Huang, S., Tong, J., Buda, S. and Kundzewicz, Z. W. (2014), Analysis of current trends in climate parameters, river discharge and glaciers in the Aksu River basin (Central Asia), *Hydrological Sciences Journal* 60(4), 566–590.
- Kundzewicz, Z. W., Merz, B., Vorogushyn, S., Hartmann, H., Duethmann, D., Wortmann, M., Huang, S., Su, B., Jiang, T. and Krysanova, V. (2014), Analysis of changes in climate and river discharge with focus on seasonal runoff predictability in the Aksu River Basin, *Environmental Earth Sciences* 73(2), 501–516.
- Kutuzov, S., Lavrentiev, I., Vasilenko, E. and Petrakov, D. (2015), Estimation of the greater Caucasus glaciers volume, using radio-echo sounding data and modelling, *Earth's Cryosphere* (1), 78–88.
- Kutuzov, S. and Shahgedanova, M. (2009), Glacier retreat and climatic variability in the eastern TerskeyAlatoo, inner Tien Shan between the middle of the 19th century and beginning of the 21st century, *Global and Planetary Change* 69(1-2), 59–70.
- Kuzmichenok, V. (1989), Tekhnologiya i vozmozhnosty aerotopographicheskogo kartografirovania izmeneniy lednikov (na primere oledeneniya khrebta Akshiiarak)(Methods and opportunities of the aero topographic cartography in context of glaciers changes (e.g. Akshiiarak range glaciers, *Data of Glaciological Studies* 67, 80–87.
- Kuzmichenok, V. (2009), Monitoring of water, snow and glacial resources of Kyrgyzstan, *Assessment of Snow, Glacier and Water Resources in Asia* 8, 84–99.

- 
- Lambiel, C., Maillard, B., Regamey, B., Martin, S., Kummert, M., Schoeneich, P., Ondicol, R. P. and Reynard, E. (2013), The ArcGIS version of the geomorphological mapping legend of the University of Lausanne, *Institute of geography and sustainability, University of Lausanne* .
- Langston, G., Bentley, L. R., Hayashi, M., McClymont, A. and Pidlisecky, A. (2011), Internal structure and hydrological functions of an alpine proglacial moraine, *Hydrological Processes* 25, 2967–2982.
- Leopold, M., Williams, M. W., Caine, N., Völkel, J. and Dethier, D. (2011), Internal structure of the Green Lake 5 rock glacier, Colorado Front Range, USA, *Permafrost and Periglacial Processes* 22(2), 107–119.
- Linsbauer, A., Paul, F. and Haeberli, W. (2012), Modeling glacier thickness distribution and bed topography over entire mountain ranges with glabtop: Application of a fast and robust approach, *Journal of Geophysical Research: Earth Surface* 117, 1–17.
- Liu, Y., Wang, M. and Cai, Q. (2010), The target detection for GPR images based on curve fitting, in ‘3rd International Congress on Image and Signal Processing’, Vol. 2, Ieee, pp. 2876–2879.
- Lukas, S. (2011), Ice-Cored Moraines, in V. P. Singh, P. Singh and U. K. Haritashya, eds, ‘Encyclopedia of Snow, Ice and Glaciers’, Springer, pp. 616–618.
- Lukas, S. and Sass, O. (2011), The formation of Alpine lateral moraines inferred from sedimentology and radar reflection patterns : a case study from Gornergletscher , Switzerland, in I. Martini, H. French and A. Pérez Alberti, eds, ‘Ice-Marginal and Periglacial Processes and Sediments’, The Geological Society of London, pp. 77–92.
- Machguth, H., Eisen, O., Paul, F. and Hoelzle, M. (2006), Strong spatial variability of snow accumulation observed with helicopter-borne GPR on two adjacent Alpine glaciers, *Geophysical Research Letters* 33(13), 1–5.
- Mamatkanov, D. (2006), Water Resources of Kyrgyzstan (in Russian), *National Academy of Science of the Kyrgyz Republic, Institute of Water Problems and Hydropower* .
- Marchenko, S., a.P. Gorbunov and Romanovsky, V. (2007), Permafrost warming in the Tien Shan Mountains, Central Asia, *Global and Planetary Change* 56(3-4), 311–327.

## REFERENCES

---

- Marchenko, S. S. (2001), A model of permafrost formation and occurrences in the intra-continental mountains, *Norsk Geografisk Tidsskrift - Norwegian Journal of Geography* 55(4), 230–234.
- Maurer, H. and Hauck, C. (2007), Instruments and methods: Geophysical imaging of alpine rock glaciers, *Journal of Glaciology* 53(180), 110–120.
- Merz, K., Maurer, H., Buchli, T., Horstmeyer, H., Green, A. G. and Springman, S. M. (2015), Evaluation of Ground-Based and Helicopter Ground-Penetrating Radar Data Acquired Across an Alpine Rock Glacier, *Permafrost and Periglacial Processes* 27(February), 13–27.
- Micklin, P. P. (1988), Desiccation of the aral sea: a water management disaster in the soviet union., *Science* 241, 1170–1176.
- Monnier, S., Camerlynck, C., Rejiba, F., Kinnard, C. and Galibert, P.-Y. (2013), Evidencing a large body of ice in a rock glacier, Vanoise Massif, Northern French Alps, *Geografiska Annaler: Series A, Physical Geography* 95(2), 109–123.
- Monnier, S. and Kinnard, C. (2015a), Internal Structure and Composition of a Rock Glacier in the Dry Andes, Inferred from Ground-penetrating Radar Data and its Artefacts, *Permafrost and Periglacial Processes* .
- Monnier, S. and Kinnard, C. (2015b), Reconsidering the glacier to rock glacier transformation problem: New insights from the central Andes of Chile, *Geomorphology* 238, 47–55.
- Monnier, S., Kinnard, C., Surazakov, A. and Bossy, W. (2014), Geomorphology, internal structure, and successive development of a glacier foreland in the semiarid Chilean Andes (Cerro Tapado, upper Elqui Valley, 3008' S., 6955' W.), *Geomorphology* 207, 126–140.
- Montgomery, D. R. (1999), Process Domains and the River Continuum, *Journal Of The American Water Resources Association* 35, 397–410.
- Moorman, B. J., Robinson, S. D. and Burgess, M. M. (2003), Imaging periglacial conditions with ground-penetrating radar, *Permafrost and Periglacial Processes* 14(4), 319–329.
- Narama, C. and Okuno, M. (2006), Record of glacier variations during the last glacial in the Turkestan range of the Pamir-Alay, Kyrgyz Republic, *Annals of Glaciology* 43, 397–404.
- Neal, A. (2004), Ground-penetrating radar and its use in sedimentology: principles, problems and progress, *Earth-Science Reviews* 66(3-4), 261–330.

- Nyenhuis, M., Hoelzle, M. and Dikau, R. (2005), Rock glacier mapping and permafrost distribution modelling in the Turtmantal, Valais Switzerland, *Zeitschrift für Geomorphologie* 49(3), 275–292.
- Østrem, G. and Arnold, K. (1970), Ice-cored moraines in southern British Columbia and Alberta, Canada, *Geografiska Annaler. Series A. Physical Geography* 52(2), 120–128.
- Odell, D. E., Smith, I. R., Survey, G. and Moorman, B. J. (2009), Detection and characterization of massive ground ice using Ground Penetrating Radar and seismic shothole records, *Proceedings Geo2010 Calgary - 63rd Canadian Geotechnical Conference & 6th Canadian Permafrost Conference* (Figure 1), 1284–1290.
- Oerlemans, J. (2005), Extracting a climate signal from 169 glacier records., *Science* 308(2005), 675–677.
- Osmonov, A., Bolch, T., Xi, C., Kurban, A. and Guo, W. (2013), Glacier characteristics and changes in the Sary-Jaz River Basin (Central Tien Shan, Kyrgyzstan) - 1990-2010, *Remote Sensing Letters* 4(8), 725–734.
- Otto, J. C. and Sass, O. (2006), Comparing geophysical methods for talus slope investigations in the Turtmann valley (Swiss Alps), *Geomorphology* 76(3-4), 257–272.
- Otto, J.-C. and Smith, M. J. (2013), Geomorphological mapping Field Mapping, *British Society for Geomorphology* 6, 1–10.
- Pieczonka, T. and Bolch, T. (2015), Region-wide glacier mass budgets and area changes for the Central Tien Shan between 1975 and 1999 using Hexagon KH-9 imagery, *Global and Planetary Change* 128, 1–13.
- Rangecroft, S., Harrison, S., Anderson, K., Magrath, J., Castel, A. P. and Pacheco, P. (2014), Short Communication A First Rock Glacier Inventory for the Bolivian Andes, *Permafrost and Periglacial Processes* 343, 333–343.
- Raup, B., Racoviteanu, A., Khalsa, S. J. S., Helm, C., Armstrong, R. and Arnaud, Y. (2007), The GLIMS geospatial glacier database: A new tool for studying glacier change, *Global and Planetary Change* 56(1-2), 101–110.
- Sandmeier, K. (2014), ReflexW Version 7.5 - Manual, Technical report.
- Sass, O. (2006), Determination of the internal structure of alpine talus deposits using different geophysical methods (Lechtaler Alps, Austria), *Geomorphology* 80(1-2), 45–58.

## REFERENCES

---

- Schomacker, A. (2011), Moraine, in V. P. Singh, P. Singh and U. K. Haritashya, eds, 'Encyclopedia of Snow, Ice and Glaciers', Springer, pp. 747–756.
- Schrott, L. and Sass, O. (2008), Application of field geophysics in geomorphology: Advances and limitations exemplified by case studies, *Geomorphology* 93, 55–73.
- Scotti, R., Brardinoni, F., Alberti, S., Frattini, P. and Crosta, G. B. (2013), A regional inventory of rock glaciers and protalus ramparts in the central Italian Alps, *Geomorphology* 186, 136–149.
- Shi, Y. and Liu, S. (2000), Estimation on the response of glaciers in China to the global warming in the 21st century, *Chinese Science Bulletin* 45(7), 668–672.
- Siegfried, T., Bernauer, T., Guiennet, R., Sellars, S., Robertson, A. W., Mankin, J., Bauer-Gottwein, P. and Yakovlev, A. (2012), Will climate change exacerbate water stress in Central Asia?, *Climatic Change* 112, 881–899.
- Smith, D. R. (1995), Environmental Security and Shared Water Resources in Post-Soviet Central Asia, *Post-Soviet Geography* 36(6), 351–370.
- Sorg, A., Bolch, T., Stoffel, M., Solomina, O. and Beniston, M. (2012), Climate change impacts on glaciers and runoff in Tien Shan (Central Asia), *Nature Climate Change* 2(10), 725–731.
- Springman, S. M., Arenson, L. U., Yamamoto, Y., Maurer, H., Kos, A., Buchli, T. and Derungs, G. (2012), Multidisciplinary Investigations on Three Rock Glaciers in the Swiss Alps: Legacies and Future Perspectives, *Geografiska Annaler: Series A, Physical Geography* 94(2), 215–243.
- Stolt, R. H. (1978), Migration By Fourier Transform, *Geophysics* 43(I), 23.
- Takahashi, K., Igel, J., Preetz, H. and Kuroda, S. (2007), Basics and Application of Ground- Penetrating Radar as a Tool for Monitoring Irrigation Process, in M. Kumar, ed., 'Problems, Perspectives and Challenges of Agricultural Water Management', InTech.
- Takeuchi, N., Fujita, K., Aizen, V. B., Narama, C., Yokoyama, Y., Okamoto, S., Naoki, K. and Kubota, J. (2014), The disappearance of glaciers in the Tien Shan Mountains in Central Asia at the end of Pleistocene, *Quaternary Science Reviews* 103, 26–33.
- UNEP (2007), Global Outlook for Ice and Snow, *United Nations Environment Programme (UNEP)* .

- USGS (2015), Landsat8, *U.S. Geological Survey* .
- Vasilenko, E. V., Machío, F., Lapazaran, J. J., Navarro, F. J. and Frolovskiy, K. (2011), Instruments and Methods A compact lightweight multipurpose ground-penetrating radar for glaciological applications, *Journal of Glaciology* 57(206), 1113–1118.
- Viviroli, D., Dürr, H. H., Messerli, B., Meybeck, M. and Weingartner, R. (2007), Mountains of the world, water towers for humanity: Typology, mapping, and global significance, *Water Resources Research* 43, 1–13.
- Vonder Mühll, D., Arenson, L. and Springman, S. (2003), Temperature conditions in two Alpine rock glaciers, *8th International Conference on Permafrost, Zurich, Switzerland* pp. 1195–1200.
- Vonder Mühll, D., Hauck, C. and Gubler, H. (2002), Mapping of mountain permafrost using geophysical methods, *Progress in Physical Geography* 26(4), 643–660.
- Vonder Mühll, D. and Holub, P. (1992), Borehole Logging in Alpine Permafrost, Upper Engadin, Swiss Alps, *Permafrost and Periglacial Processes* 3, 125–132.
- Wahrhaftig, C. and Cox, A. (1959), Rock Glaciers In The Alaska Range, *Bulletin of the Geological Society of America* 70(70), 383–436.
- Washburn, A. (1973), *Periglacial processes and environments*, Edward Arnold.
- Whalley, B. W., Hamilton, S. J. and Palmer, C. F. (1995), The Dynamics of Rock Glaciers: Data from Tröllskagi, North Iceland, *Steepland Geomorphology* pp. 129–145.
- Whalley, W. B. and Azizi, F. (1994), Rheological models of active rock glaciers: Evaluation, critique and a possible test, *Permafrost and Periglacial Processes* 5, 37–51.
- Woodward, J. and Burke, M. J. (2007), Applications of Ground-penetrating Radar to Glacial and Frozen Materials, *Journal of Environmental Engineering Geophysics* 12(1), 69–85.
- Xu, C., Chen, Y., Hamid, Y., Tashpolat, T., Chen, Y., Ge, H. and Li, W. (2009), Long-term change of seasonal snow cover and its effects on river runoff in the Tarim River basin, northwestern China, *Hydrological Processes* 23, 2045–2055.
- You, P. (1995), Surface water resources and runoff composition in the Tarim River basin, *Arid Land Geography* 18(2), 29–35.



## A Appendix



## A.1 Rock Glacier Inventory

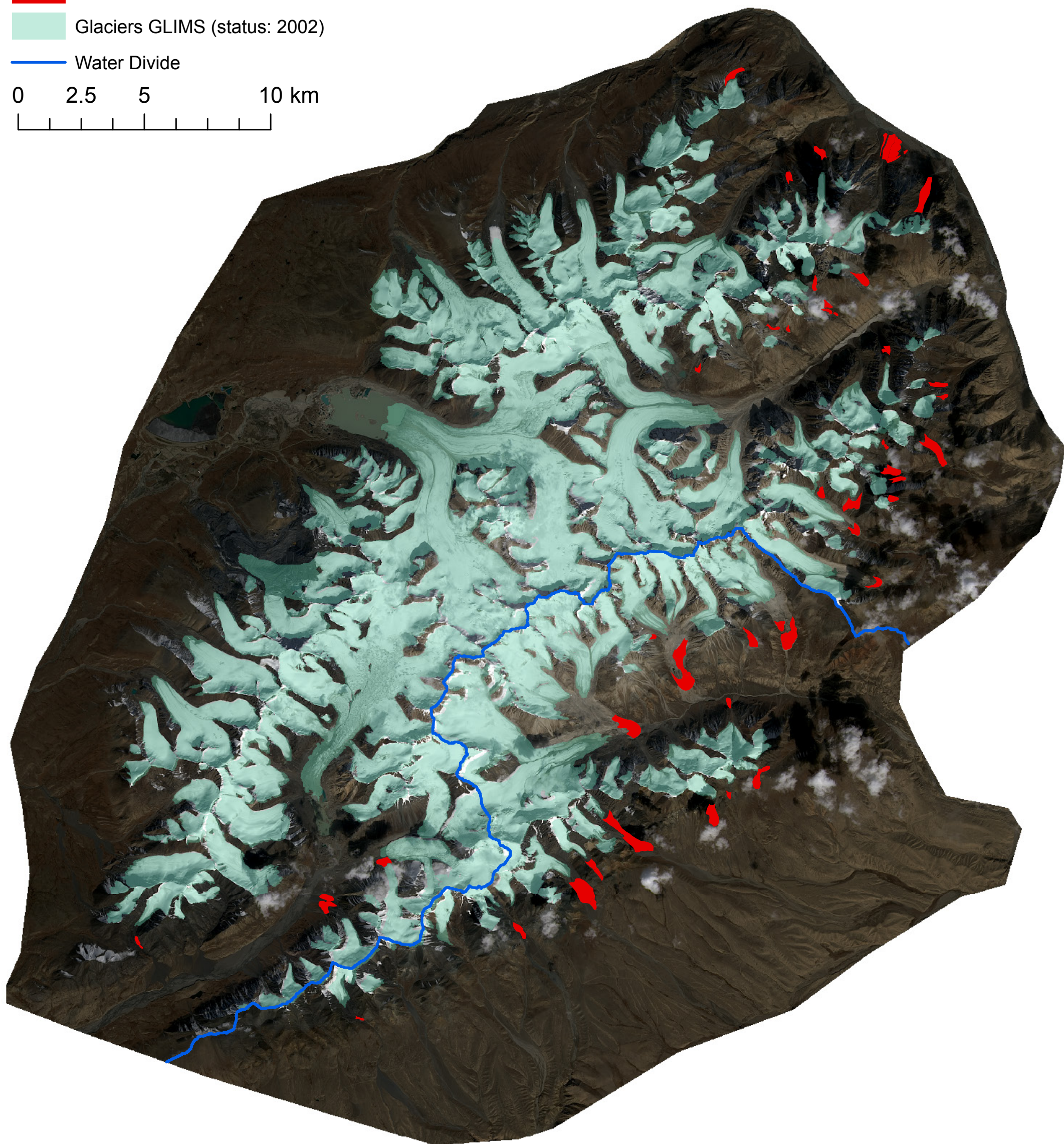


# Legend

-  Rock Glaciers
-  Glaciers GLIMS (status: 2002)

 Water Divide

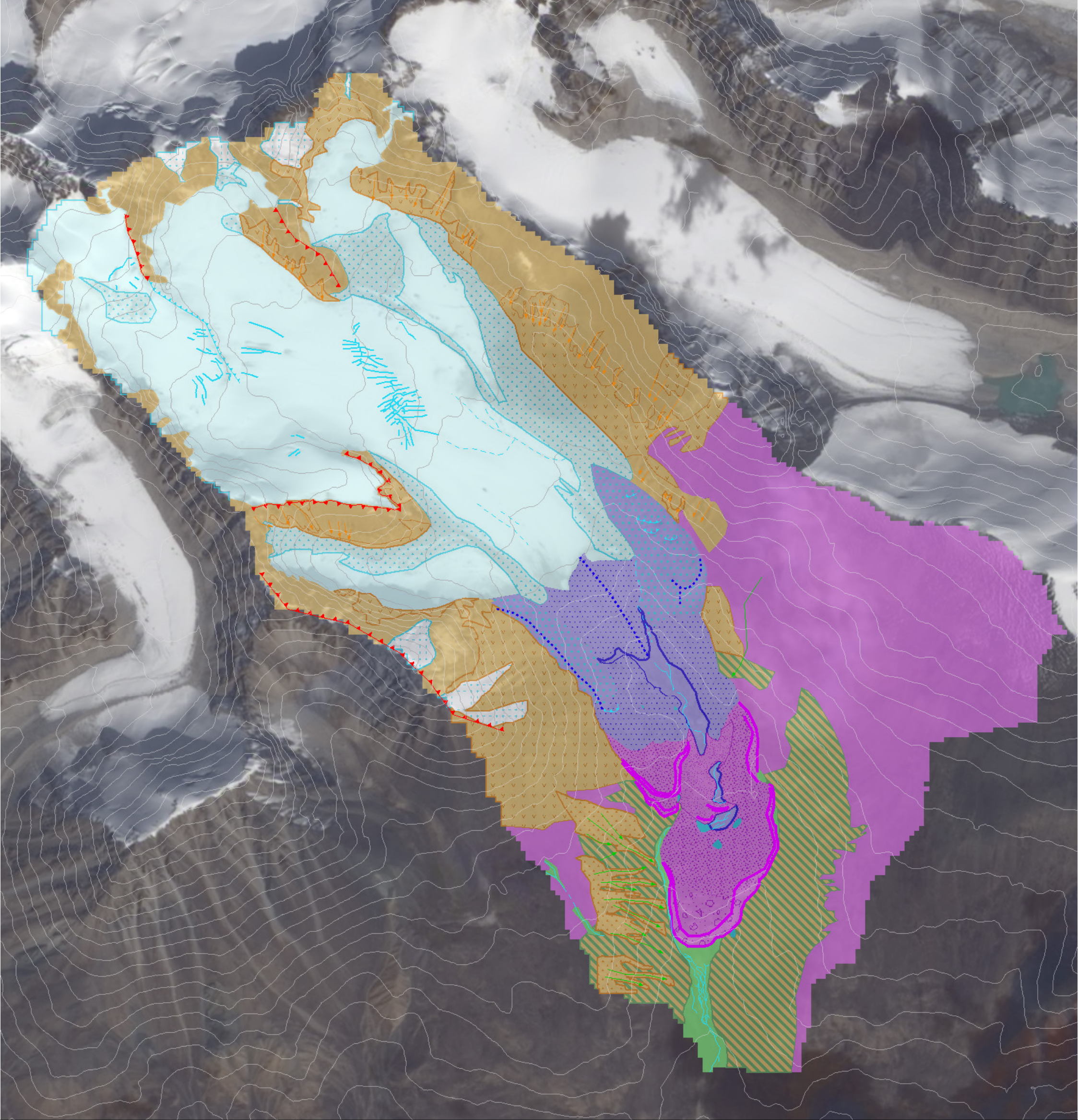
0 2.5 5 10 km





## A.2 Geomorphological Map





**glacial process domain**

- glacier
- supraglacial debris
- moraine accumulation
- ice-cored moraine
- permanent snow patch

- crevasse, serac
- ice fall
- morainic crest

**periglacial process domain**

- periglacial slope
- active rock glacier
- less active rock glacier
- periglacial deposits

- rock glacier front

**gravitational process domain**

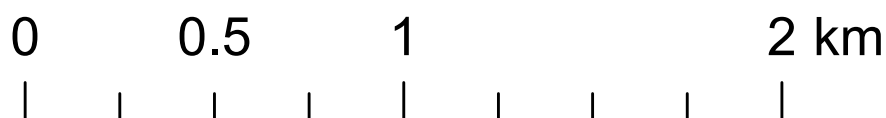
- gravitative accumulation area
- rockslide
- vegetation covered talus slope
- landslide

- rock scarp
- debris channel

**fluvial process domain**

- fluvial deposit area
- fluvio-glacial deposits
- lake

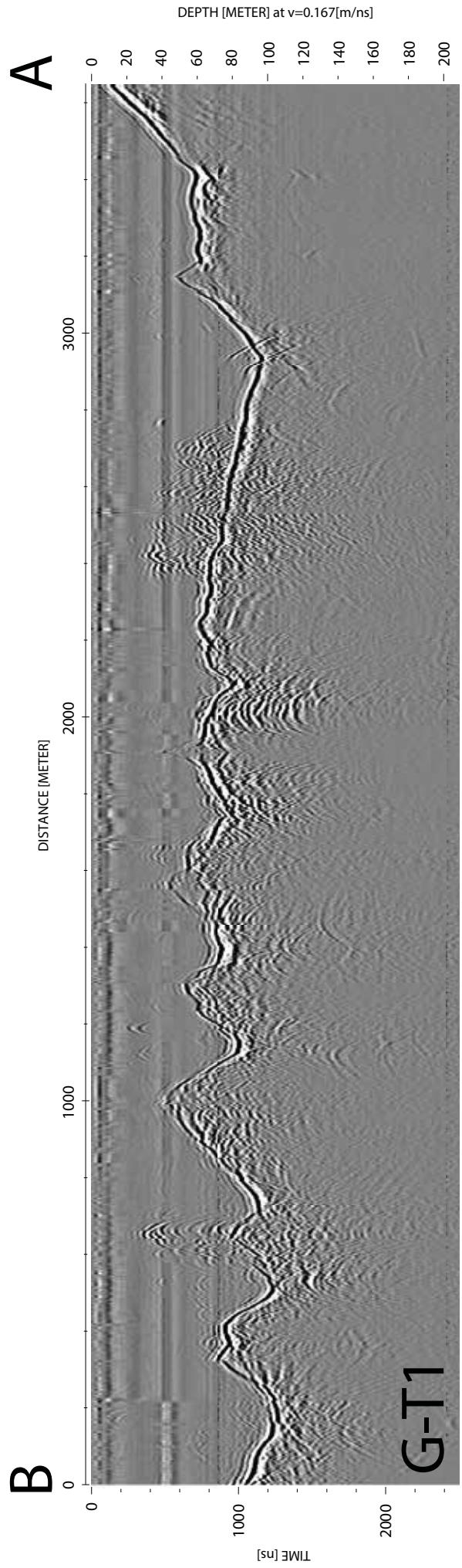
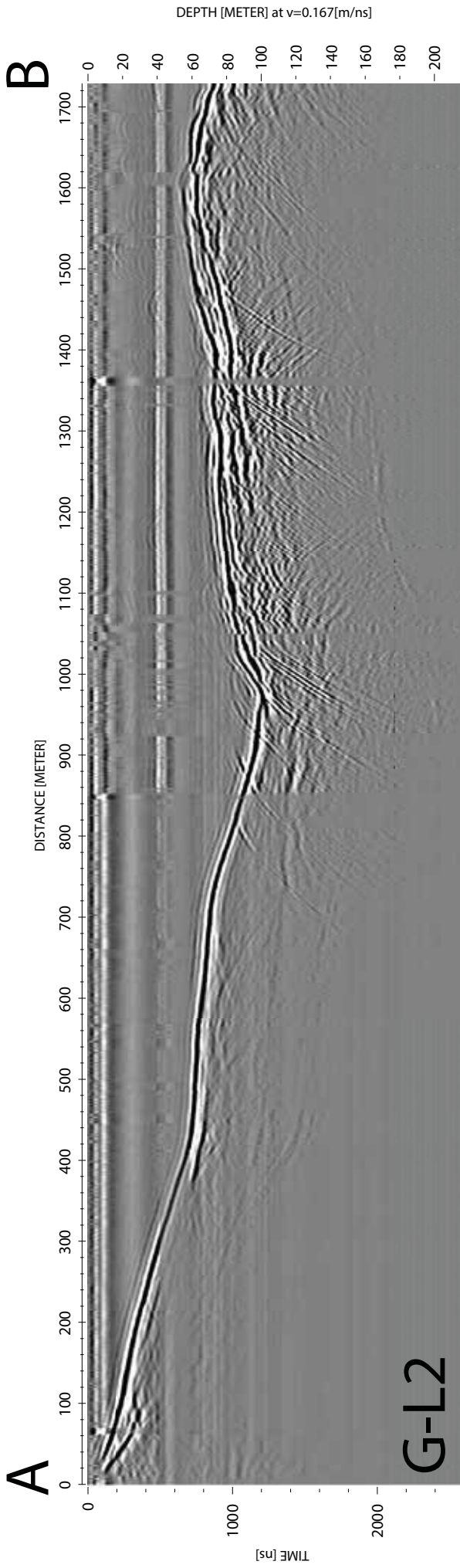
- stream
- intermittent stream
- debris flow channel

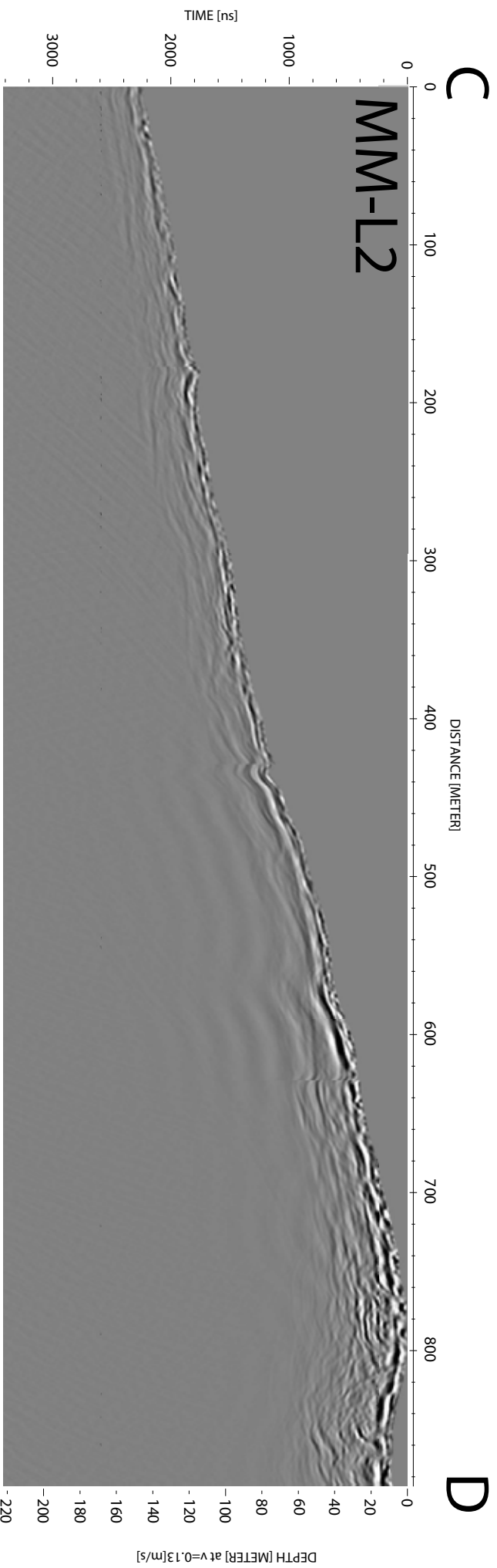
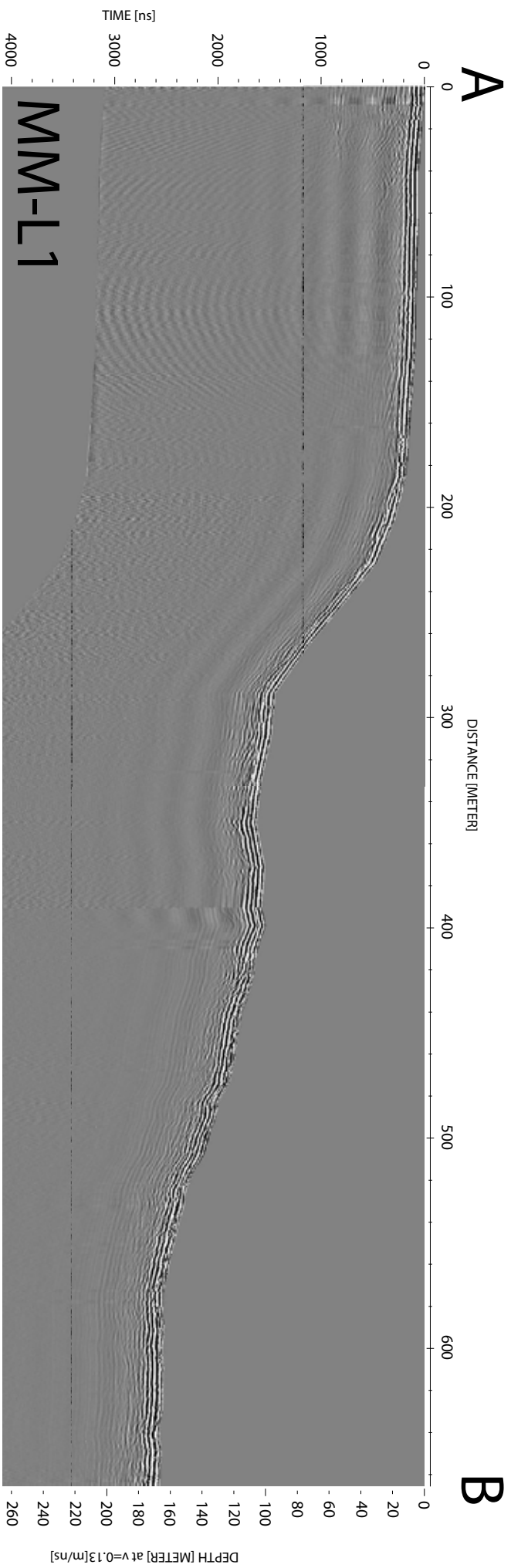




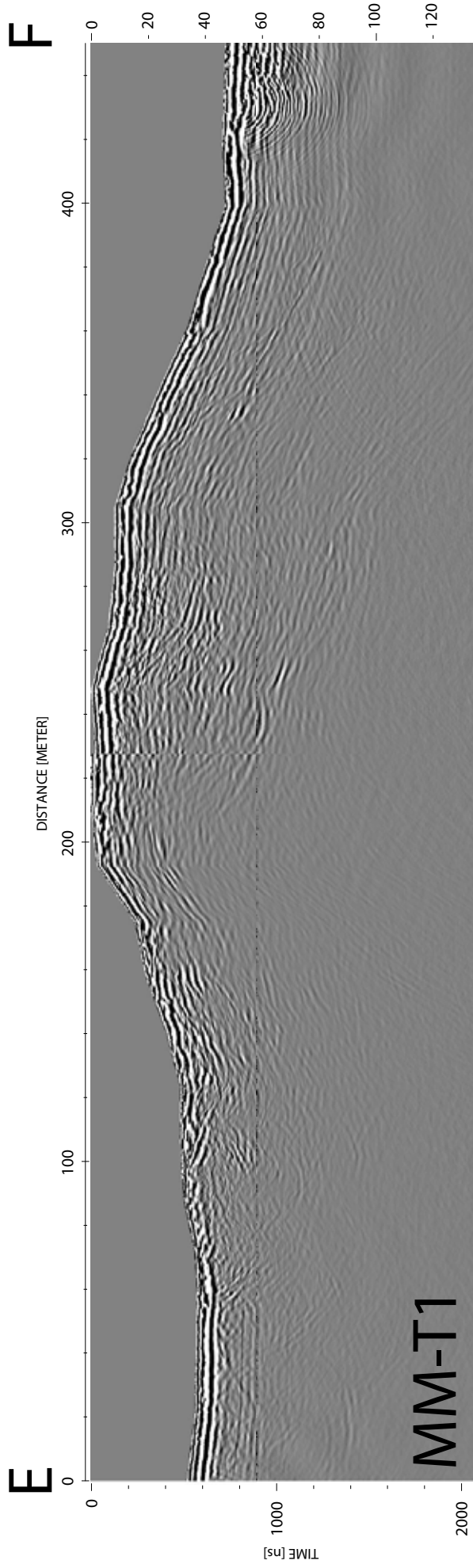
### A.3 GPR Profiles Used in Thesis

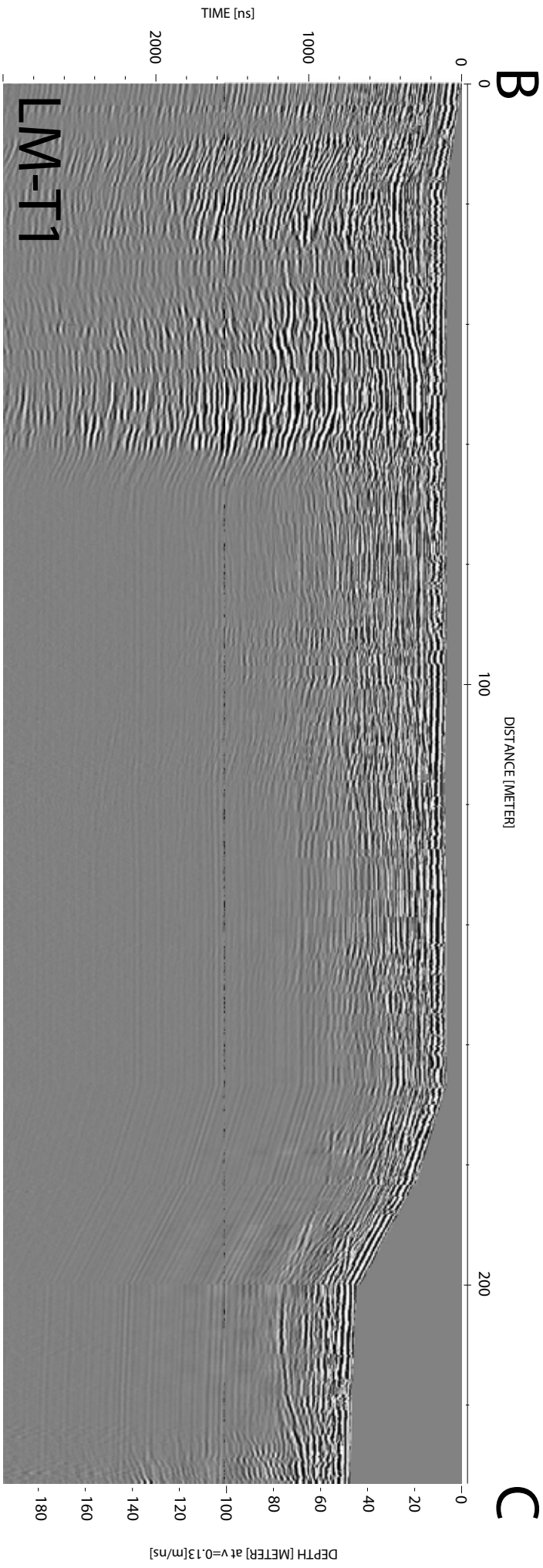
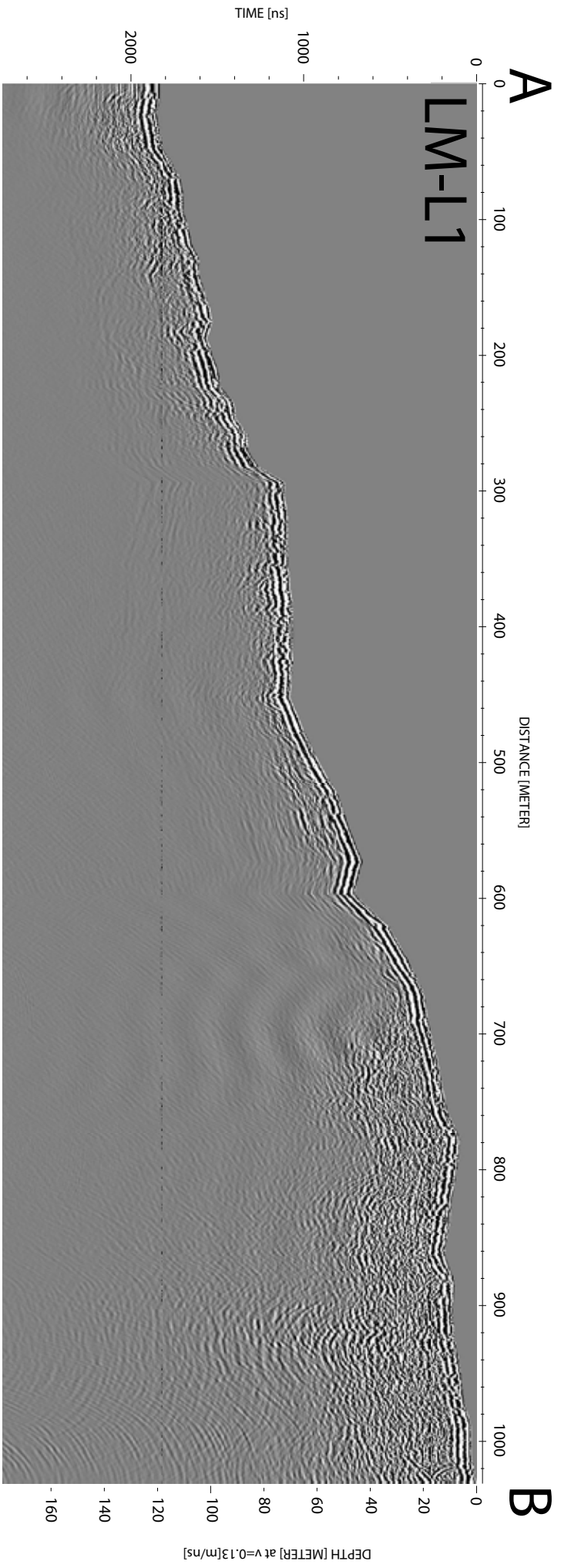


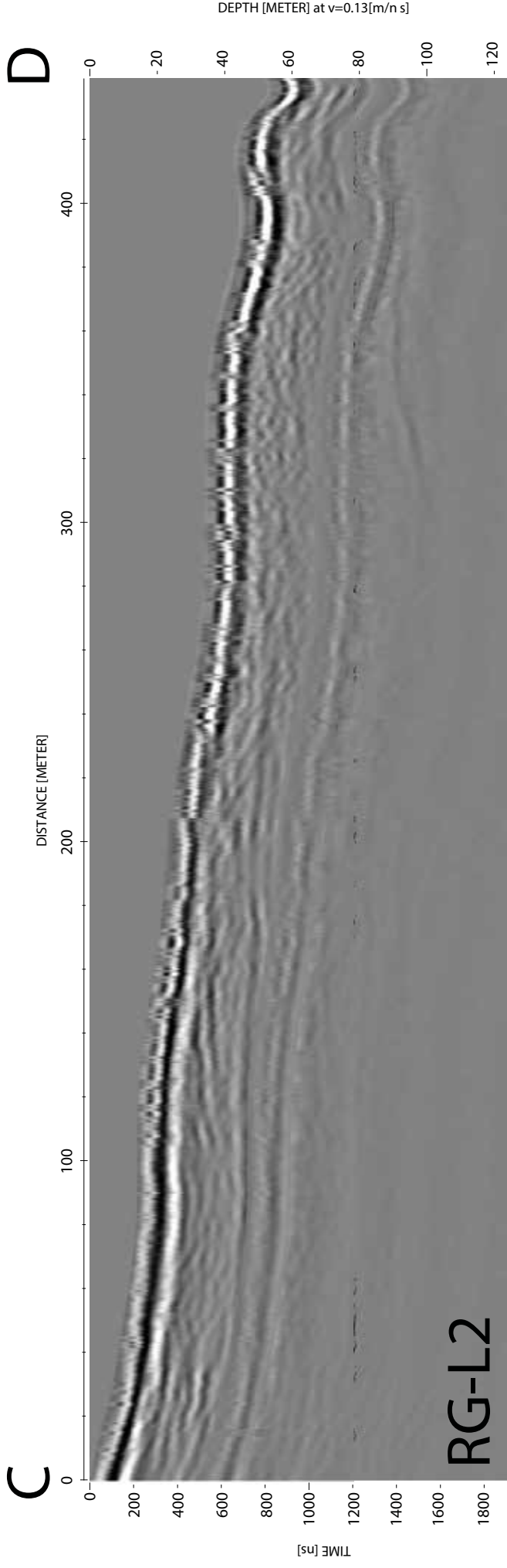
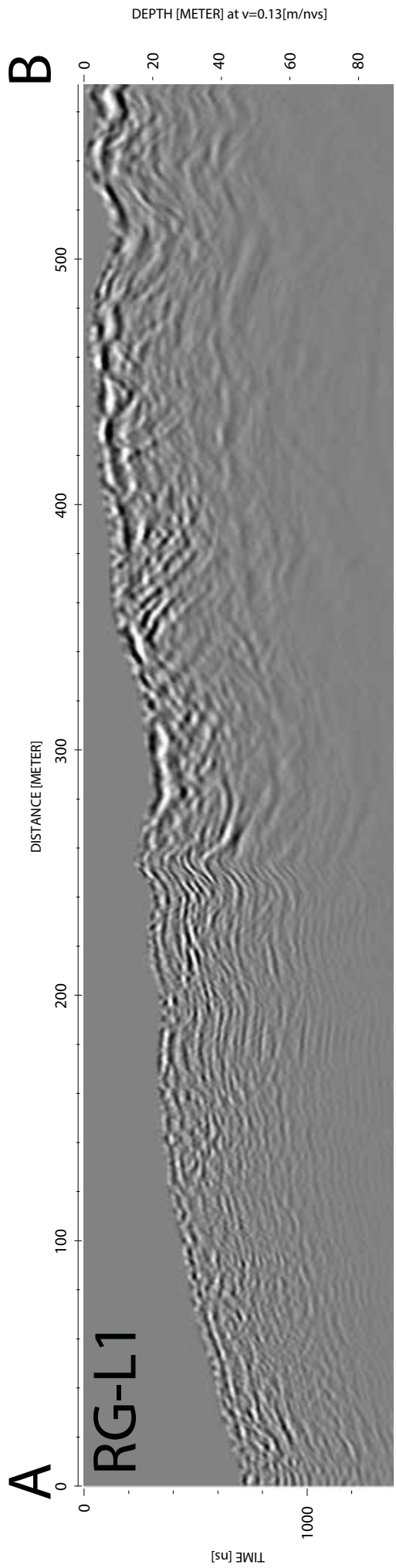


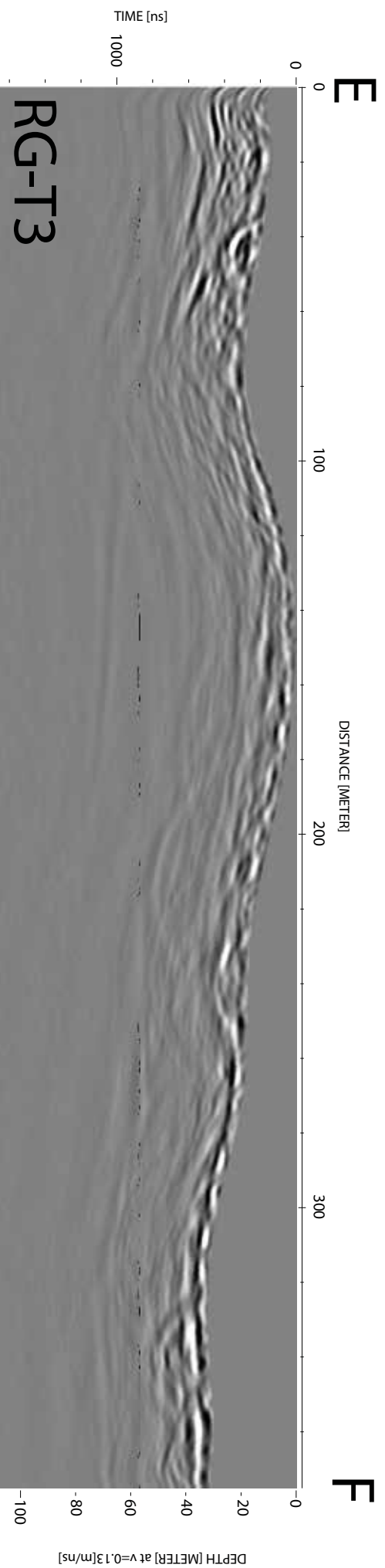
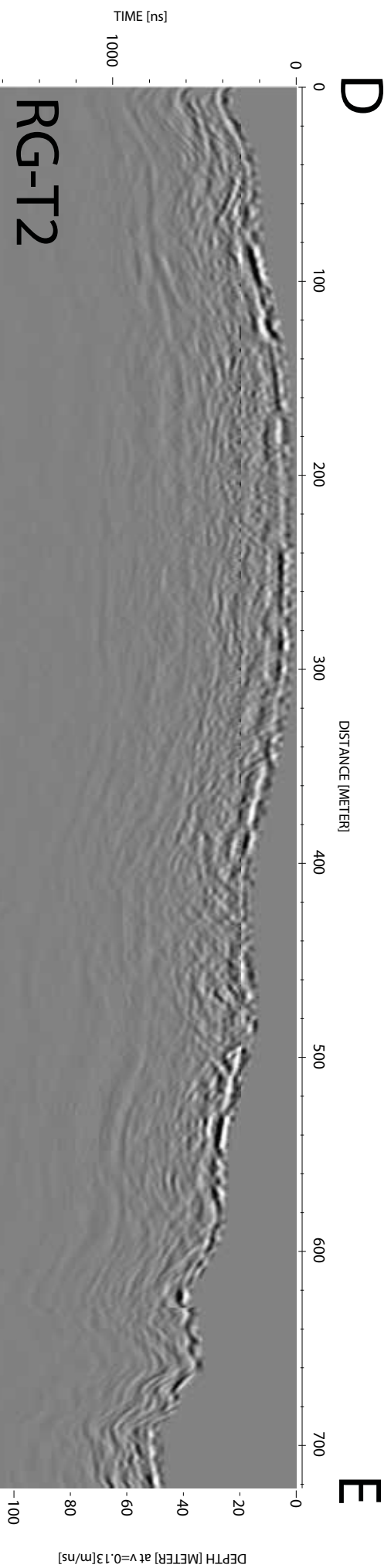
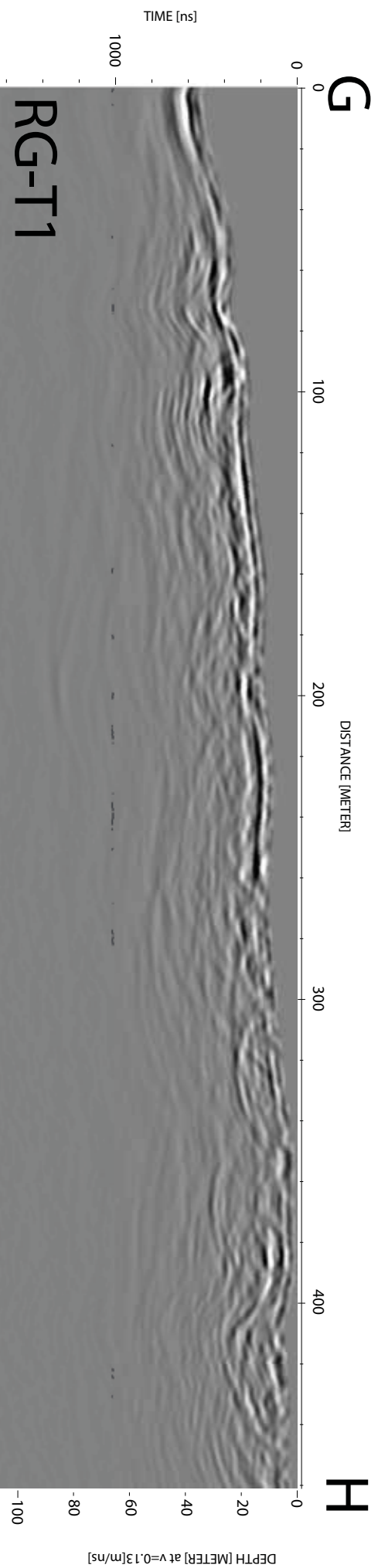


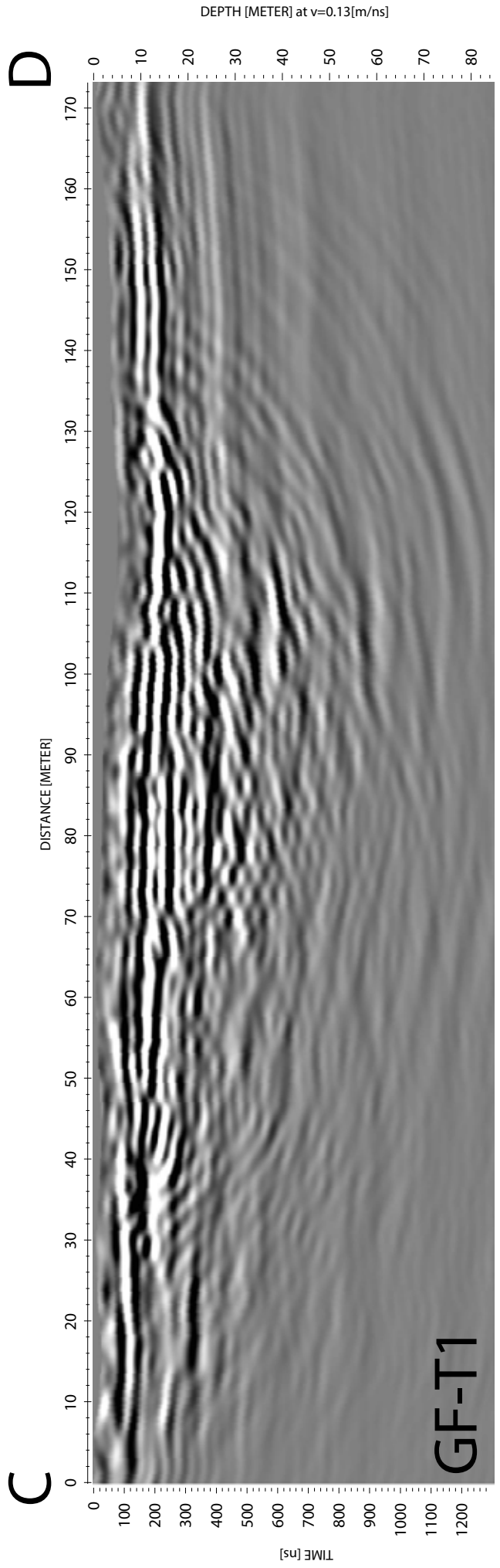
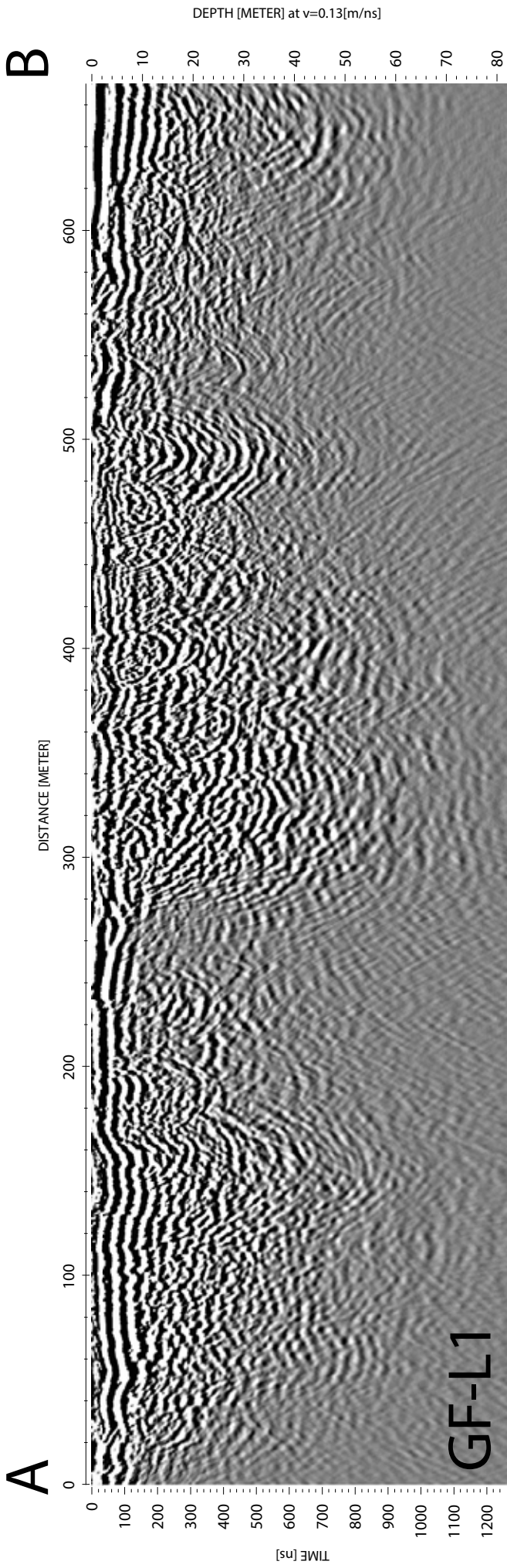
DEPTH [METER] at v=0.13[m/ns]





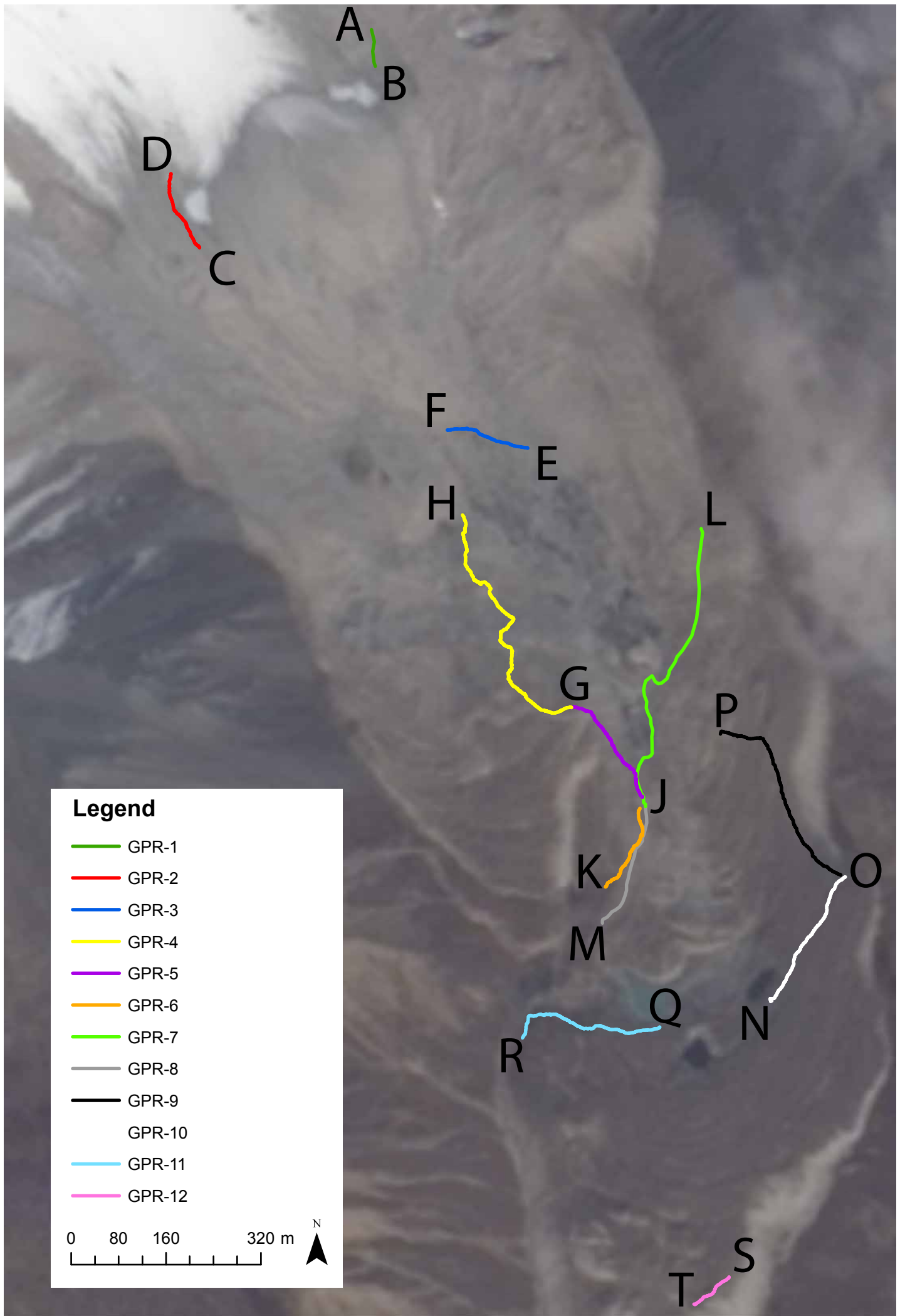


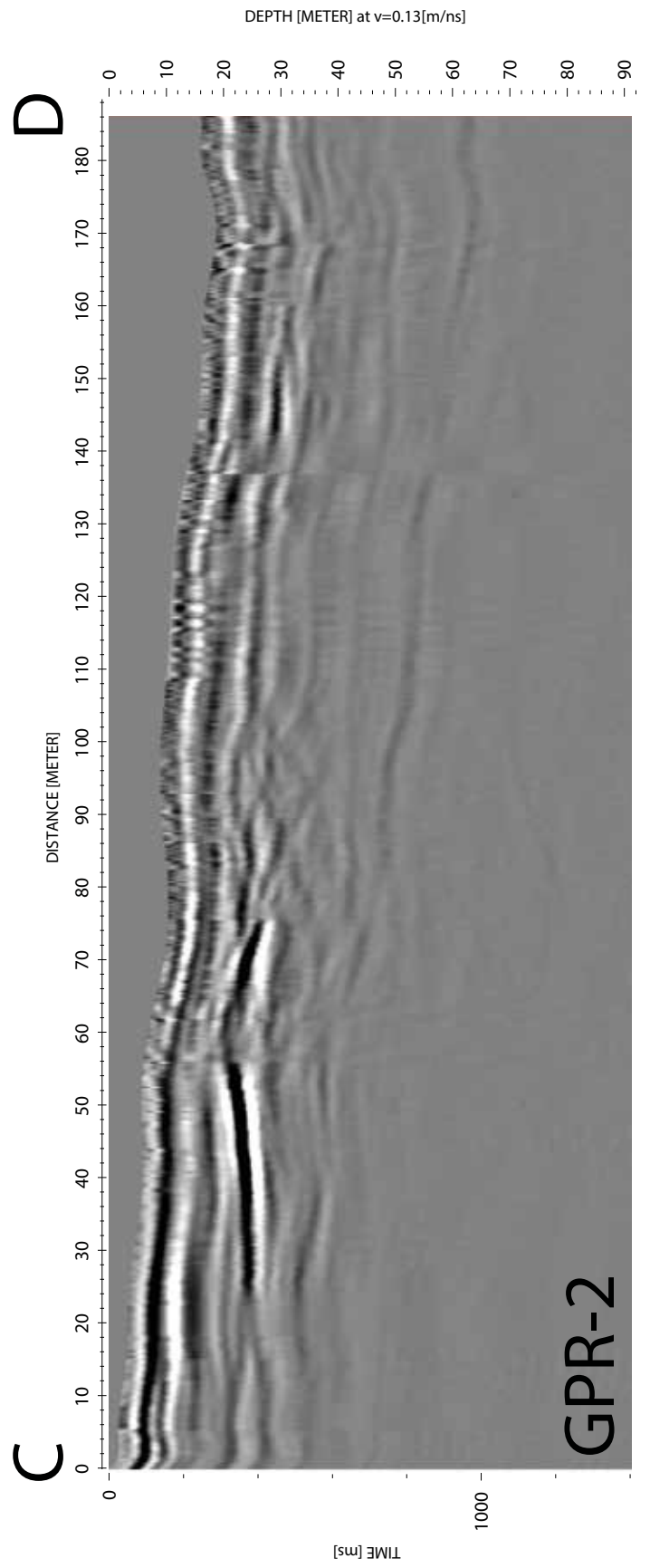
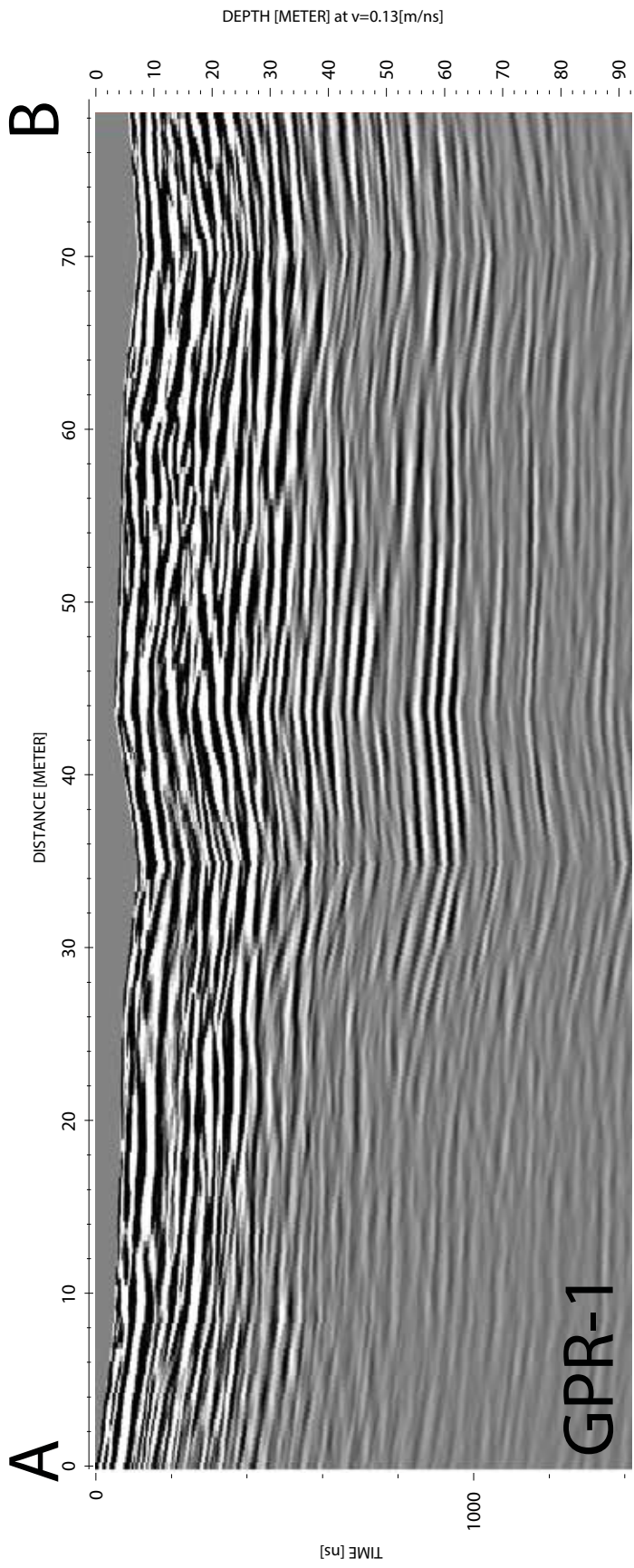


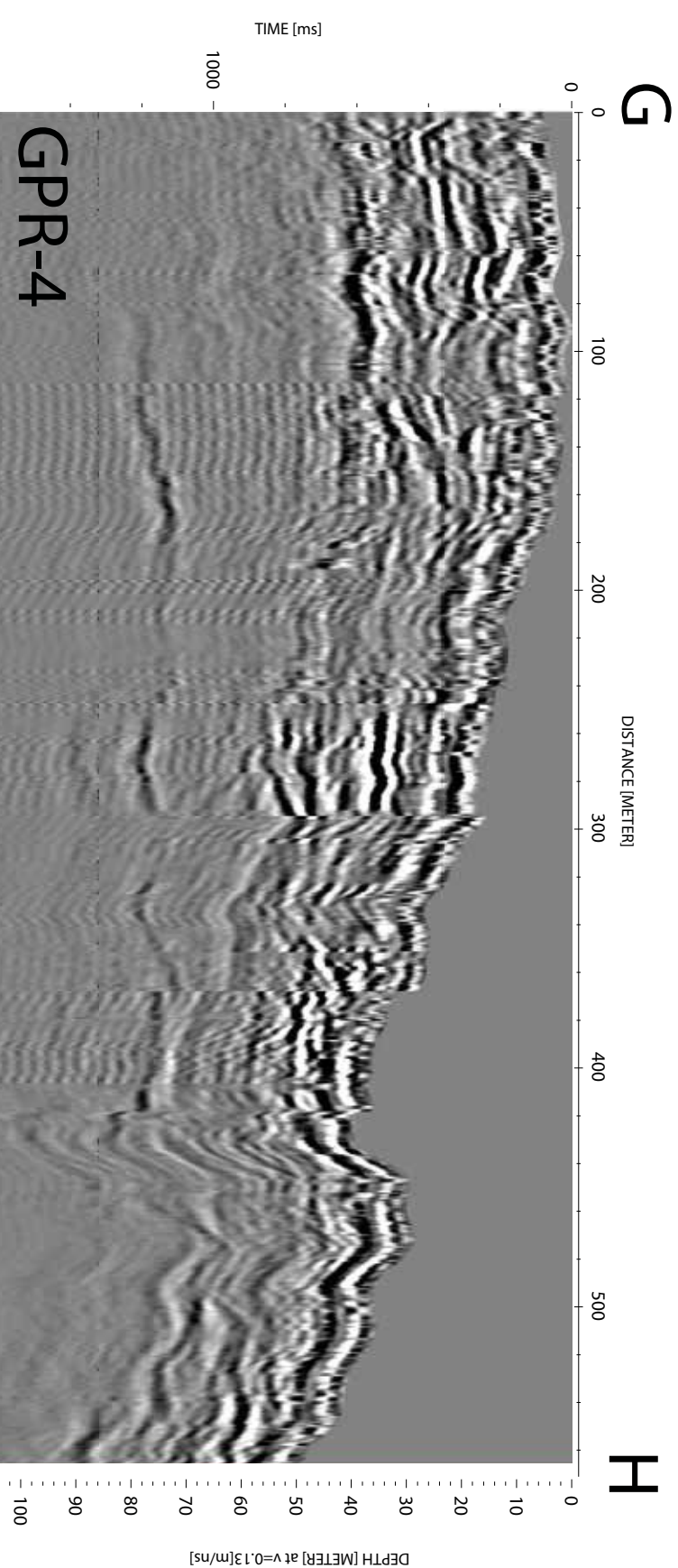
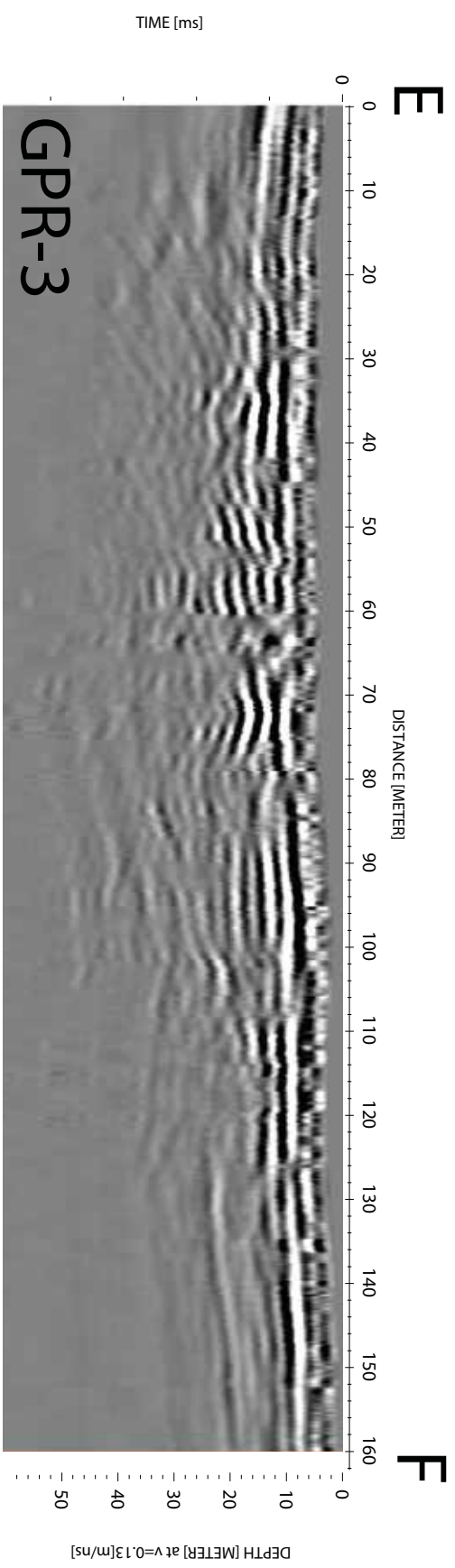


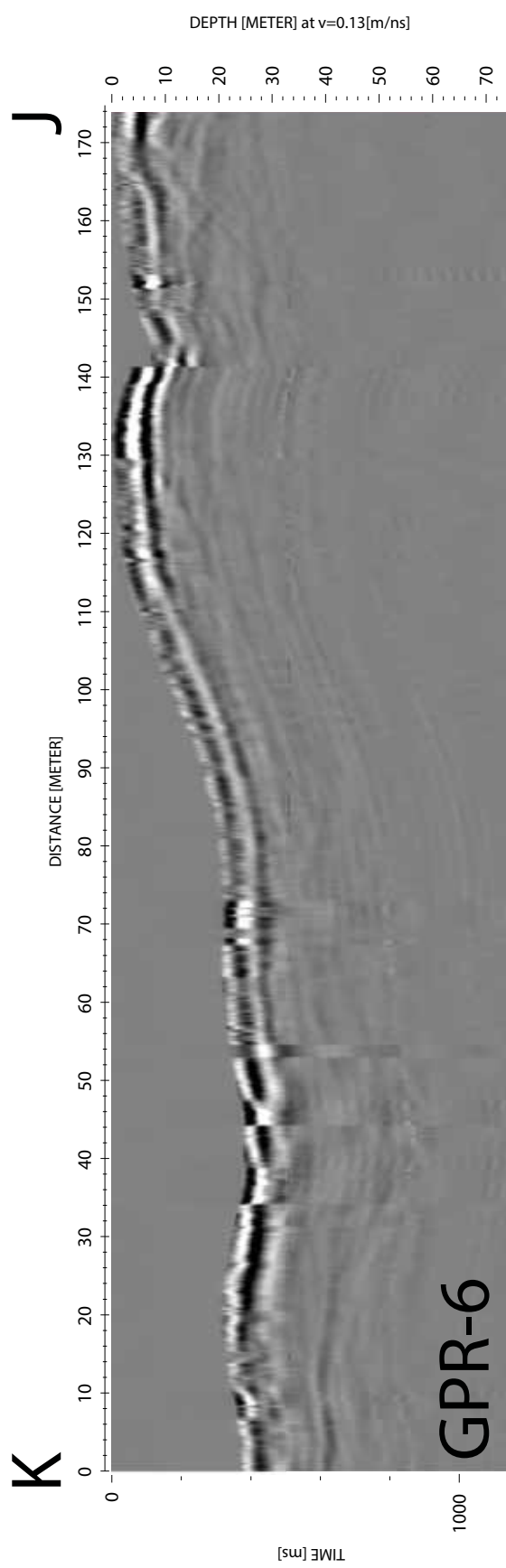
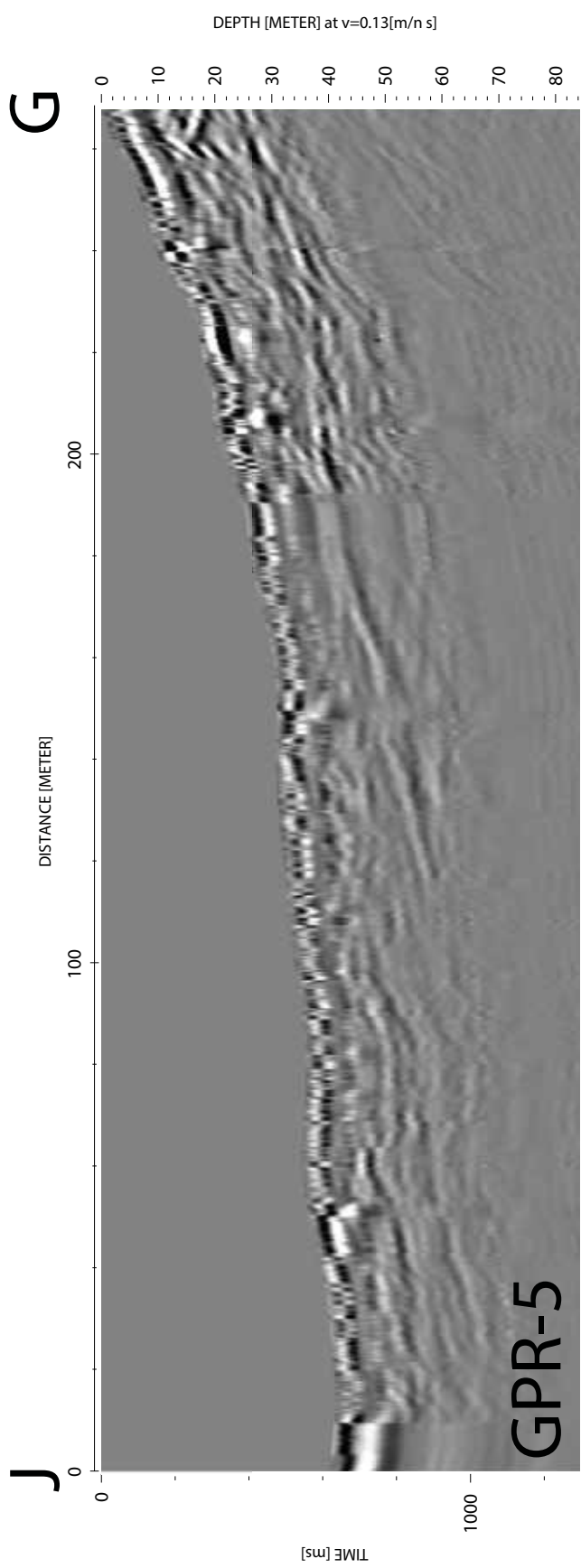


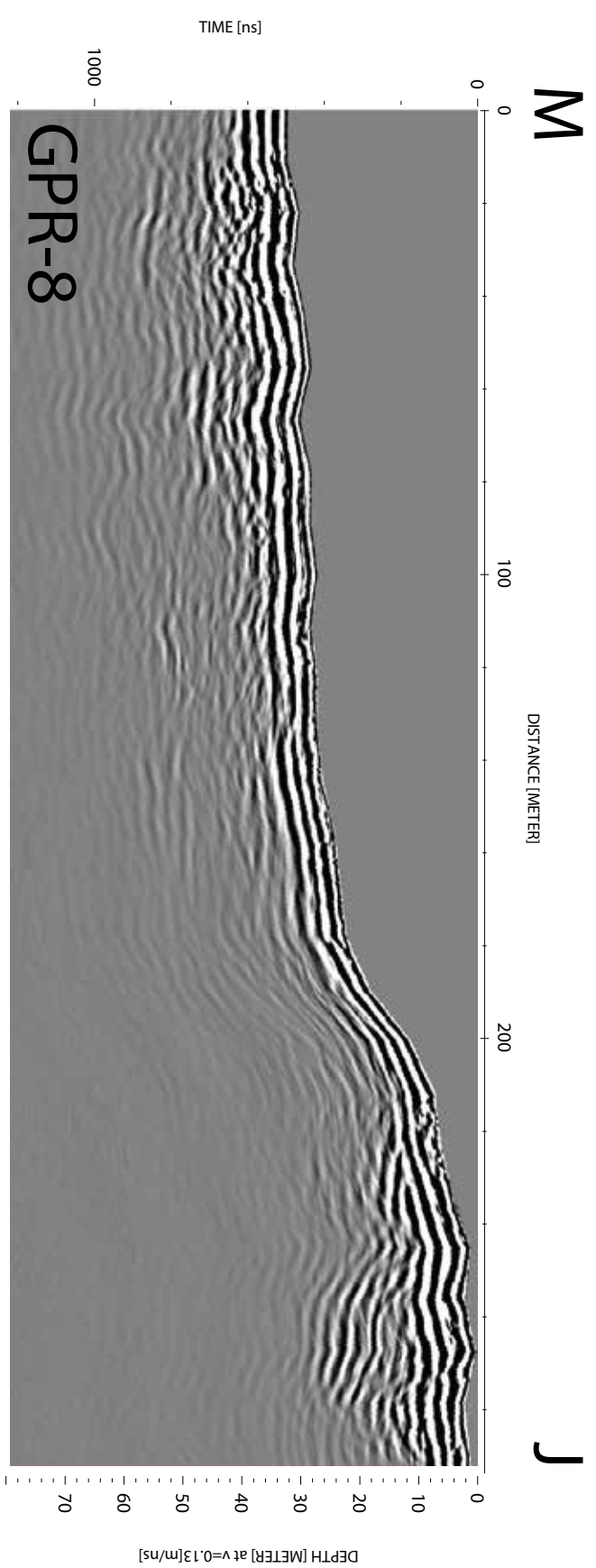
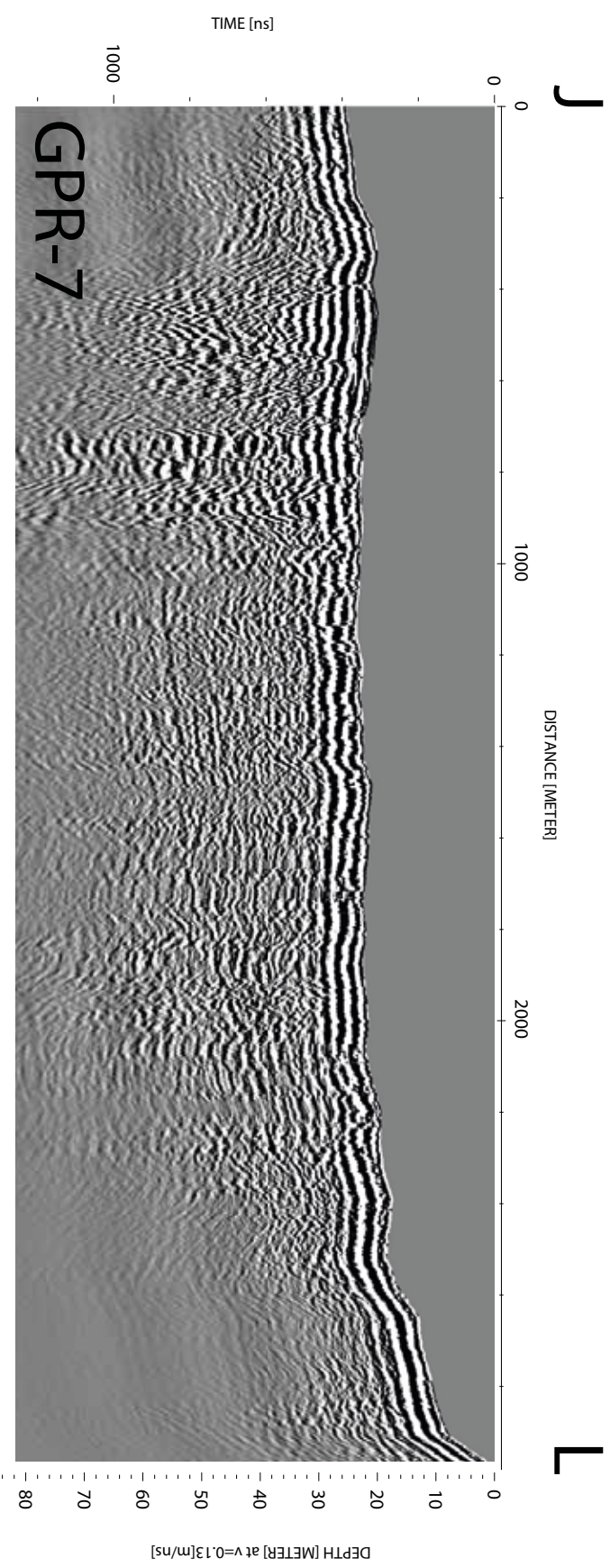
#### A.4 GPR Profiles Not Used in Thesis

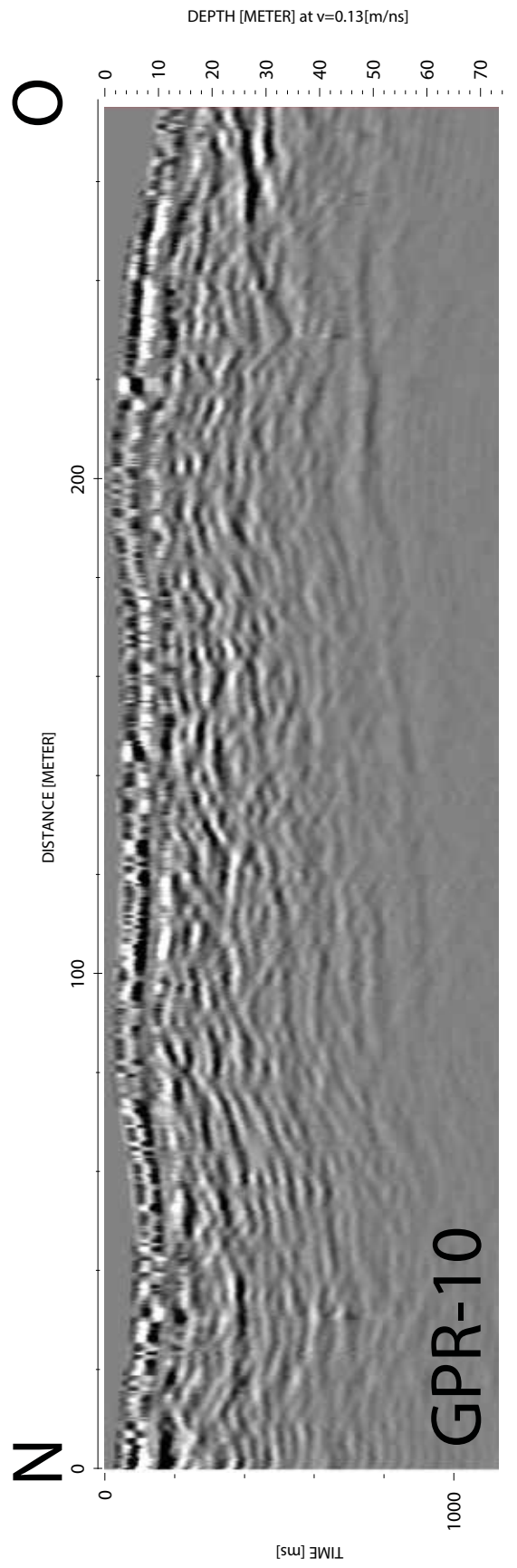
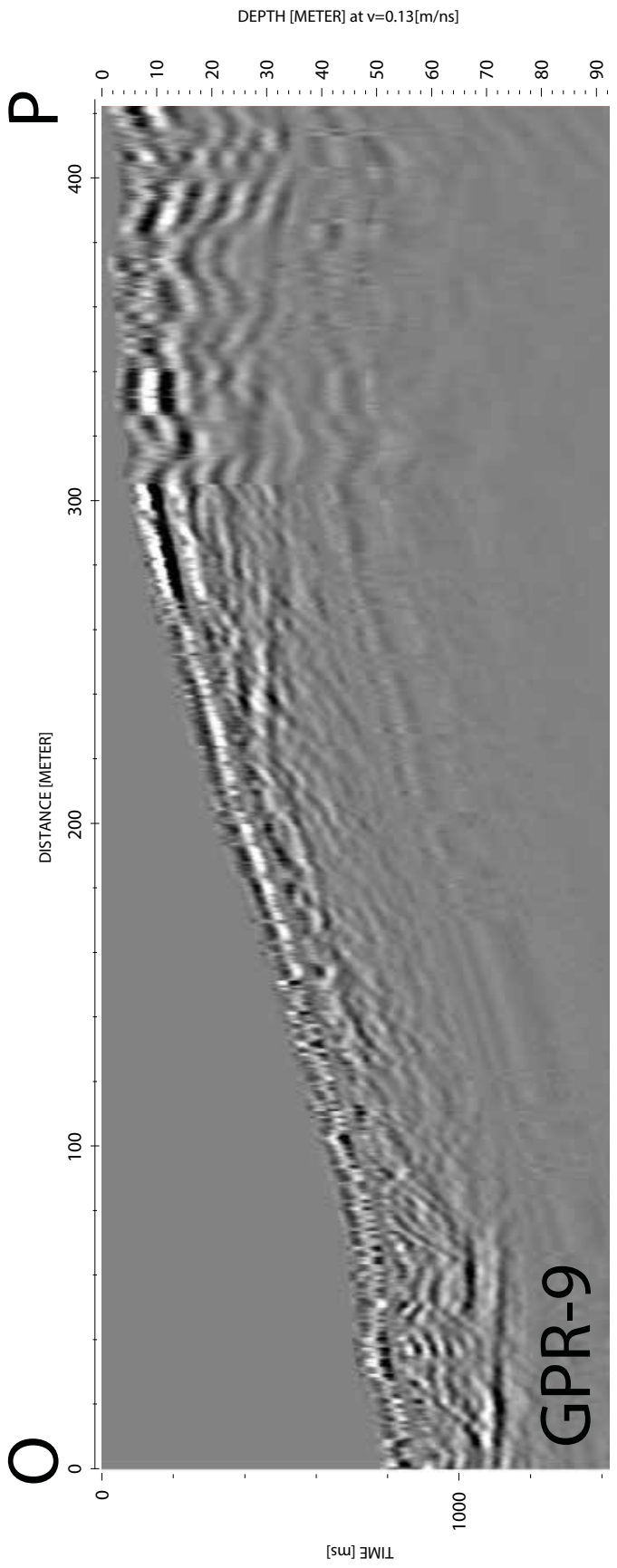


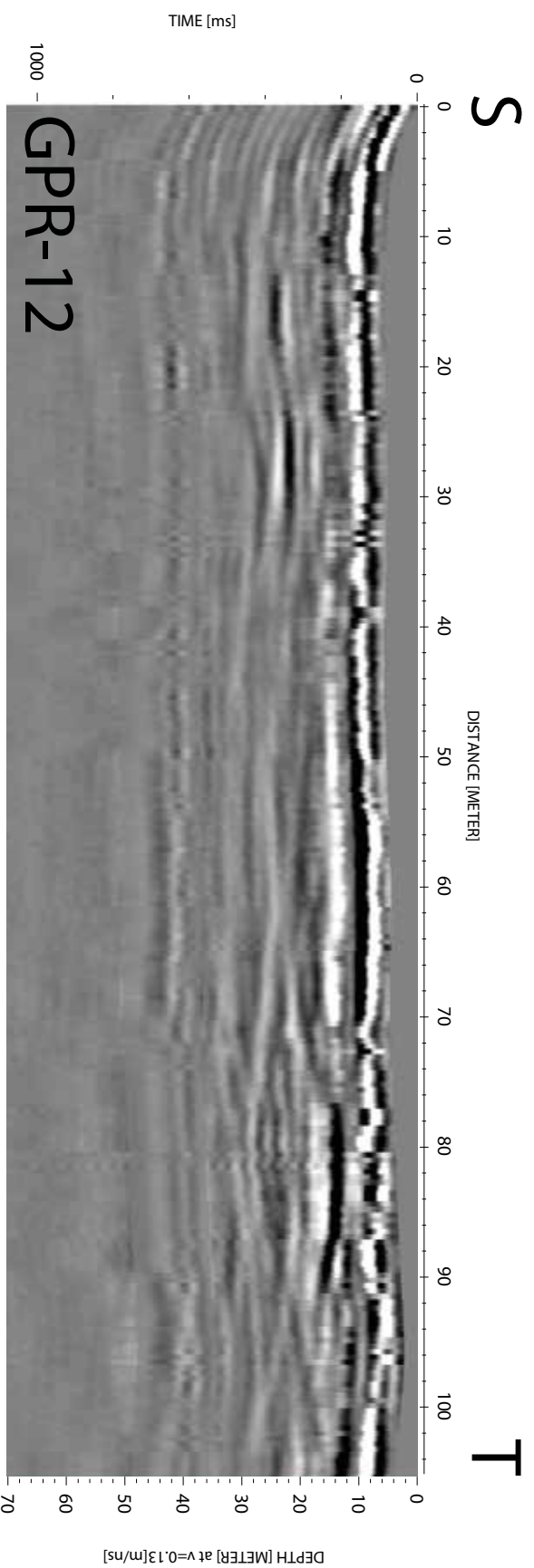
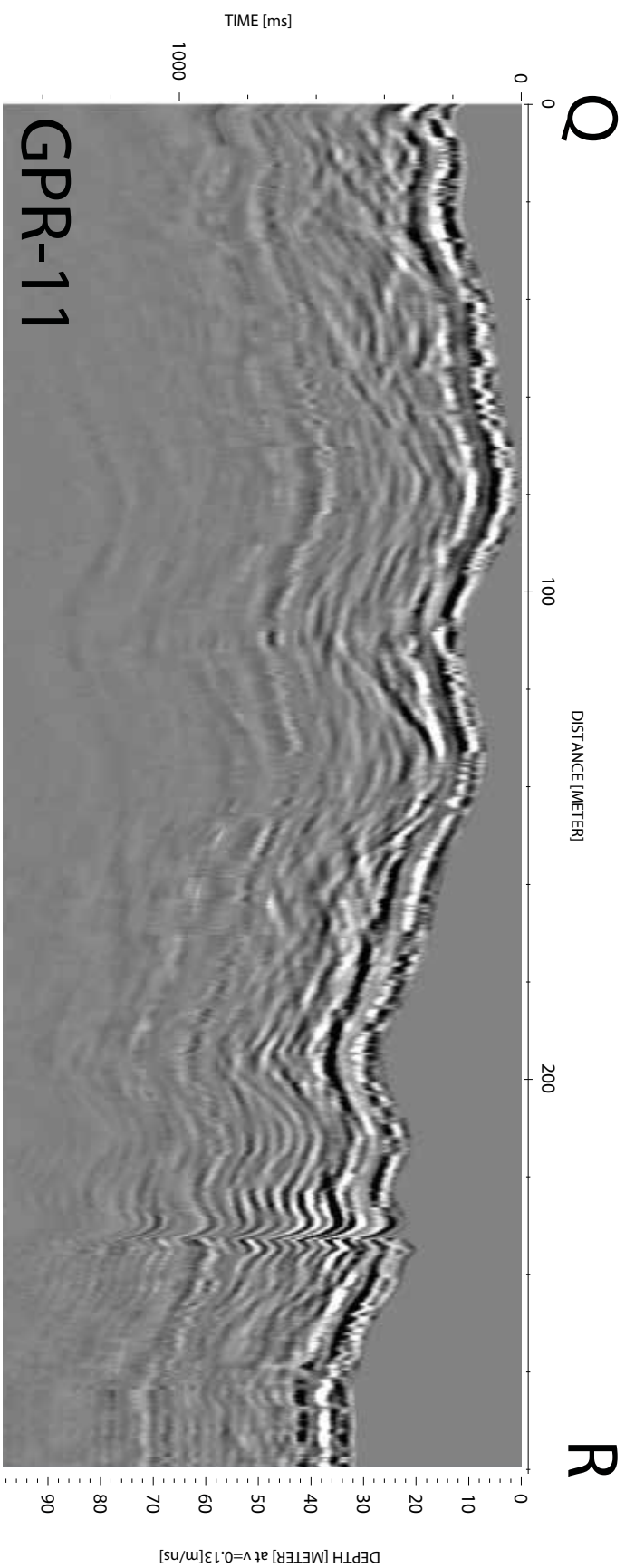












## **B Personal Declaration**

I hereby declare that the submitted thesis is the result of my own, independent, work. All external sources are explicitly acknowledged in this thesis.

Zürich, June 18, 2015

Nico Rohrbach